**Ice island deterioration in the Canadian Arctic:
Rates, patterns and model evaluation**

by

Anna J Crawford

A thesis submitted to the Faculty of Graduate and Postdoctoral
Affairs in partial fulfillment of the requirements for the degree of

Master of Science

in

Geography

Carleton University
Ottawa, Ontario

Abstract

Knowledge regarding the deterioration processes of large tabular icebergs, known as ice islands, is limited within the Canadian Arctic. This study analyzed ice island deterioration through two aspects: 1) horizontal (areal) and 2) vertical (surface melt or 'ablation'). Satellite images were digitized to monitor areal dimensions, classify deterioration modes and correlate deterioration rates with environmental variables. The rates of deterioration were different between the Eastern and Western Canadian Arctic regions possibly due to differences in air temperature and sea ice concentration. Validation of operational surface ablation models was also carried out with *in-situ* microclimate measurements. The Canadian Ice Service iceberg model under-predicted surface ablation by 68%, while a more complete energy-balance model developed for ice islands improved output accuracy (7.5% under-prediction). These analyses will provide useful knowledge regarding the deterioration process of ice islands to offshore stakeholders for mitigation of risks associated with ice island hazards to offshore operations.

Acknowledgements

Table of Contents

List of Figures

List of Tables

List of Appendixes

List of Symbols and Abbreviations

Symbol	Unit	Notes
Greek		
α	unitless	Albedo
Γ	J kg^{-1}	Latent heat of melting ice
ε_a	unitless	Atmospheric emissivity
ε_s	unitless	Emissivity of ice
ρ_a	kg m^{-3}	Air mass density
ρ_i	kg m^{-3}	Ice density
σ	W m^{-2} K^{-4}	Stefen-Boltzman constant
σ_{area}	km^2	Surface area error
σ_D	m	Uncertainty in D (image resolution dependent)
υ	m ns^{-1}	Electromagnetic wave velocity
Roman		
a	0.143	Exponential power-law parameter for wind speed calculation
C_E	unitless	Latent heat turbulent exchange coefficient
c_{pa}	J kg^{-1} K^{-1}	Dry air specific heat
C_S	unitless	Sensible heat turbulent exchange coefficient
D	km	Side length of a square equal in surface area to an ice island
e_a	Pa	Atmospheric vapour pressure
e_s	Pa	Vapour pressure at the ice surface
I	W m^{-2}	Insolation, absorbed shortwave radiation
$K\uparrow$	W m^{-2}	Reflected incoming shortwave radiation
$K\downarrow$	W m^{-2}	Incoming shortwave radiation
$L\uparrow$	W m^{-2}	Outgoing (emitted) longwave radiation
$L\downarrow$	W m^{-2}	Incoming longwave radiation
L_v	J kg^{-1}	Latent heat of vaporization
M	mm	Amount of surface ablation (surface lowering)
p	hPa	Atmospheric pressure
Q_E	W m^{-2}	Latent energy flux density
Q_G	W m^{-2}	Ground energy flux density
Q_M	W m^{-2}	Melt energy density
Q_N	W m^{-2}	Net radiation flux density
Q_R	W m^{-2}	Rain energy flux density
Q_S	W m^{-2}	Sensible energy flux density
R	m d^{-1}	Rate of surface ablation (rate of surface lowering)
RH	%	Relative humidity
s	m	Antenna separation
T	m	Total ice thickness
t	ns	Two-way travel time
T_a	K	Air temperature
T_s	K	Ice temperature
Δt	Hour	timestep

U_s	m s^{-1}	Wind speed
ΔU_s	m s^{-1}	Wind speed differential (10 m and surface)
U_1	m s^{-1}	Wind speed (10 m)
U_2	m s^{-1}	Wind speed (surface)
v	m ns^{-1}	Electromagnetric wave velocity
z	m	Height

Abbreviations

BAA		Bulk aerodynamic approach
BBC		British Broadcasting Corporation
BREA		Beaufort Regional Environmental Assessment
CIS		Canadian Ice Service
DDF	mm d^{-1} °C d^{-1}	Degree day factor
DAZ		Days above 0°C
EB		Energy balance
GEM		Global Environmental Multiscale model
GIS		Geographic information system
GRIP		Government Related Initiatives Program
IIP		International Ice Patrol
MDD		Melting degree day (daily average temperatures > 0°C)
NAIS		North American Ice Service
NCAR		National Center for Atmospheric Research
NCEP		National Centers for Environmental Prediction
NSERC		National Science and Engineering Research Council
NSTP		Northern Scientific Training Program
PDD		Positive degree day (sum of temperatures > 0°C for time interval)
RMSE		Root mean squared error
SST	°C	Sea surface temperature
TIM		Temperature index model

1.0 Introduction

The Arctic has experienced effects of climate change over the past 40 years (Derksen et al., 2012), with air temperature rising almost two times more rapidly than the global average (Trenberth et al., 2007). The trend is not expected to abate, with a 3-5°C projected increase in Arctic air annual mean temperatures by 2100 (IPCC, 2001; Johannessen et al., 2011). Observations of rapid change in the cryospheric components (frozen environments) of the Arctic are associated with the warming. This has wide-ranging physical implications, which include diminishing sea ice extents and reduced surface reflectivity (albedo). Resulting feedback loops exacerbate warming and contribute to Arctic amplification of climate change (Derksen et al., 2012).

Ice shelves and floating glacial tongues are components of the Arctic cryosphere affected by climate change which have been negatively impacted by increasing atmospheric and oceanic temperatures (Copland et al., 2007; IPCC, 2007; Peterson, 2011). The weakening and break-up of these ice features leads to the calving of ice islands (large, tabular icebergs). The Ellesmere ice shelves saw a marked decrease in areal extent over the 20th and start of the 21st centuries (Derksen et al., 2011). High Arctic temperatures recorded in the 1930s and 1940s likely resulted in ice island calving events from these ice shelves, while the increasing trend in Arctic temperatures since the 1990s has resulted in the continuation of these events (Derksen et al, 2011; Copland et al., 2007). The areal extent of the Ellesmere Island ice shelves decreased from 8900 km^2 in 1906 (Vincent et al., 2011) to 1043 km^2 in 2002 (Mueller et al., 2006) and 500 km^2 in 2012 (Mueller et al., 2013). Major ice island calving events have been recorded at least once a decade between 1940 and 1990 (Jeffries and Sackinger, 1988). Eight such events have occurred to these ice shelves since 2000 (Vincent et al., 2011). The remaining 500 km^2 of ice shelves is

susceptible to future calving as it has lost its protective barrier of multi-year sea ice (Mueller et al., 2013; Vincent et al., 2011; Mueller et al., 2008).

Greenland's increased iceberg production since 1995 is also attributed to climate change (Timco, 2007). The floating glacial tongue of the Petermann Glacier (northwest Greenland), a contributor of ice islands to the waters off Canada's east coast, was within its historical limits until the early 2000s (Peterson, 2005; Johannessen et al., 2011). Yet, after calving events in 2003, 2008 and 2010, the terminus was repositioned 15 km further inland than ever observed (Peterson, 2011; Johannessen et al., 2011). The increase in calving frequency may be associated with warming ocean temperatures, increased melt channeling and the absence of sea ice (Rignot and Steffen, 2008).

Warming conditions which reduce sea ice extents can allow for an increase in offshore activity (Valsson and Ulfarsson, 2011). However, ice islands and icebergs, which are also connected with climate change, are known to pose a hazard to vessels and offshore infrastructure (Comiso, 2012; McGonigal et al., 2011; Prowse et al., 2009; Peterson, 2011). This needs to be taken into account when assessing operational risks in the region (e.g., shipping through the Northwest Passage or offshore oil exploration and extraction) as a collision with an ice island or calved fragment could have detrimental economic and environmental outcomes (Veitch et al., 2001) in the remote and ecologically sensitive Arctic marine environment.

Agencies such as the North American Ice Service (NAIS), International Ice Patrol (IIP) and Canadian Ice Service (CIS) have developed operational drift and deterioration models for typical (i.e., non-tabular) icebergs (Murphy and Carriers, 2011; Kubat et al., 2005; Kubat et al., 2007). A limiting factor for these operational models is the lack of observational data for model validation (Murphy and Carrieres, 2011; Ballicater, 2012). The CIS deterioration model was in general agreement with calving observations (Kubat et al., 2007) while the drift model forecasted

well for only the first 48 hours (Kubat et al., 2005) in validation trials during model development. Ice islands warrant further study due to their distinct morphology and far greater extents than typical icebergs that are already characterized and modeled. Future research needs to include an improved understanding of ice island occurrence, trajectories, morphology and detection in the Canadian Arctic, as well as the processes that affect their drift and deterioration. This body of research would aid in the calibration and validation of operational ice island drift and deterioration models for agencies such as the CIS. These tools can be used for ice island risk assessment and management planning, allowing offshore industry to target activity to low-risk locations with both economic and environmental benefits (Khan and Amyotte, 2002).

1.1 Research objectives and study hypothesis

This thesis contributes to the knowledge gaps identified above by characterizing and analyzing a number of the processes contributing to ice island deterioration, estimating numbers of individual ice hazards in Canadian Arctic waters, and evaluating surface ablation (melt) models. This ice island deterioration analysis is part of a larger collaborative research initiative on ice islands sponsored by the CIS, ArcticNet and the Water and Ice Research Laboratory at Carleton University. Ice island deterioration was assessed at two spatial scales in this thesis.

1) A comparative study of ice island deterioration between two Canadian Arctic regions assessed areal deterioration. This part of the study examined the hypothesis that the rates and observed modes of deterioration in the eastern and western Canadian Arctic are different based on an ice island's location of origin, resulting drift trajectory and environmental conditions to which it is exposed.

2) A site-specific study of an ice island's microclimate and associated surface ablation analyzed the vertical aspect of deterioration (thickness change). This part of the study

examined the hypothesis that modifying surface ablation models originally developed for 'typical' icebergs to represent a more comprehensive energy-budget will improve model representation of the magnitude of an ice island's surface melt. Throughout this thesis, surface ablation refers to the lowering of the above-water surface of an ice island through a combination of processes including, sublimation, melt, evaporation and runoff.

1.2 Methodological approach and paper contributions

This study, beginning with data collection through analysis and final presentation as manuscript-based chapters, was developed for operational applicability regarding ice hazard assessment and management. The hypotheses above were evaluated with the combination of field work, remote-sensing and modeling. A large benefit of the study is the on-site data collected from ice islands at northern locations which allowed for drift tracking and deterioration monitoring of multiple ice islands. Ice island data is historically limited due to the logistical difficulties of ice island field work. Re-visits are rare due to deterioration and drift between field excursions. For this reason, ice island bottom melt (basal ablation) was not recorded in this thesis. However, the impacts of four of the five processes included in deterioration modeling are documented in chapters 3 and 4 and provide a near-complete representation of ice island evolution.

Chapter 3, 'Deterioration modes of ice islands in the eastern and western Canadian Arctic regions', is a detailed work on how ice island deterioration rates and modes vary based on origin and drift location, and examines ice islands associated with recent calving events of 2008 and 2010. Real-time tracking of seven ice islands by deployed GPS beacons aided in high-resolution satellite-imagery acquisition. Nearly 100 RADARSAT-2 images were acquired through a collaborative agreement with the CIS (Environment Canada). Remote-sensing is a key

component of ice hazard identification and subsequent monitoring. Ice island deterioration was monitored and quantified in this study with image analysis in GIS software. This analysis classified the deterioration modes of ice islands into three modes and quantified the ice discharge from deteriorating ice islands.

The analysis presented in Chapter 4, 'Surface ablation model evaluation on a drifting ice island in the Canadian Arctic', utilizes the first *in-situ* microclimate data for a Canadian Arctic ice island to test and validate operational surface ablation models, as well as analyze its energy-balance and the environmental variables which control surface ablation. The use of this four-week dataset will be used to assess the second hypothesis listed above. Both studies are strengthened by the use of regional (Canadian Arctic) and recent (2011-2013) data, and thus provide unique and timely information to the overall objective of ice hazard risk mitigation.

1.3 Thesis structure

This thesis follows the 'Thesis as Papers' (manuscript-based thesis) submission format. A review of relevant literature to the ice island subject and overview of the methods used in this study is presented in Chapter 2. Chapters 3 (Deterioration modes of ice islands in the eastern and western Canadian Arctic regions) and 4 (Surface ablation model evaluation on a drifting ice island in the Canadian Arctic) are manuscripts intended for eventual submission to peer-reviewed journals (e.g. *Cold Regions Science and Technology, The Cryosphere,* or *Arctic, Antarctic and Alpine Research*). Both papers were structured and written by Anna Crawford, who also undertook data analysis and collection apart from an automatic weather station installation and four beacon deployments. Supervision during data collection and analysis, as well as document editing, was provided by Derek Mueller (M.Sc. supervisor and Assistant Professor in the Department of Geography and Environmental Studies). Concluding remarks

connecting the topics presented in the literature review and manuscript chapters are conveyed in Chapter 5. Throughout the thesis, figures are embedded within the text. Tables for the two manuscript chapters (3 and 4), are presented at the end of each chapter. A complete reference list is provided at the end of the document.

2.0 Literature Review and Methodology

The manuscripts presented in chapters 3 and 4 will examine the processes of horizontal (areal) and vertical ice island deterioration. This chapter reviews the background information on ice islands that will contextualize the study's importance. In particular, this chapter will examine the characteristics of ice islands (shape and size) and offer an historical review of this unique ice type. It then considers the activity and risk management strategies of the transportation and offshore oil and gas industries. Finally, current ice island sources, drift tracks and occurrence trends in the Canadian Arctic are detailed.

This chapter will also provide a review of the key methods employed in chapters 3 and 4: remote-sensing and surface ablation modeling. Improvement in remote-sensing technology has increased the capabilities of government agencies, private industry and collaborators to identify and monitor ice island size and location. General background regarding imaging ice islands with remotely-sensed data is explained in this section while surface ablation modeling is briefly introduced before being more fully described in Chapter 4.

2.1 Ice island morphology

Ice islands have been described as, "…the most massive ice features known in the Arctic Ocean" (Jeffries et al., 1987). They are akin to tabular icebergs due to their constant height above water and vertical sidewalls and are distinguished by their extensive areal dimensions (Fig. 2.1) (Rudkin et al., 2005; Peterson et al., 2009).
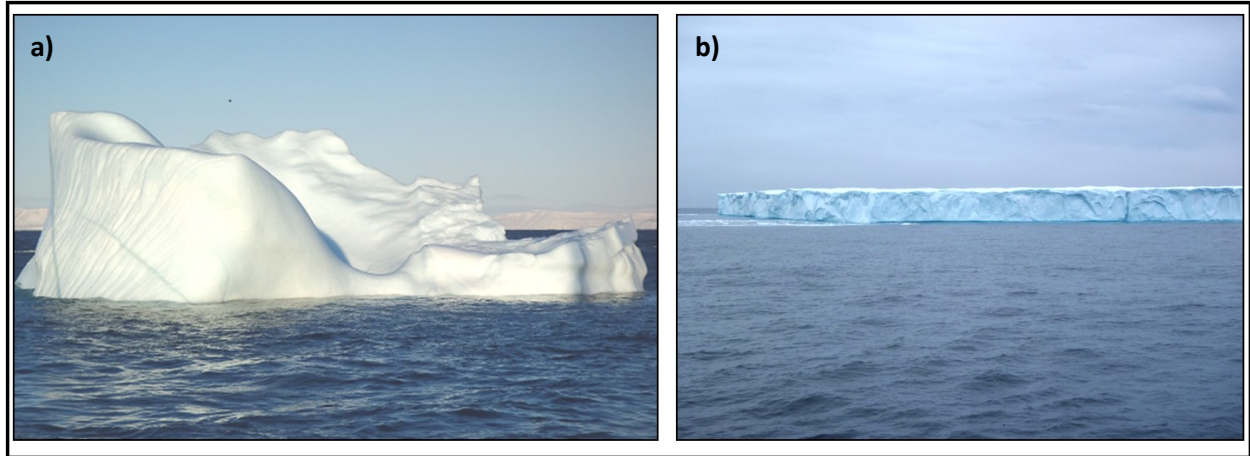
Figure 2.1: Comparing the size and shape of: a) a typical iceberg with 10 m approximate freeboard – Lancaster Sound, October 2011, and b) an ice island with 24 m approximate freeboard – Lancaster Sound, July 2011. Photos courtesy of a) Anna Crawford and b) Derek Mueller.

Ice islands range in surface area from a few square kilometers to over 500 km^2 (MANICE, 2005). Thicknesses for ice islands originating from the floating glacial tongues of northwest Greenland can range between 30 to 130 m, while those sourced from Ellesmere Island ice shelves range from 30 to 50 m (Rudkin et al., 2005; Forrest et al., 2012; MANICE, 2005). Freeboard (height above waterline) is greater than 5 m (MANICE, 2005). Figure 2.2 portrays terms familiar to ice island morphology. Ice islands originate from thick coastal ice, either ice shelves or floating glacier tongues, with their primary sources being those of Ellesmere Island and northwest Greenland (Rudkin et al., 2005). Ellesmere Island ice islands are distinguished by a ridge and trough surface structure, a remnant characteristic from their time as part of the island's ice shelves (Jeffries, 1992).

2.2 Climate change and ice island production

Arctic air temperature rose an average of 1.2°C decade[-1] from 1989 to 2008 (Screen and Simmonds, 2010). Air temperature anomalies have been positive since 2000, relative to both the 1971-2000 and 1981-2010 baseline periods (Fig. 2.3) (Overland et al., 2012; NCEP, 2013a) and some researchers have suggested that ice shelf and floating glacial tongue calving events are linked to this warming trend (Peterson, 2005; Copland et al., 2007).
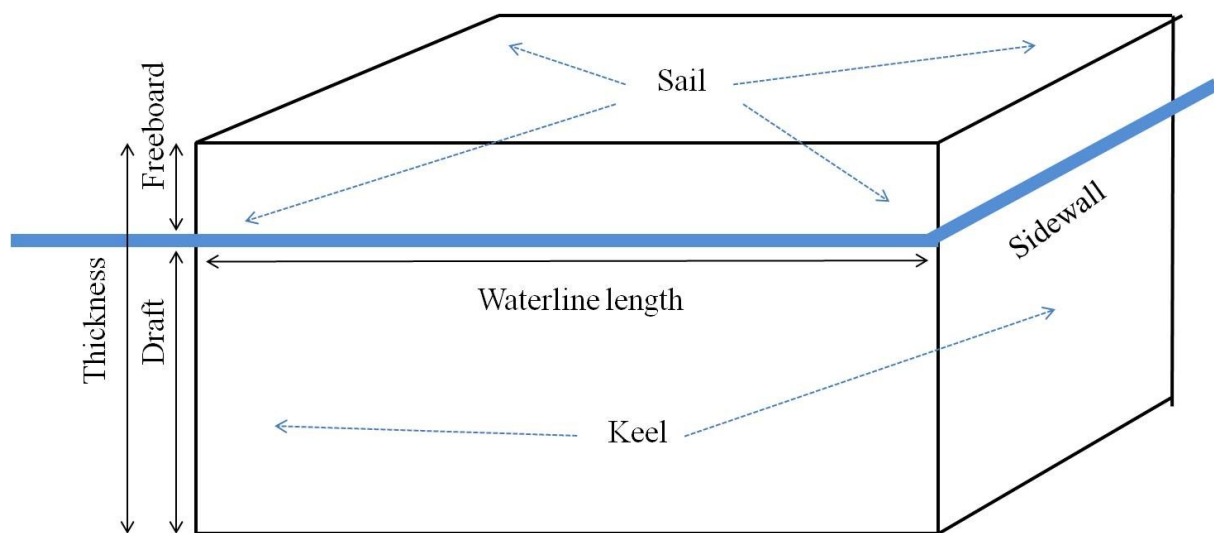
Figure 2.2: Ice island morphological terminology (not to scale).
The water surface is represented by a thick blue line.

Reduction in sea ice extent is another consequence of Arctic climate change. The loss of sea ice (pack and land fast sea ice) increases the chance of ice shelf and floating glacial tongue calving events. Sea ice acts as a barrier to wind and wave action and loss of this barrier has preceded calving events such as the 2005 calving of the Ayles Ice Shelf, Ellesmere Island (Copland et al., 2007). With Arctic sea ice dropping to a new record minimum in September 2012 (NSIDC, 2012) and studies predicting a summer ice-free Arctic Ocean by 2030 (Stroeve et al., 2008), this potential mechanism should continue to cause ice island calving events.
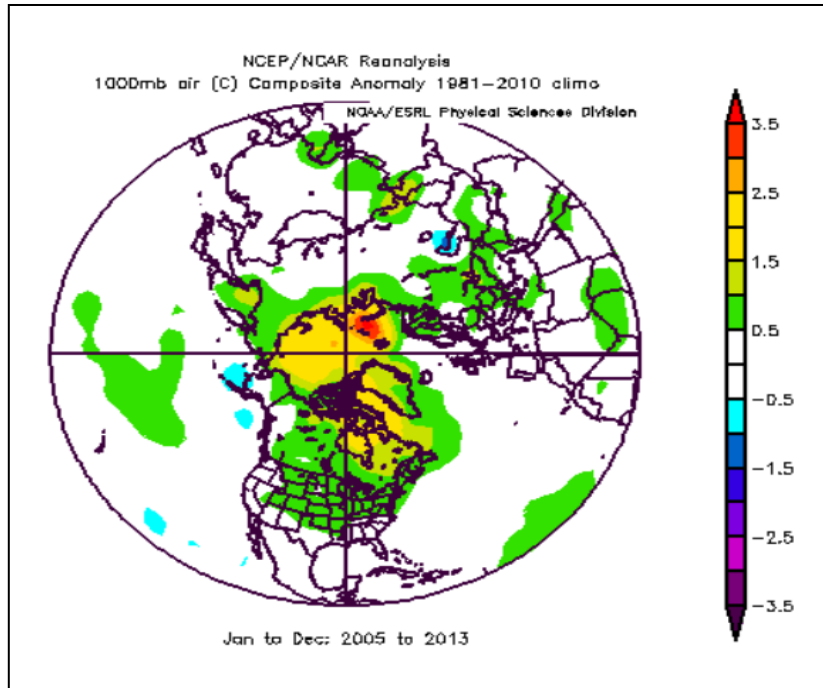
Figure 2.2: Northern Hemisphere average air temperature anomalies between 2005-2013 relative to a 1981-2010 baseline period. NCEP reanalysis data from NOAA/ESRL (Boulder, CO). http://www.esrl.noaa.gov/psd/ After Overland et al. (2012).

Rudkin et al. (2005) documented the increased occurrence frequency of ice islands in waters off the East Coast of Canada in the beginning of the 21st century. Peterson (2005) suggests that climate warming is the potential cause but also states that the terminus of the Petermann Glacier, the likely source of these ice islands, was within its historical limits in the early 2000s. However, Johannessen et al. (2011) and Falkner et al. (2011) found that the 2010 calving caused the terminus of the Peterman Glacier to retreat inland 15 km further than previously recorded. Rignot and Steffen (2008) determined that the Petermann Glacier is more vulnerable to weakening and subsequent calving due to increased ocean temperatures which increases basal ablation and sub-surface channelling. Minimal sea ice was recorded in the Petermann Glacier's outlet waters between 2006 and 2010 (Falkner et al., 2011). This may be

another factor in the 2010 calving event, as the floating glacial tongue no longer had a protective barrier from ocean forces (Falkner et al., 2011).

Climate change is believed to have also contributed to ice shelf calving events along Ellesmere Island's northern coast (Copland et al., 2007; Peterson, 2005). The loss of 87.1 km^2 of the Ayles Ice Shelf in 2005 was partly accredited to weakening through cumulative thinning related to an increase in mean temperature over the past 50 years (Copland et al., 2007). It is believed that the multiple, large calving events of Ellesemere Island in 2008 (detailed further below) were contributed to by low sea ice cover and open water conditions (McGonigal et al., 2011; Mueller et al., 2008). In addition to the lines of evidence that suggest that climate warming has a role in the calving of ice islands from Arctic ice shelves and floating glacial tongues, rising Antarctic ocean temperature is regarded as a contributor to the retreat of the Pine Island Glacier, West Antarctic Ice Sheet, Antarctica (Park et al., 2013).

2.3 Arctic offshore activity

Less sea ice will allow offshore activity to continue to increase in the Arctic region (Prowse et al., 2009). However, operations in the Arctic are still faced with unique challenges including interactions with ice hazards such as multi-year sea ice, icebergs and ice islands (McGonigal et al., 2011). Two sectors that will need to consider the hazards posed by ice islands are 1) natural resource exploration and extraction, and 2) shipping and marine transportation (Harsem et al., 2011). The reduced extent of sea ice in the Arctic has allowed for new opportunities in these activities (Valsson and Ulfarsson, 2011). Yet, Sackinger et al. (1991) state that ice islands are potentially the "...most serious hazard for Arctic offshore infrastructure".

The Beaufort and Chukchi seas are poised to experience increased activity with oil companies Imperial Oil Ltd., Exxon Mobile Corporation and British Petroleum obtaining

exploratory drilling leases (Beaufort Sea) and Royal Dutch Shell PLC beginning exploratory drilling in 2012 (Chukchi Sea) (McGonigal et al., 2011; McCarthy, 2012). Active drilling operations exist off Newfoundland's Grand Banks (Peterson et al., 2009) and ice islands are known hazards to these operations (Kubat et al., 2005).

Marine transportation through the Arctic is also poised to increase with the decreased extent and thickness of summer sea ice. This will likely include an expansion of shipping routes as well as tourism and the transport of natural resources to refineries overseas (Prowse et al., 2009). The opening of the Northwest Passage during the summer months could cause a surge of activity through the Canadian Archipelago, as it would drastically cut transportation times between regions of Asia and Europe (Valsson and Ulfarsson, 2011). The Northern Sea Route (Russia) and the Polar Route (over the North Pole) are also predicted to be navigable by mid-century (Stephenson et al., 2013). Ice islands pose a serious threat to these developing operations (Peterson, 2011) which reinforces the need for observations and adequate modeling of morphology, drift and deterioration of ice islands.

2.4 Drift and occurrence of ice islands in the Canadian Arctic

2.4.1 Eastern Canadian Arctic

Ice islands originating from northwest Greenland typically drift south through 'Iceberg Alley', transiting through Baffin Bay (Krajick, 2001) and continuing a drift trajectory along Canada's East Coast in the Labrador Current (Fig. 2.4) (Newell, 1993). The Petermann and Ryder glaciers and their corresponding floating glacial tongues, situated along the northwest coast of Greenland, are known to be sites of origin for ice islands in the Eastern Canadian Arctic (Peterson, 2005; Higgins, 1991).
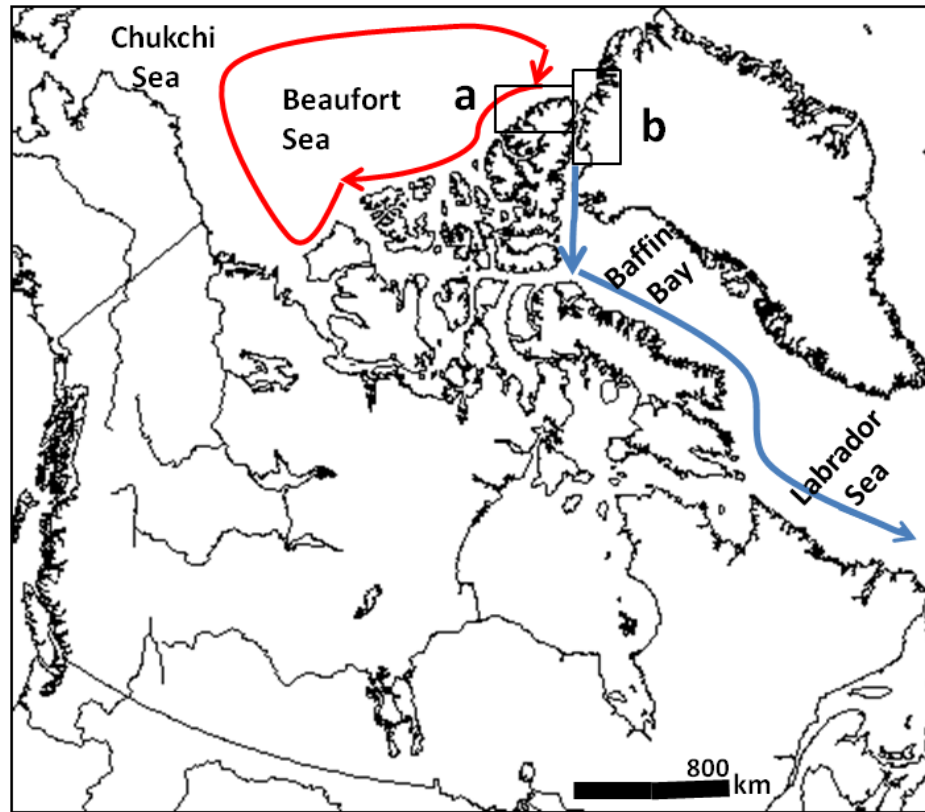
Figure 2.3: Common trajectories of ice islands adrift in the Canadian Arctic. Typical circulation of ice islands originating from Northern Ellesmere Island ice shelves (rectangle a) is shown in red. The normal route for ice islands originating from northwest Greenland floating glacial tongues (rectangle b) is shown in blue.

The multiple calving events of the Petermann Glacier have resulted in an increased occurrence of ice islands that eventually drift to more southern latitudes (Johannessen et al., 2011; Peterson, 2011). Of the glaciers located in northwest Greenland, the Petermann Glacier has the highest ice velocity with the last 50 km of the glacier terminus being afloat (a floating glacial tongue). Historically, ice island calving from the Petermann Glacier occurs at intervals between 5 or 10 years (Higgins, 1991). The glacier has been calving more frequently over the last 20 years with calving events in 1991, 2001, 2008, 2010 and 2012 (Johannassen, 2011; Environment Canada, 2012b). The 2010 Peterman Ice Island (PII), which calved on 5 August 2010 had an

original surface area of roughly 270 km^2. It has since fragmented into many smaller pieces, though many are still sizeable and are transiting south (Johannessen et al., 2011, L. Desjardins, pers. comm., 2011-2013). Three of these pieces were utilized as study cases in this thesis.

2.4.2 Western Canadian Arctic

Ice islands within the Western Canadian Arctic typically originate from the ice shelves of Northern Ellesmere Island (Jeffries 1992a) and commonly drift along the west coast of the Canadian Arctic Archipelago into the Beaufort and Chukchi seas (Fig. 2.4). If the ice islands get entrained in the Beaufort Gyre they may retrace their circular drift track up to 3 – 4 times, with the completion of each circuit taking 5 – 10 years (Jeffries et al., 1987). Since 2002, ice islands have originated from the break-up of a number of ice shelves along the northern coast of Ellesmere Island. This includes calving events at Ward Hunt, Ayles, Serson and Markham ice shelves between 2002-2011 (Copland et al., 2007; Vincent et al., 2009; McGonigal et al., 2011; Vincent et al., 2011; Mueller forthcoming). Five of these ice islands originating from northern Ellesmere Island were also monitored for deterioration analysis in Chapter 3.

2.5 Ice island deterioration

The modeling of processes which contribute to ice island deterioration and subsequent validation has proved difficult, due to the lack of *in-situ* data (Ballicater, 2012; Murphy and Carrieres, 2011). Deterioration models have attempted to represent mechanisms which directly influence surface ablation, mass loss by calving (break-off of relatively small ice pieces) and the melt of the submerged sidewalls and bottom surface (Fig. 2.5). Bottom melt (basal ablation) is not considered in this study as it was impossible to re-visit the study sites to assess the thickness change attributed to this process.

The five processes accounted for in the CIS operational iceberg deterioration model (Kubat et al., 2007, White et al., 1980) and identified as the main contributors to iceberg deterioration are: 1) buoyant convection, 2) forced convection from wind and water currents, 3) wave erosion, 4) calving of overhanging slab resulting from wave erosion and 5) solar radiation causing surface ablation (Fig. 2.5) (Savage, 2001). The percent contribution to overall deterioration due to each process is displayed in Table 2.1. Chapter 3 discusses the influence of the first four processes with respect to the rate and mode of ice island deterioration, while Chapter 4 focuses on surface ablation caused by solar radiation and wind generated forced convection.
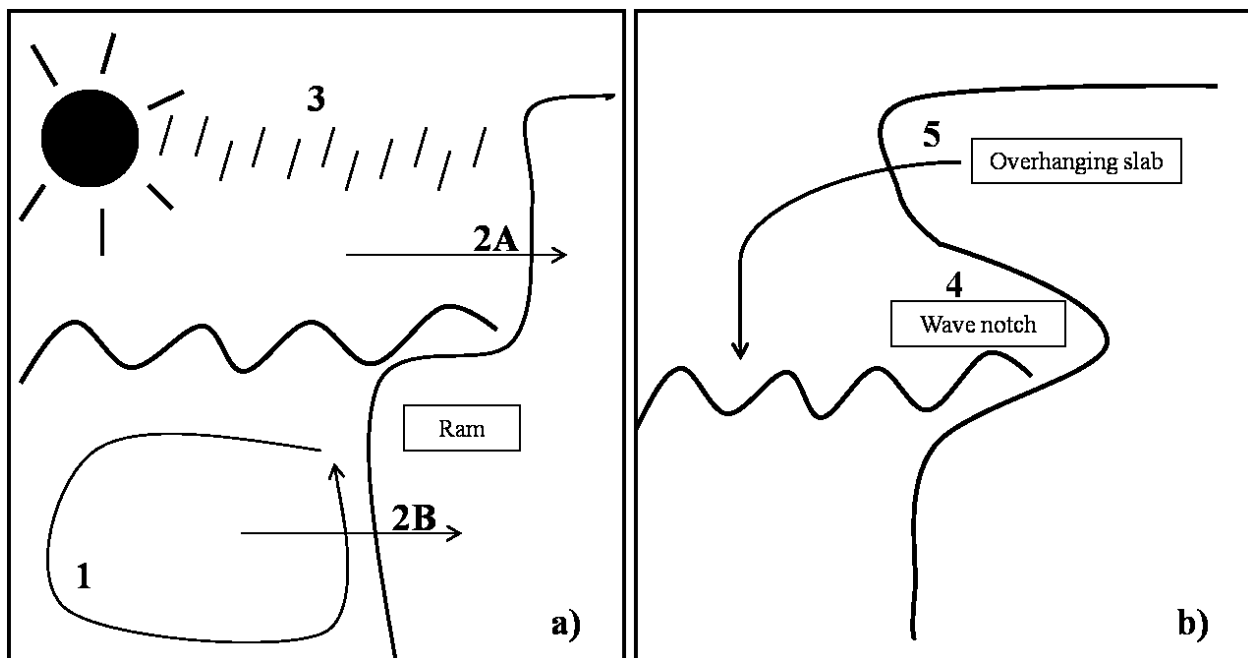
Figure 2.5: Side view of ice island deterioration processes: 1) buoyant convection cell, 2) forced convection from wind (2A) and water currents (2B), 3) solar radiation causing surface ablation, 4) wave erosion creating a wave notch, and 5) calving of an overhanging slab resulting from wave erosion. Conditions before and after the overhanging slab break off and creation of an underwater ram is depicted between a) and b).

Table 2.1: Contribution of mechanisms to iceberg deterioration. Based on studies of icebergs off the coast of Newfoundland and Labrador, the major forces of iceberg deterioration have been compared by Savage (2001) for their overall contribution.

Deterioration mechanism	Contribution to total loss %
Buoyant convection	1.2 - 1.5
Wind convection (forced)	0.3 - 2.9
Water current convection (forced)	11.3 - 24.9
Wave erosion	50.6 - 65.5
Calving of slab from wave erosion	21.0 - 29.5
Solar radiation causing surface ablation	0.3 - 5.3

Buoyant convection is caused by the production of iceberg melt water which is relatively fresh compared to the surrounding ocean water. The lower density of the melt water causes a circulation cell (Fig. 2.5) whereby water rises alongside the ice while the colder denser ocean water is displaced from the ice face and sinks (Savage, 2001). This circulation cell allows for the convection of heat from the water to ice surface, promoting melt of the submerged sidewall.

Forced convection occurs as sensible or latent heat is transferred to the submerged and emergent ice surfaces by water currents or wind, respectively. Melt due to forced convection is primarily caused by wind contact with the ice island surface above water, resulting in surface ablation as described in chapter 4. Wind and waves also influences the drift of icebergs and ice islands relative to the surrounding ocean. This generates forced convection as submerged ice comes in contact with surrounding water (Savage, 2001).

Wave erosion is typically the process that accounts for the greatest proportion of iceberg deterioration (Table 2.1). Wave-enhanced forced convection preferentially erodes a notch at the waterline and will cause a small calving event of the remaining, overhanging slab when an adequate depth and bending stress threshold is crossed (Savage, 2001). Field observations compiled by Vietch et al. (2001) confirm that wave erosion and calving are the mechanisms responsible for the greatest amount of deterioration. A sensitivity study was conducted by Kubat

et al. (2007) to determine which variables (air water temperature, waterline length, wind and water current velocities, wave period and wave height) most greatly affect iceberg deterioration. Wave height was found to be the most important variable as it influences the rate of wave erosion. This can then be directly linked to the frequency and magnitude of wave-notch calving events. Changes in water temperature and wind velocity also cause significant differences in deterioration rates (White et al., 1980; Kubat et al., 2007). These processes contribute to sidewall deterioration and fracturing of ice islands. Chapter 3 presents the first comparative study of sidewall deterioration rates and large-scale fracturing events for ice islands between the two Canadian Arctic regions.

Aside from the contribution from sensible and latent heat, the amount of energy for ice island surface ablation is determined by the net radiation. A large fraction of this comes from incoming shortwave radiation. The values of insolation vary greatly over the Arctic annually due to minimal winter daylight. Even in the summer, the presence of fog and/or cloud cover can decrease the amount of net radiation (longwave and shortwave) at the surface by up to 60% (Savage, 2001; Kubat et al., 2007). The amount of surface ablation experienced from solar radiation is also affected by the albedo (reflectivity) of the ice surface (Savage, 2001). Albedo values normally range from 0.4 to 0.5 for pure, glacial ice (Oke, 1987; Orelemans et al, 1999) but have been observed at 0.8 or greater (Oke, 1987; Savage, 2001).

2.6 Remote-sensing techniques for detecting and tracking ice islands

It is possible to assess ice shelf and glacier extents, determine the timing of calving events and locate drifting ice islands by utilizing various remote sensing techniques. It is feasible to monitor the areal extent of ice islands and thereby determine the amount of deterioration between

acquisitions by delineating the edges of ice islands, identified in satellite imagery, in geographic information system (GIS) software.

Real aperture radar (RAR) and synthetic aperture radar (SAR) are two airborne (or space-borne) remote sensing instruments that can operate through the winter dark and summer cloud cover (Jeffries, 2002). SAR is the preferred method of data collection due its increased resolution in the azimuth (flight-path) direction of the image swath (Fig. 2.6). SAR records and processes a sequence of signals, resulting in azimuth resolution that is independent of sensor-to-surface distance unlike RAR (ESA, 2013). SAR antennas transmit energy pulses (microwaves whose wavelengths are between 4 and 8 cm) towards Earth (UNOOSA, 2013). The receiver will detect the backscattered energy and organize these responses in range direction based on the two-way travel time (transmitter – surface – receiver) (Bamler and Hartl, 1998). It is necessary for the radar to be side looking so that the corresponding location on Earth of each energy response can be differentiated by two-way travel time (Mott, 2007). Backscatter power (which is displayed as pixel brightness) in processed imagery is controlled by the physical and chemical structure of the surface; for ice this includes air space (in)-homogeny, dielectric constants and surface roughness (ESA, 2013).
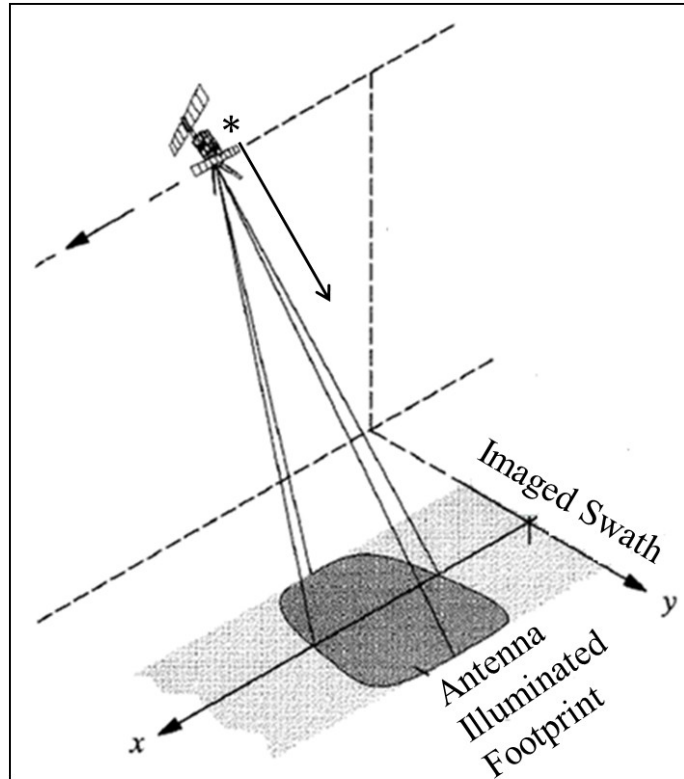
Figure 2.6: Synthetic aperture radar (SAR) basic geometry. SAR is preferred over real aperture radar due to increased resolution in the azimuth (along-track) direction (x). SAR has a side looking configuration (*). y denotes 'ground range' or width of imaged swath. Modified from Bamler and Hartl (1998).

Jeffries and Sackinger (1990) examined the use of airborne SAR imagery to identify and characterize ice islands in the Canadian High Arctic. This was the first systematic study to use remote sensing for ice island identification and characterization. RADARSAT-2 beam modes were most recently analyzed for best ice island identification practices by the CIS and Defence Research and Development Canada for the Canadian Space Agency (De Abreu et al., 2011). Ice islands, due to the greater freshwater content in comparison to surrounding saline ice floes, return a relatively stronger radar signal to the receiver. The greater salinity of ice floes results in increased attenuation of the radar signal and a darker tone in imagery (Jeffries and Sackinger, 1990). Ice islands will normally have a brighter appearance in the SAR imagery but depends if

the ice island's surface ice is of atmospheric or marine origin (Fig. 2.7) (De Abreu et al., 2011). Imagery can detail the ice island's ridge and trough surface relief and define the angular ice edge which has an even brighter radar return. Both are characteristics differentiating an ice island from the surrounding sea-ice, along with their extensive size (Jeffries and Sackinger 1990).

Ice islands in both the Arctic and Antarctic have been and are currently monitored (size and location) by numerous satellite systems, including MODIS, ICESat, Envisat and RADARSAT-2 (Scambos et al., 2005; Scambos et al., 2003; Peterson et al., 2009; Jeffries, 2002). Recently in the Arctic, Peterson (2009) used a combination of Envisat and MODIS satellite imagery to track the 2008 PII to southern Baffin Island.
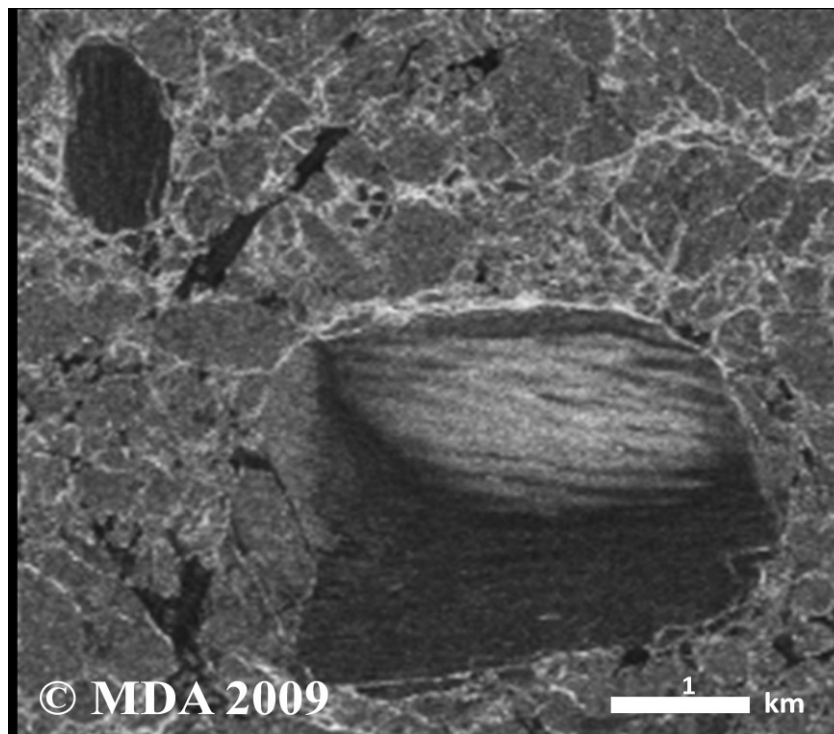
Figure 2.7: RADARSAT-2 satellite image depicting the contrasting tones of marine (darker) and meteoric, atmospherically derived (brighter return), ice constituting parts of ice island 'M3' (origin: Markham Ice Shelf, Ellesmere Island). 9 November 2009. After De Abreu et al. (2011). RADARSAT-2 Data and Products © MacDONALD, DETTWILER AND ASSOCIATES LTD. (2011) – All rights reserved. RADARSAT is an official mark of the Canadian Space Agency.

Ice shelf extents and calving events are also documented by remote sensing. Envisat, MODIS and RADARSAT-2 imagery was used to document the 2010 Petermann Glacier calving event (Fig. 2.8) (Johannessen, 2011; NASA, 2010; L. Desjardins, pers. comm. 2010). MODIS and RADARSAT-2 imagery was used to monitor the fracturing and separation of the Ellesmere Island ice shelves in 2005 and 2008 (Copland et al., 2007; Vincent et al., 2011).

Figure 2.8: A MODIS image captured the calving of the Petermann Glacier on 5 August 2010. Source: NASA Earth Observatory. Image acquired 5 August 2010. http://earthobservatory.nasa.gov/NaturalHazards/view.php?id=78556

Cryospheric remote sensing has become more sophisticated over time and there is commitment to further develop these remote sensing capabilities. This demonstrates their utility for monitoring the evolving cryosphere that is challenging to document due to the difficulty of performing field surveys in the Polar Regions. These technological advancements, especially in initial ice island identification, should be taken into consideration when assessing ice island occurrence frequency (McGonigal et al., 2011), as they enhance identification capabilities. This is most important for areas far afield from ice island source locations (i.e., Grand Banks, NL).

2.7 Surface ablation modeling

Surface ablation models can be developed at various levels of complexity. This thesis explores two surface ablation forecasting methods including two different physically based energy-balance (EB) models and an empirical temperature-index model (TIM) (Hock 2003). The two EB models are the operational CIS iceberg (Kubat et al., 2007) and ice island (Ballicater, 2012) surface ablation models while the TIM is a glacial model developed by Hock (2003).

2.7.1 Energy balance modeling

Energy-balance models utilize physical equations to represent radiative and turbulent fluxes affecting the ice surface (Hock, 2005). When all fluxes are accounted for the energy available for melt is represented as:

$$Q_M = Q_N + Q_S + Q_E + Q_G + Q_R \tag{2.1}$$

where Q_M is available melt energy, Q_N is the net radiative flux, Q_S is the sensible heat flux, Q_E is the latent heat flux, Q_G is the ground or ice heat flux and Q_R is the energy provided by precipitation.

The net radiative flux (Q_N) is usually considered the most important variable in surface ablation modeling (providing two-thirds of available melt energy), however the inclusion of the turbulent fluxes (Q_S and Q_E) may improve model performance (as these fluxes typically provide much of the remaining melt energy) (Knox, 2011; Male and Gray, 1981; Braithwaite, 1995).

The net radiative flux is composed of four variables:

$$Q_N = L\!\downarrow + L\!\uparrow + K\!\downarrow + K\!\uparrow \tag{2.2}$$

where $L\!\downarrow$ is incoming longwave radiation, $L\!\uparrow$, is emitted longwave radiation, $K\!\downarrow$ is incoming shortwave radiation and $K\!\uparrow$ is reflected shortwave radiation.

Sensible and latent fluxes are convective energy exchanges (Oke, 1987). Q_S exchange occurs when there is a temperature gradient between the atmosphere and ice surface (Oke, 1987), while latent heat is either released or stored at the ice surface with the phase change of water (Knox, 2011; Aguado and Burt 2007). The CIS ice island model represents both Q_S and Q_E with equations 2.3 and 2.4, respectively.

$$Q_S = \rho_a \, c_{pa} \, C_S \, \Delta U_s \, (T_a - T_s) \tag{2.3}$$

$$Q_E = \rho_a \, L_v \, C_E \, \Delta U_s \, (0.622 \, p^{-1})(e_s - e_a) \tag{2.4}$$

where ρ_a is air mass density (1.29 kg m^{-3}), c_{pa} is dry air specific heat (1006 J kg^{-1} K^{-1}), C_S and C_E are the sensible and latent heat exchange coefficients, respectively, ΔU_s is the wind speed differential between 10 m and the surface (m s^{-1}), T_a is air temperature (K), T_s is ice temperature (273.15 K), L_v is the latent heat of vaporization (2.501 x 10^6 J kg^{-1}), p is atmospheric pressure, e_s is surface vapour pressure (610 Pa) and e_a is atmospheric vapour pressure (Pa) (Ballicater, 2012; Knox, 2011).

Q_G is often ignored by EB models for surface ablation of ice. An assumption of the bulk aerodynamic approach (BAA) is that energy is not exchanged with the below-surface ice (Hay and Fitzharris, 1988) and was valid in a previous glacial study during the melt season (Marcus et al., 1985). Q_R may also be ignored as it is assumed that heat exchange from rain is negligible to the radiative and turbulent fluxes (Braithwaite, 1995). Both are omitted from the CIS iceberg and ice island models.

The resulting rate of surface ablation is then:

$$R = Q_M/(\rho_i \Gamma) \tag{2.5}$$

where R is rate of surface ablation (m per time step), ρ_i is ice density (0.9 kg m^{-3}) and Γ is the latent heat of fusion for ice (3.34 x 10^5 J kg^{-1}).

The CIS iceberg deterioration model represents surface ablation with a simple, three parameter equation, calculating surface ablation rate with $K\downarrow$ as the sole input variable and albedo (α) set to 0.7 (Savage, 2001). The remaining radiative and turbulent fluxes are omitted (Kubat et al., 2007).

Ice island surface structure differs from icebergs in that areal extents are much greater and are essentially horizontal to the ocean's surface. Surface ablation thus plays a larger relative role in ice island deterioration modeling than for an iceberg (Ballicater, 2012) and needs adequate model calibration and validation. The development of an ice island-specific deterioration model has begun at the CIS (Ballicater, 2012; Crocker et al., 2013). The geometric parameterization of the CIS/North American Ice Service (NAIS) model (Murphy and Carrieres, 2010) was altered to adequately represent an ice island's tabular structure in the new model. The model uses the BAA, a profile method to determine the vertical, convective fluxes of momentum, heat and water vapour (Oke, 1987). Use of the BAA allows the EB to be calculated via measurements of T_a and U_s at one height above the ice surface (Ballicater, 2012; Hay and Fitzharris, 1988). Q_S, Q_E and Q_N are used to determine Q_M. Longwave radiative fluxes are calculated using the Stephan-Boltzman relationship and the respective atmospheric or ice emissivity and temperature values. $L\uparrow$ is held at 306 W m^{-2} with the use of parameterized T_s and ε_s (emissivity of ice) values. $L\downarrow$ calculation utilizes T_a as an input variable, but relative humidity (RH) values parameterized (at 75%) for the calculation of ε_a (atmospheric emissivity). Insolation (I, or absorbed shortwave radiation, $K\downarrow$ - $K\uparrow$) is held constant at 40.7 W m^{-2}, α at 0.8 and $K\downarrow$ as 203.5 W m^{-2} during operational model runs (Ballicater, 2012).

In addition to the greater detail in Q_N calculation, Ballicater (2012) and Crocker et al. (2013) calculate and include Q_S (Eq. 2.3) and Q_E (Eq. 2.4) using constant turbulent exchange coefficients (C_s and C_E) (Esbensen and Reynolds, 1981). Wind speed, ice roughness and

atmospheric stability all influence these coefficients and are included in the model by Ballicater (2012).

2.7.2 Temperature index modeling

TIMs, or 'degree day models' assumes a relationship between T_a, time (as 'positive temperature sums' input) and surface ablation (Hock, 2003; Braithwaite, 1995), without the use of solar radiation as an input variable. Since T_a is highly correlated with the three most important energy sources for ice melt ($L\downarrow$, I and Q_s) and resulting surface ablation (Braithwaite and Olesen, 1993; Ohmura, 2001), it can be argued that it is an appropriate substitute when creating a simple surface ablation model. Positive degree days (PDDs) are related to surface ablation (M) by the degree day factor (DDF) which can be influenced by local conditions via α and turbulence (Arendt and Sharp, 1999).

$$\sum_{i=1}^{n} M = \text{DDF} \sum_{i=1}^{n} \text{PDD}\Delta t \tag{2.6}$$

where Δt is the time step (hr).

It is important to use the correct DDF value for the site being modeled, as slightly altering the DDF value will result in a large change in surface ablation prediction. DDFs can be calculated from T_a records, direct surface ablation measurement (lysimeter or surface ablation stakes) or surface ablation prediction from EB calculations (Hock, 2003). Maritime environments, such as an ice island, have low DDFs due to high turbulent heat fluxes which are a result of high T_a and U_s. Turbulent fluxes are also greater than inland locations at increased elevations. Albedo can also influence DDFs. It has been suggested to alter the model DDF throughout the year as site conditions evolve; however, changes are less dramatic for ice cover in comparison to snow (Hock, 2003; Braithwaite and Olesen, 1993). If conditions do not change considerably it may not be necessary to modify the DDF (Hock, 2003). Arendt and Sharp (1993)

suggest that PDDs are ideally calculated from T_a measurements. This is possible with data provided by an *in-situ* weather station but PDD input would be calculated from forecast estimates in operational deterioration models. A benefit of a TIM is that it lends itself to being run for operational use with regional reanalysis or forecasted T_a data which is most readily available to operational modelers. Data sources would include the National Center for Atmospheric Research/National Centers for Environmental Prediction (NCEP/NCAR) reanalysis data (Kalnay et al., 1996) or the Global Environmental Multiscale (GEM) model.

2.8 Knowledge gaps and conclusion

Updating the current iceberg deterioration model in use by the CIS for ice islands and deterioration monitoring via satellite imagery will provide relevant information to offshore stakeholders such as the natural resource and shipping industries. This will result in prudent offshore risk assessment and management plan development to mitigate the risk of a disastrous oil spill or ship collision in the sensitive Arctic environment.

The ability for an ice island to drift allows it to come into contact with varying atmospheric and oceanic conditions within a relatively short time frame. As they are originally sourced from ice shelves, the deterioration processes caused by evolving climatic variables (namely warmer atmospheric and ocean temperatures) can be compared to what will happen to ice shelves as climate change continues in the Polar Regions (Scambos et al., 2005). Thus, a better understanding of ice island deterioration may be applicable to other cryospheric features also affected by global climate change.

Field observations of ice islands are logistically difficult to obtain and it is therefore necessary to combine various methods of observation. This thesis utilizes remote-sensing (Chapter 3), *in-situ* microclimate and surface ablation records and modelling efforts (Chapter 4)

in the attempt to provide a complete representation of the processes contributing to ice island deterioration. Remote-sensing aids in monitoring ice island location and areal dimensions while adrift in Arctic waters, and regional *in-situ* data gathering is imperative for model calibration and validation. It is important that drift and deterioration models are calibrated when in Arctic waters so that accurate forecasting is possible when the models are applied to ice islands in this region. Deterioration model output is used as input for drift models; therefore, correct ice island dimensional output from deterioration modeling is important for accurate drift forecasting. The processes contributing to ice island deterioration are often sub-satellite resolution, furthering the need for on-site field work. This thesis details ice island deterioration in both the horizontal (areal) extent (through remote-sensing) and the vertical extent associated with surface ablation and will contribute pertinent, operationally-applicable knowledge on ice island for use by offshore stakeholders.

Deterioration modes of ice islands in the Eastern and Western Canadian Arctic regions

3.1 Introduction

Ice islands were first observed in North America during the 1940s and were used as floating, scientific research platforms by the United States and Canada between 1952 and 1992. The ice islands were utilized and studied while drifting from northern Ellesmere Island to the Beaufort and Chukchi seas, Arctic Ocean or within the Canadian Arctic Archipelago (CAA) (VanWychen and Copland, forthcoming; Belkin and Kessel, forthcoming; Jeffries, 1992; Jeffries and Shaw, 1993; Koenig et al., 1952).

Ice island surface areas can range from a few thousand square meters to over 500 km^2 (Jeffries, 1992a; MANICE, 2005; McKenna, 2005; Peterson et al., 2009). There are two source regions for ice islands drifting in Canadian waters. Ice islands observed in the Eastern Canadian Arctic (ECA) are normally of glacial (terrestrial) ice origin from northwest Greenland (Petermann and Ryder glaciers). These ice islands follow a common drift route south through Nares Strait and along the east coast of Baffin Island (Halliday et al., 2012; Tang et al., 2004; Higgins, 1989) (Fig. 2.4) and have been observed as far south as the Grand Banks (Peterson et al., 2005; Peterson, 2009). Ice islands observed in the Western Canadian Arctic (WCA) calve from Ellesmere Island ice shelves and are composed of meteoric and/or marine ice. Meteoric ice is either glacial ice or iced firn (accumulation of ice through snow transformation or rainfall). Marine ice accumulates from the underside of an ice shelf (basement ice) or can be multiyear landfast sea ice (Mueller et al., 2006). These ice islands normally drift southwest and can entire the CAA or continue along the west coast of the CAA and into the Beaufort and Chukchi seas, where recirculation in the Beaufort Gyre is possible (De Abreu et al., 2011; Jeffries, 1992) (Fig. 2.4). There was a decrease in the rate of ice island calving for the eastern and western Canadian Arctic regions, between 1960-1990 and 1970-2000, respectively (Newell, 1991;

Vincent et al., 2011; Mueller, forthcoming). However, calving events from thick coastal ice (floating glacial tongues and ice shelves of northwestern Greenland and Northern Ellesmere Island, respectively) have caused an increased number of ice islands to be produced and consequently observed off the east coast of Canada (Newell, 1993; Rudkin, King, Ralph and Stoermer, 2005; Stoermer and Rudkin, 2003; Peterson, 2005; Peterson, 2011) and in the Arctic Ocean since the early 2000s (Copland et al., 2007; Derksen et al., 2012; Vincent et al., 2011). This is cause for concern as both the ECA and WCA regions are proposed areas for increased offshore activity (Prowse et al., 2009) and ice islands are recognized hazards for offshore industrial operations including shipping, resource exploration and subsequent extraction (McGonigal et al., 2011; Peterson, 2011; Prowse et al., 2009).

The common drift trajectories taken by ice islands within the two regions results in the ice islands of the ECA reaching southern latitudes and corresponding warmer environmental conditions (air and ocean temperatures, sea ice conditions) more quickly than ice islands adrift in the WCA, which may play a role in determining how these ice features deteriorate (Scambos et al., 2005).

Three modes of deterioration have been identified using MODIS satellite imagery for large, tabular icebergs of Antarctica. Antarctic icebergs are analogous to Arctic ice islands but with increased thickness and surface dimensions. These modes are (1) edge-wasting, where separated fragments are still identifiable in satellite imagery and the overall shape of the parent ice island remains intact, (2) rift-calving/fracturing events, where calving results in 2 or more daughter ice islands that do not resemble the parent (original) ice island and (3) rapid disintegration, where calved ice is small enough to be sub-satellite resolution (Scambos, 2009; Scambos et al., 2005; Scambos et al., 2008). Scambos et al. (2008) describe 'disintegration' to be a summer phenomenon, usually overlapping with the presence of melt water on the top of the

berg. This results in rapid calving events due to hydro-fracturing. Large fracturing events are difficult to predict but are the cause of the majority of an ice island's deterioration (Ballicater, 2012). Scambos et al. (2005) find fracturing events to often occur along surface erosion features, which were apparent when the iceberg was still intact with the original ice shelf.

In this study of Arctic ice island deterioration, three modes of deterioration are proposed and are defined by the areal loss rate which occurs to an ice island while within the respective mode. These modes are: (1) fracturing (≥ 0.2 km^2 d^{-1}), (2) fragmentation (between 0.1 and 0.2 km^2 d^{-1}), where daughter fragments are likely visible in 8 m resolution satellite imagery but the overall ice island shape remains unchanged, and (3) decay (≤ 0.1 km^2 d^{-1}), which is small-scale deterioration where calved pieces are not visible in 8 m resolution satellite imagery. Figure 3.1 illustrates the fracturing and fragmentation modes of deterioration. The sizes of these events are analogous in terms of relative magnitude to the deterioration modes of Antarctic tabular icebergs. The classification terms of deterioration modes in this study (fracturing, fragmentation and decay) are analogous to the terms utilized by Scambos et al. (2008) (edge-wasting, rift-calving and disintegration, respectively). The terms were modified since the reasons for and times of their occurrence may differ.
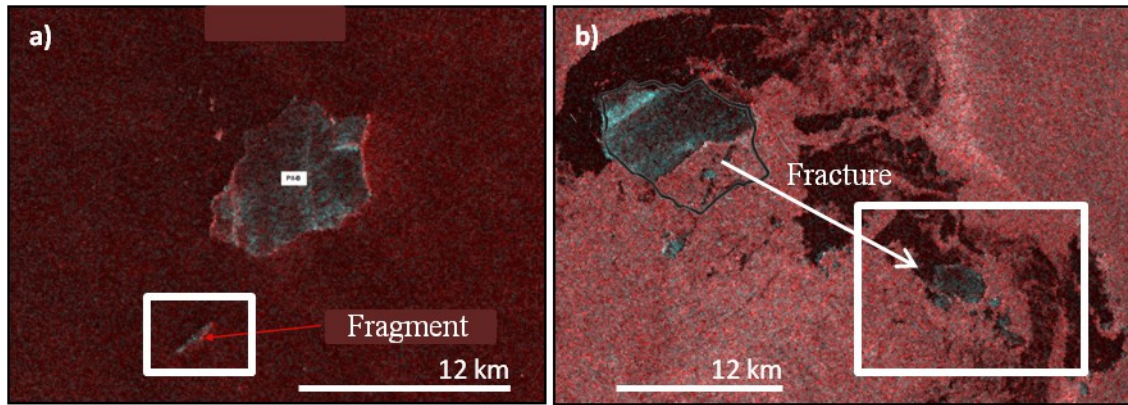
Figure 3.1: Ice island deterioration modes demonstrated with RADARSAT-2 images of Petermann Ice Island (PII)-B. Image a) illustrates the fragmentation deterioration mode (2011-10-16) and b) depicts PII-B after experiencing a fracturing event (2011-11-16). Resulting fragments are enclosed in white boxes. Images are courtesy of L. Desjardins (CIS).

This study's aim is to characterize Arctic ice islands' deterioration modes and determine if these modes are associated with the ice island's source region (ECA or WCA), sea ice concentration and/or environmental conditions. The annual duration and concentration of sea ice will differ for an ice island depending upon its origins and drift track. Similarly, environmental conditions (air temperature (T_a) and sea surface temperatures (SST)), will also vary along the ice islands' trajectories. It is hypothesized that the deterioration mode experienced by the ice island is associated with the surrounding sea ice concentration and regional air and ocean temperatures.

To evaluate this hypothesis, satellite imagery (RADARSAT-2) was acquired for a set of ice islands in the two source regions that were being monitored with global positioning system (GPS) tracking beacons. Deterioration rates and deterioration modes were classified using this imagery to assess loss of surface area. Mass loss was calculated for ice islands within the ECA with measurements of surface area, ice thickness recorded with ground penetrating radar (GPR) and estimations of surface ablation.

This multi-year study monitored the deterioration of seven ice islands in the Canadian Arctic and estimated the mass and quantity of fragments which result from their deterioration. This research will contribute to the understanding of ice island deterioration processes and provide relevant ice hazard information to offshore stakeholders. The validation and improvement to operational ice island drift and deterioration models (Kubat et al., 2005; Kubat et al., 2007) will then aid in the prediction of ice hazard size and frequency in Canadian waters.

3.2 Study Sites

3.2.1 Eastern Canadian Arctic

Two ice islands in the ECA were accessed in October 2011 during Leg 3b of ArcticNet's Arctic Research Cruise on board the *CCGS Amundsen*. Both were fragments of the 2010 Petermann Ice Island (PII) which calved from the floating glacial tongue of the Petermann Glacier, northwest Greenland (81°N, 61°W) on 5 August 2010 (Fig. 3.2, Table 3.1). At the time of calving, the 2010 PII was 270 km^2 (approximately 28 km x 15-20 km) (Johannessen et al., 2011). PII fragmented between 9 September and 16 Sepember, 2010 and created 4 ice islands: PII-A, B, C & D. PII-B-a calved from PII-B in early October 2010 (L. Desjardins, pers. comm., 2010). PII-B and PII-B-a (Figs. 3.3 and 3.4, Table 3.2) were utilized as case studies for this research as they were along the CCGS *Amundsen's* cruise track and readily accessible by helicopter.

Fracturing events, like those sustained by PII in September 2010, lead to daughter fragments (the original ice island would be the parent). A naming convention has been developed where the daughter fragments keep the stem name (e.g. 'PII-B') and add letters or numbers, alternating as subsequent daughter fragments are created. If one resulting ice island is obviously

larger than the others, post-fracture, it may keep the original stem name with no additions (L Desjardins, pers. comm, 2012).
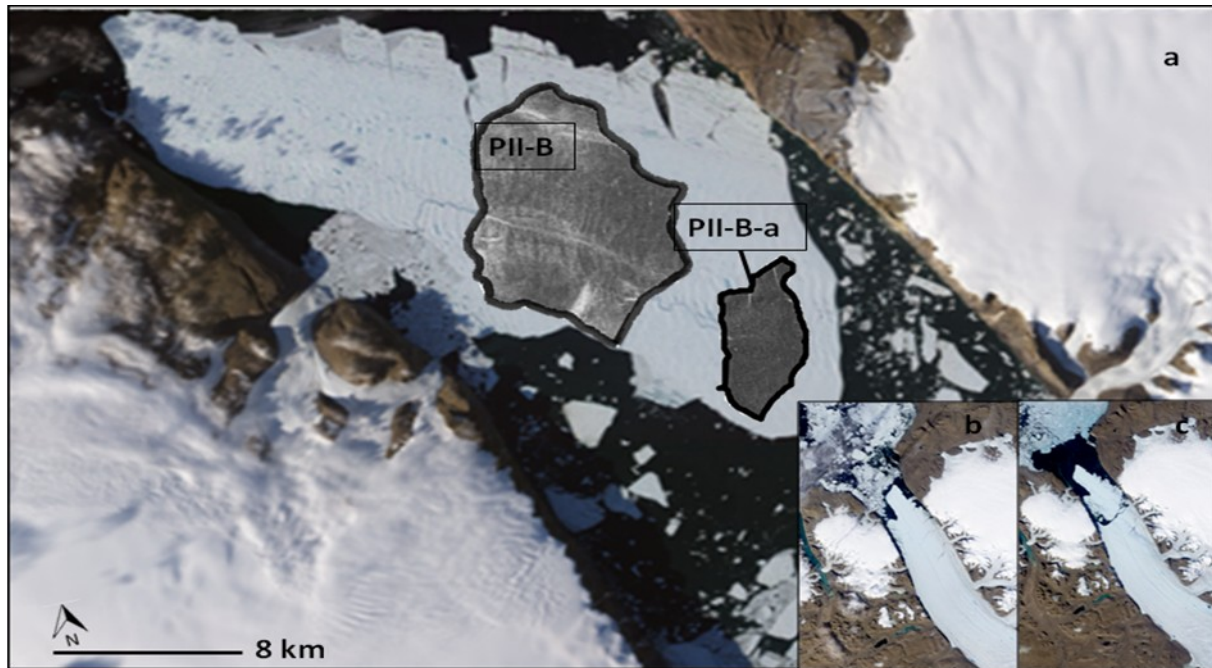
Figure 3.2: 2010 Petermann Ice Island (PII) calving event from Petermann Glacier, northwest Greenland. Images are courtesy of NASA MODIS Earth Observatory (EO-1 ALI Aqua satellite). a) PII post-calving, with slight rotation and drift towards mouth of fjo the fjord (2010-08-16), b) Petermann Glacier pre-calving (2010-07-21), c) PII on the day after the calving event (2010-08-05). Ice islands utilized as field sites in this study, PII-B and PII-B-a, are overlain with their *in-situ* position within the original PII in a).

PII-B-a was accessed on 13 October 2011 when located in Lancaster Sound (74°15'N, 87°54'W). It was 6.1 x 2.8 km, with a surface area of 12 km^2 and a freeboard of approximately 15 m. PII-B-a had been previously visited in July 2011 with a group from the *CCGS Amundsen* to deploy a GPS tracking beacon. PII-B (69°38'N, 65°52'W) was accessed on 22 October 2011. At the time, PII-B was grounded on a shoal near Cape Raper, 130 km southeast of Clyde River, NU. The ice island was 11.7 x 7.7 km, with a surface area of 59 km^2 (Fig. 3.3). Freeboard was approximately 8 m. Adverse weather conditions during field work on PII-B allowed for the

establishment of only two sample sites. PII-B was re-visited in August 2012 while it was still grounded at the same location. The surface area of PII-B had decreased to 38 km^2 (9.4 x 5.0 km) between the two field visits.
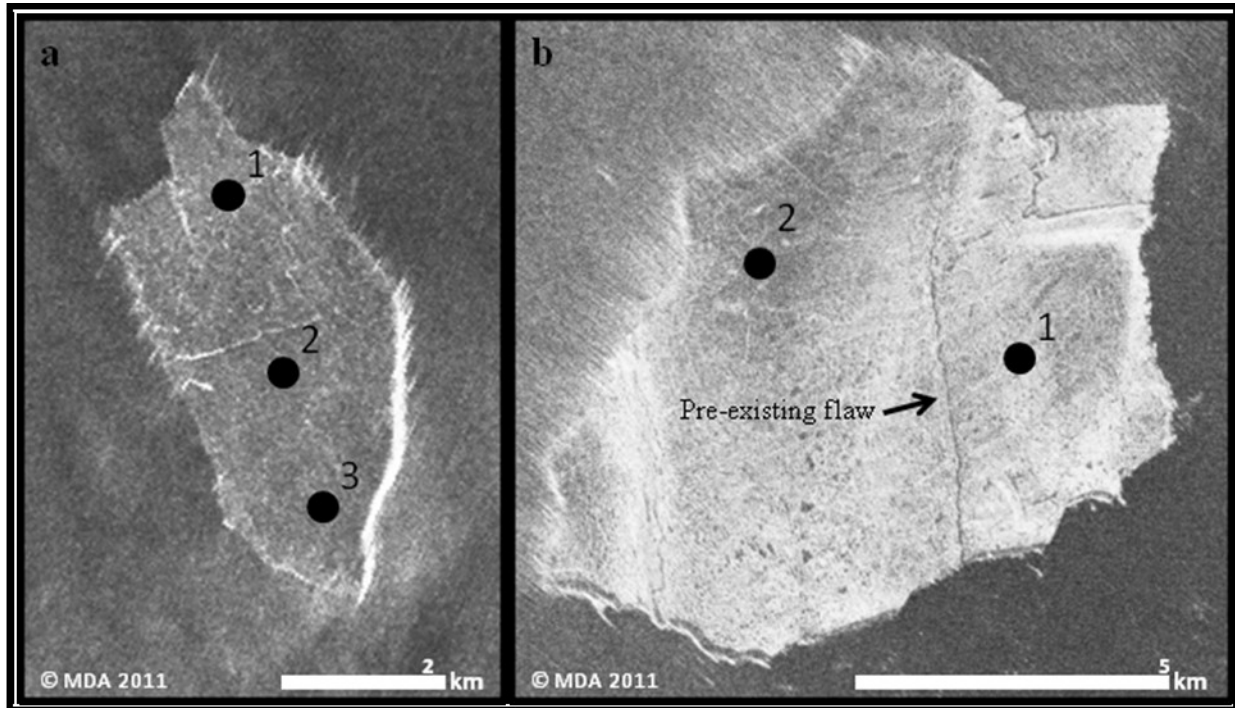
Figure 3.3: Beacon deployment and thickness/freeboard measurement sites on a) PII-B-a, 2011-10-06 and b) PII-B, 2011-10-08. Refer to Figure 3.5 for locations. All images are Radarsat-2 Fine-Quad, © MDA 2011. All images are RADARSAT-2 Fine-Quad © MDA.
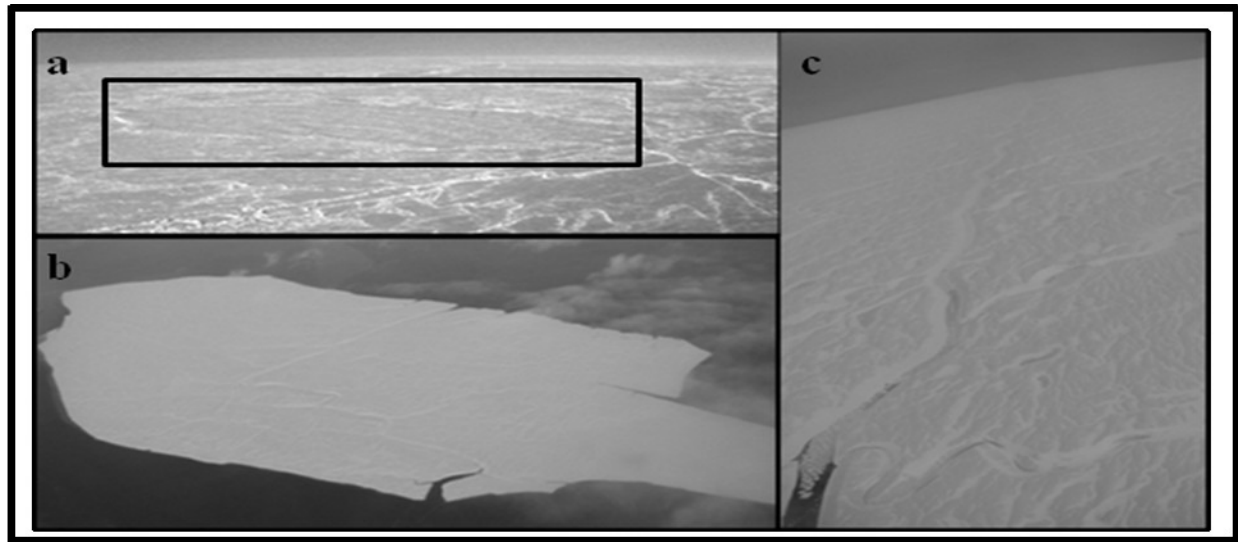
Figure 3.4: Aerial photographs of ice islands showing the: a) limited freeboard of M3, 2012-04-13 (photo courtesy of Klaus Hochheim – University of Manitoba), b) PII-B-a, 2011-10-12, c) pre-existing erosion feature of PII-B, 2011-10-22 (see Figure 3.3).

3.2.2. Western Canadian Arctic

Five ice islands, originating from the Ward Hunt and Markham ice shelves of northern Ellesmere Island (Figs. 3.5 and 3.6, Tables 3.1 and 3.2), drifted along the west coast of the CAA and into the southern Beaufort Sea. These ice islands were previously tracked during a joint study co-sponsored by the CIS and Canatec and Associates Ltd (De Abreu et al., 2011).

The ice islands 'Ward Hunt 1' (WH1) and 'Ward Hunt 2' (WH2) originated from the Ward Hunt Ice Shelf, which lost 42 km^2 during the summer of 2008 (83°02'N, 74°00'W) (De Abreu et al., 2011). WH1 was composed of meteoric and multiyear ice while WH2 was primarily meteoric ice with a small amount of marine ice (De Abreu et al., 2011). WH1 and WH2 were known as 'Target 1' and 'Target 2', respectively in the work by De Abreu et al. (2011) (Fig. 3.5, Table 3.2).

'Markham 1' (M1) and 'Markham 2' (M2) (also referred to as 'Target 7' and 'Son of Seven', respectively; De Abreu et al. 2011) originated from the Markham Ice Shelf (83°03'N, 71°20'W).

These ice islands were created when the entire ~50 km^2 ice shelf collapsed and drifted away in 2008 (Mueller, Vincent and Jeffries, 2009; Mueller et al., 2008) (Fig. 3.6). The fifth ice island, 'Markham 3' (M3), was also a fragment of the Markham Ice Shelf (Fig. 3.5). This ice island was first accessed on 19 April 2010 at 79°42'N, 106°54'W. The ice island was visited accessed by helicopter on 7 and 13 April 2012 at 72°21'N, 127°29'W, 88 km west of Sachs Harbour, NT. The ice island was surrounded by sea ice and freeboard was < 2-3 m,. Freeboard was difficult to discern as the surrounding sea ice appeared level with the ice island surface (Fig. 3.4, Table 3.2).
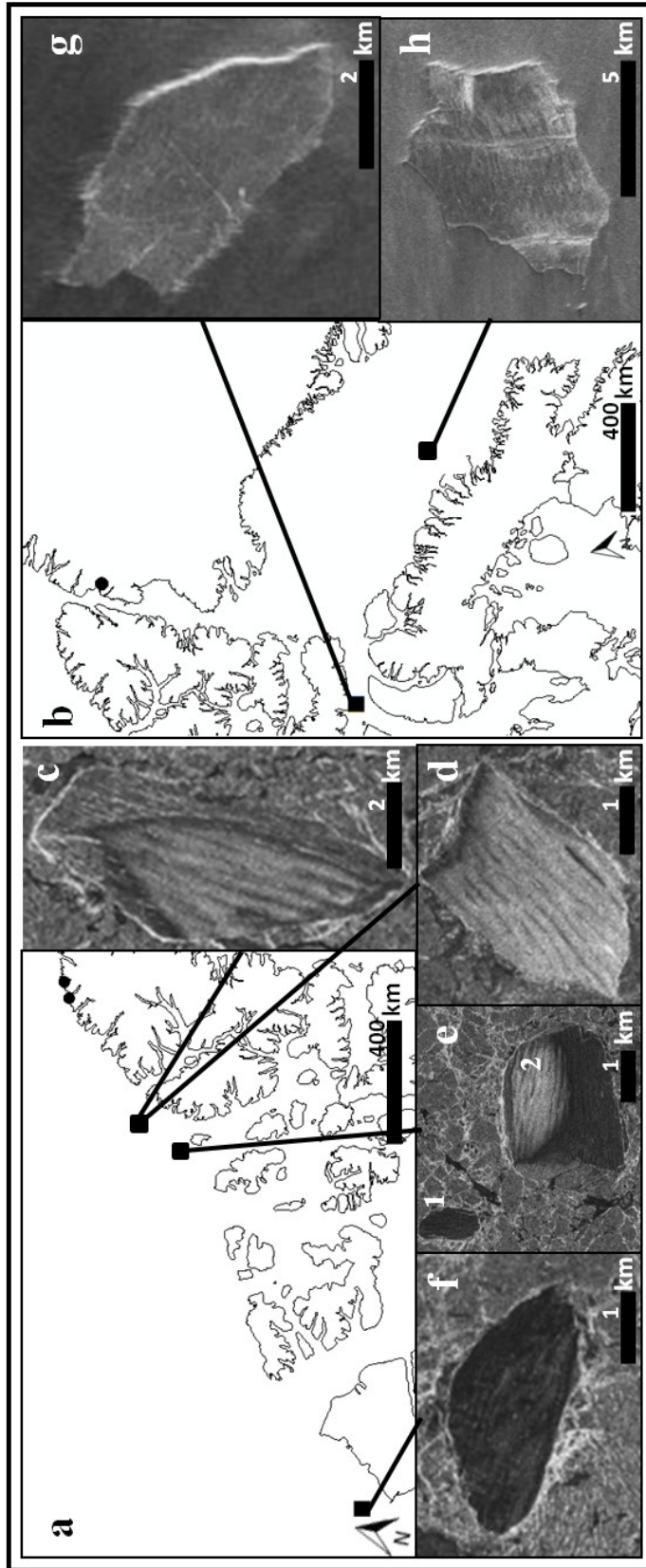
Figure 3.5: Study sites in the Western (a) and Eastern (b) Canadian Arctic. ● (a) Ward Hunt and Markham ice shelves, ● (b) Petermann Glacier. (c) WH1: 2009-10-08, (d) WH2: 2009-09-27, (e) M1 and M2: 2009-10-16, (f) M3: 2009-10-22, (g) PII-B-a: 2011-10-06, (h) PII-B: 2011-10-23. All images are Radarsat-2 © MDA.
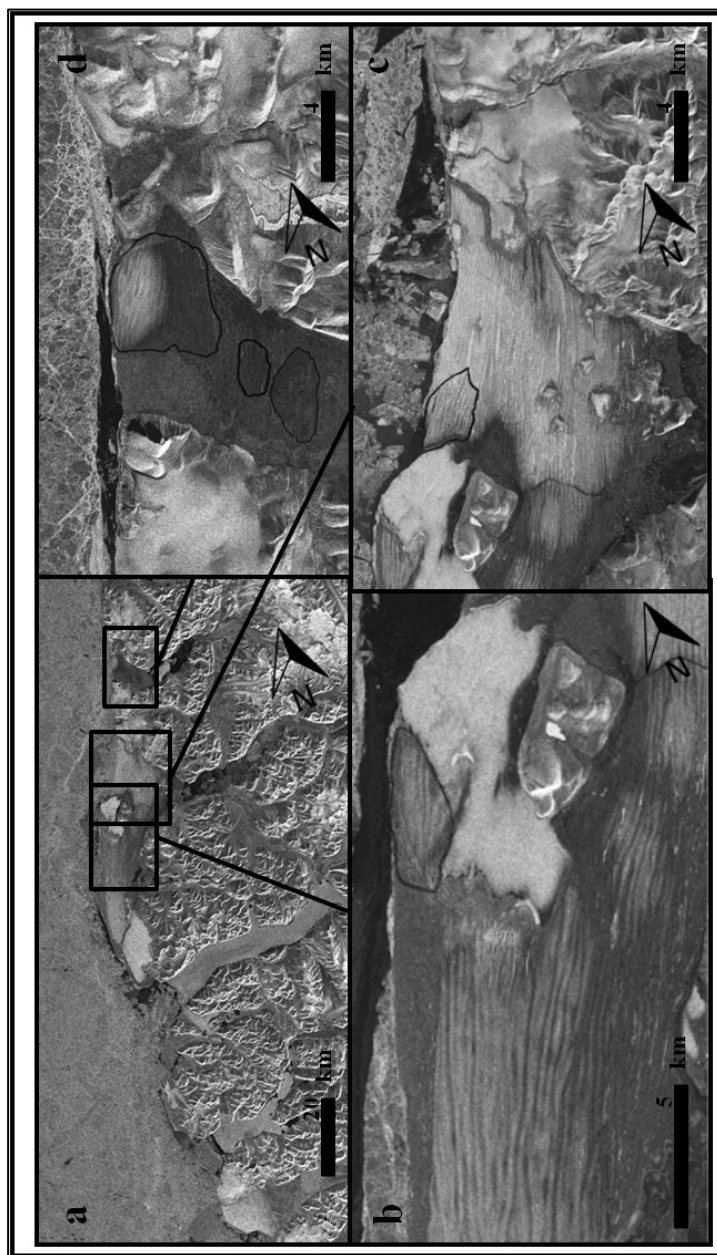
Figure 3.6: Original ice island placement within northern Ellesmere Island ice shelves a) Overview (2007-09-07), before break-up events of 2008. (b) Ward Hunt Ice Island 1 – Southwest Ward Hunt Ice Shelf (2007-01-24). (c) Ward Hunt Ice Island 2 – Northeast Ward Hunt Ice Shelf (2008-02-02). (d) Markham Ice Island 1 – Markham Ice Shelf (2007-01-21). All images are Radarsat-2 © MDA.

3.3 Methods

3.3.1 *Ice island tracking*

Nine global positioning system (GPS) tracking beacons were deployed on six ice islands in the Canadian Arctic for location monitoring and assisting in RADARSAT-2 image acquisitions. Displaced distance was measured from first and last beacon transmission location, unless otherwise noted (Table 3.3).

3.3.2 *Ice thickness measurements*

A 10 MHz ground penetrating radar (GPR) recorded point ice thickness measurements at sample sites established on the 2010 PII fragments PII-B and PII-B-a during field work in October 2011. Sample sites on PII-B-a were chosen down the center line of the ice island and were as evenly distributed as possible. PII-B's sample sites were selected on either side of a pre-existing surface erosion trough (Fig. 3.3).

The GPR's transmitter and receiver, with corresponding antennas laid in parallel, were separated by 10 m, with the mid-point located at the site of an surface ablation stake installation (Halliday et al., 2012). A sampling window of 500 ns (approximately 420 m) was used to ensure that the total thickness of the thick Petermann ice islands would be captured. Eight traces were stacked to attenuate random noise by averaging multiple radar shots (Labey et al., 2009) and high frequency noise was removed with a 15 MHz low-pass filter (Halliday et al., 2012).

GPR post-processing was conducted manually with the identification of the surface wave (the the time associated with the surface wave's first peak) and ice-water interface (the timing of bed wave's first trough) to yield the two-way travel time (Fig. 3.7) (Halliday et al., 2012). This reflection is created by the dielectric differences (κ) of ice ($\kappa=80$) and water ($\kappa=3$), which allows for the identification of the ice bottom (Mortimer, 2011; Irvine-Fynn et al., 2006). Wave velocity

and permittivity, in ice is influenced by density, ice structure and electrical conductivity (Arcone, 2009). For the calculation of ice thickness, a standard electromagnetic wave velocity of 0.168 m ns[-1] was used for the 'temperate' condition of the ECA ice islands (Bogorodsky, 1985; Bradford et al., 2009; Halliday et al., 2012). A common midpoint survey, utilized to calibrate wave velocity, was not conducted due to limited time on site; however, error due to the choice in wave velocity value is likely to be small and was not considered further in this analysis. Total ice thickness (T) was calculated by the conversion of two-way travel time (t) (ns) (Eq. 3.1).

$$T = \sqrt{\left[\left(\dfrac{t + \frac{s}{0.3}}{2}\right)v\right]^2 - \left(\dfrac{s}{2}\right)^2} \tag{3.1}$$

where s is the antenna separation (m) and v is the electromagnetric wave velocity for ice (m ns[-1]).
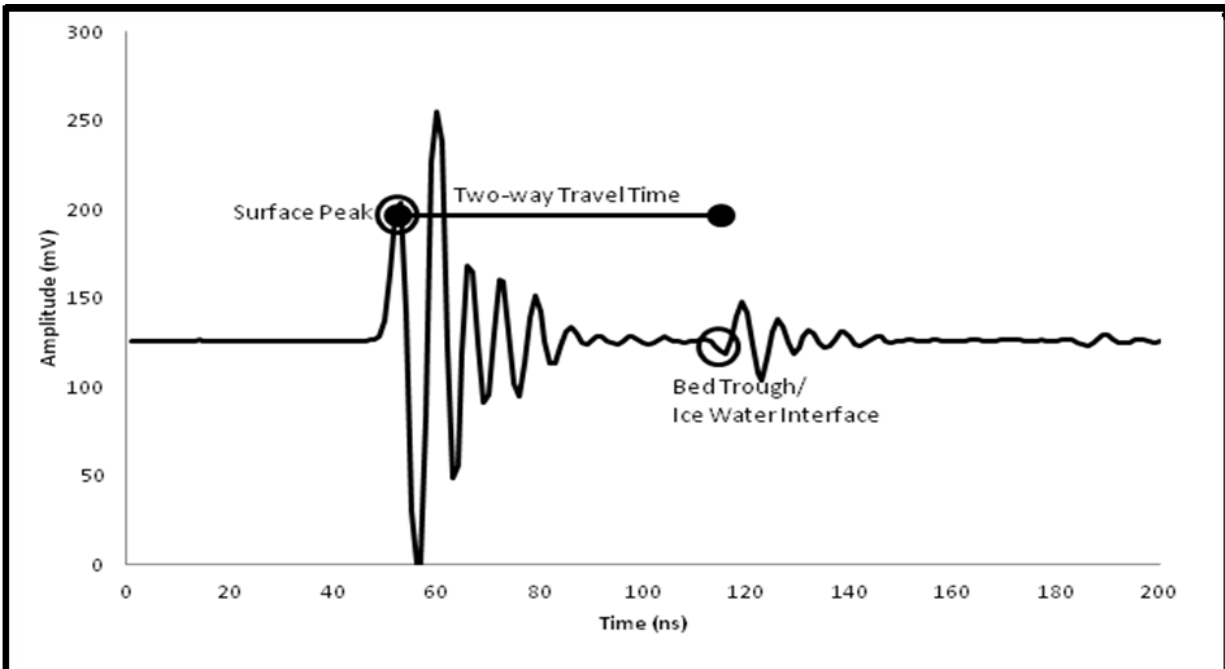
Figure 3.7: GPR trace showing the 'picking' of the surface peak and bed trough (location of ice-water interface). The distance between the two is the two-way travel time, used to calculate ice thickness (Eq. 3.1) (After Pope, 2010).

GPR resolution, or the minimum separation length required to be able to distinguish between two objects in range direction, is typically calculated as λ/4, where λ is the GPR's center frequency (Woodward and Burke 2007). Since in this study, the range from the surface to a distinct interface between media with very different κ values is more important, error in thickness measurements was calculated from the waveform sampling interval. The GPR system sampled at 10 ns intervals which equates to an uncertainty in surface or reflected wave position of ±0.4 m. Total thickness error is obtained by propagating these errors in quadrature (Taylor, 1982) and is equal to ±0.6 m. Errors associated with average ice island thickness are reported in Table 3.2.

3.3.3 *Ice island surface area*

Ice islands can be distinguished in satellite imagery from pack ice or open water by their extensive size, angular shape and relatively high backscatter. Differences in backscatter occur due to: 1) freshwater content of ice islands, 2) strong return along ice island edges, and 3) in the case of WCA and with an appropriate look direction, the ridge and trough surface structure (Jeffries and Sackinger, 1990). Synthetic aperture radar (SAR) satellite imagery (RADARSAT-2) was acquired between September 2009 and March 2010 for the target ice islands of the Western Canadian Arctic originating from Ellesmere Island (De Abreu et al., 2011). RADARSAT-2 images of the PII fragments (ECA) were acquired between September 2011 and March 2013. Appendix A provides details on the acquired RADARSAT-2 imagery. All RADARSAT-2 imagery uses a frequency of 5.405 GHz (5.55 cm wavelength, operating in the C-band) (van der Sanden and Drouin, 2011). An attempt to acquire images in FQ or Ultra-fine (UF) beam modes and HH polarization was made to allow for best image detail and consistency in surface area measurement. ScanSAR products (narrow and wide), which are routinely used by

the CIS for sea ice charting and tracking of both ECA and WCA ice islands, were also acquired and were utilized for surface area analysis. Due to the low resolution of ScanSAR imagery, there is a greater uncertainty in the ice island surface area. However, the benefit of increasing the temporal resolution of the study outweighs the increased error associated with these images.

RADARSAT-2 data was converted to amplitude images, projected with bilinear re-sampling, stretched to enhance contrast and analyzed in ArcGIS 10.0 (ESRI, Redlands, CA). Ice islands were vectorized to a polygon by hand to compute surface area. WCA ice island images were projected in an Albers Equal Area projection while those of the ECA were projected in a Lambert Conformal Conic projection (both WGS 1984). Prior projects used these specific projections and are the reason for their use in this study. Any potential difference in surface area due to the projection was ignored due to the small spatial scale of the ice islands.

Uncertainty (error) in ice island polygons is based upon image resolution and manual digitization. The possibility of human error is inherent in the delineation of polygon vertices when digitizing the ice island images but assumed small enough to not warrant inclusion in the overall error calculation (Hoffman et al., 2007). RADARSAT-2 ScanSAR Wide, ScanSAR Narrow, Wide, FQ, and UF beam modes have resolutions of 160, 80, 13.5, 7.6 and 3 m, respectively (MDA, 2009). Surface area measurement error was calculated by the 'equivalent-area square' method developed by Ghilani (2000) and used by other glaciologists (Hoffman et al., 2007) (Eq. 3.2).

$$\sigma_{area} = D\sigma_D\sqrt{2} \tag{3.2}$$

where D is the side length of square equal in area to ice island and σ_D is the uncertainty in D (½ image resolution due to confidence within ± ½ pixel during image digitization).

An experiment was undertaken to examine the resolution effects on areal uncertainty between FQ and ScanSAR Wide-beam modes and the accuracy of the 'equivalent-area square' method of areal

uncertainty computation. The surface area of an ice island was digitized on five separate occasions from one FQ and one ScanSAR Wide acquisition. The standard error of the vectorized surface areas were 0.023 km^2 (0.37%) and 0.098 km^2 (1.5%) for the FQ and ScanSAR Wide products, respectively. For a hypothetical 10 km^2 ice island the error associated with a FQ acquisition would be ± 0.0014 km^2 (± 0.014%) and increase to ± 0.36 km^2 (3.6%) for a ScanSAR Wide product. The 'equivalent-area square' method for areal uncertainty calculation thus understates error associated with FQ acquisitions and overstates for ScanSAR Wide products. It was concluded that the 'equivalent-area square' method of areal uncertainty calculation was acceptable for this study.

3.3.4 *Volume and mass calculations*

An average of the thickness measurements (Table 3.2) was used in the estimation of ice island volume and mass. It was only possible to take thickness measurements once on each ice island, as planned return visits to the ice islands in the summers of 2012 and 2013 were cancelled or curtailed by weather and logistical considerations. The change in thickness was estimated using literature values in the absence of data from PII-B-a and PII-B. Thickness change was recorded between two field visits to another fragment of the 2010 PII, PII-A, in 2011 (Halliday et al., 2012). The average surface (5.0 cm d^{-1}) and basal (2.4 cm^{-1}) ablation rates of PII-A were thus used to estimate thickness decrease of PII-B-a and PII-B (Halliday et al., 2012). The surface ablation rate was only applied when monthly air temperatures from NCEP/NCAR reanalysis (Kalnay et al., 1996) were above 0°C. This was the same procedure for basal ablation rate and SST, also from NCEP/NCAR reanalysis. Otherwise thickness was assumed to remain constant throughout the deterioration analysis. Volume was estimated by simply multiplying thickness by surface area. Any deviation from a vertical sidewall was assumed to be unimportant relative to other errors. Mass was calculated by multiplying an ice island's volume (km^3) by a water

equivalent of 0.9 tonnes m^{-3} (Peterson et al., 2009) (Table 3.2; Fig. 3.9). No thickness data was recorded from these ice islands, therefore making it impossible to estimate volume and mass loss during deterioration.

3.3.5 *Sea Ice Concentration Analysis*

Weekly regional sea ice charts, composed of polygons corresponding to sea ice concentration and type, were downloaded from the CIS ice archives. Sea ice concentration represents the ratio between open and ice covered waters (MANICE, 2005). These charts were clipped by tracking beacon coordinates to include the sea ice polygons which interacted with the corresponding ice island (Environment Canada, 2012). These coordinate points were picked by drawing a box around the entire beacon track in GIS. The coordinates of the box corners were inserted into a Python (version 2.7.2) script that digested the sea ice chart data. The total sea ice concentration, in tenths (MANICE, 2005), was determined for the area surrounding the ice island. This corresponds to several categories: open or bergy water (< 1/10), very open drift (1/10 to 3/10), open drift (4/10 to 6/10), close pack (7/10 to 8/10), very close pack (9/10 to < 10/10) and compact or consolidated ice (10/10) (MANICE, 2005). In cases where the ice island was intersected with two or more sea ice polygons, the sea ice concentration value was calculated as a weighted average of the ratio of the ice island's perimeter in contact with each sea ice polygon.

3.3.6 *Deterioration Modes*

The surface area loss rate (km^2 d^{-1}) was used to classify and describe the deterioration patterns of Arctic ice islands. Large fracturing events were categorized by a surface area rate loss ≥ 0.2 km^2 d^{-1}. Fragmentation was categorized by a surface area deterioration rate between 0.1

km^2 d^{-1} and 0.2 km^2 d^{-1}. Decay was characterized by a loss of < 0.1 km^2 d^{-1} of the ice island's surface area. In this paper, decay is used to describe small-scale deterioration events during the summer (melt season) as well as during the winter (ice-covered season) when the ice islands deteriorate at much slower rates. It is very likely that fragmentation and decay are occurring at the same time during the warmer summer months and thereby producing a large size range of calved pieces. The loss of the larger pieces over-shadows those lost by smaller-scale decay. Decay therefore becomes the dominant mode of deterioration during the winter months when no fragmentation occurs. When surface area increased between images it was classified as addition. This was likely associated with the freeze-on of sea ice but could have also been recorded during digitization of decreased resolution of operational ScanSAR RADARSAT-2 imagery or due to the human error inherent with manual vectorizing ice island polygons in GIS.

3.3.7 *Environmental conditions and deterioration rate analysis*

Environmental variables were measured or calculated for each ice island to investigate the important factors controlling ice island deterioration rates. Temperature data was recorded by GPS tracking beacons on most of the monitored ice islands. Recorded air temperature (T_a) may not be reflect true atmospheric T_a due to the sensor's enclosure within the beacon housing which may be installed below the ice surface or in direct sunlight. NCEP/NCAR T_a reanalysis of the region surrounding the drift track of PII-B-a and the first month of PII-B image acquisition filled-in data gaps in the beacon T_a data. Temperatures were averaged daily and melting degree days (MDD; the sum of daily average temperatures above zero) and days above zero (DAZ) were calculated for each ice island. Monthly regional SST was determined with NCEP/NCAR reanalysis. Sea ice concentration was determined as described in Section 3.4.5.

Correlation analysis using Spearman's rank coefficient was carried out for all variable combinations since variables were not normally distributed. Data from the environmental variables and rates of surface area decrease were averaged for each ice island and correlation analysis was carried out on the means to account for temporal pseudoreplication. Temporal pseudoreplication was inherent in this study due to the repeated measures made on the individual ice islands tracked in the two regions. The small sample size ($n = 7$) made it difficult to detect relationships between averaged environmental data and deterioration rate. A correlation matrix was also created without pseudoreplication removal. It is recognized that results from the un-averaged analysis cannot be extrapolated to other regions; however, its use in depicting associations in the Canadian Arctic is informative in this study.

A linear mixed effect (LME) model was created with non-averaged environmental and surface area data. This modeling method includes both fixed and random effects which affect a response variable (Crawley, 2007). Fixed effects are statistically associated with the response variable (deterioration rate calculated as surface area loss rate) and will affect its mean, while random effects affect its variance (between Canadian Arctic regions) (Crawley, 2007). The ice island is the random effect term in the model as each ice island is repeatedly measured throughout the study. LME regression models were created to find the environmental variables (fixed effects) that were the most influential in controlling deterioration rate.

A benefit of this modeling method is the retention of a high number of degrees of freedom (n = 70: ice island observations, df = 69) versus the degrees of freedom when comparing the means of ice island characteristics and observations (n = 7: independent ice islands, df = 6). The deterioration rates of ice islands between the ECA and WCA were compared with this method to determine if there was a regional difference in deterioration rate. Associations between environmental variables and deterioration rates were also explored. The

47

best LME model to explain deterioration was chosen based on p-values and model fit measures (Akaike's Information Criterion, AIC and Bayesian Information Criterion, BIC), which take into consideration model strength as well as model parsimony (Crawley, 2007).

3.4 Results

3.4.1 Eastern Canadian Arctic

Drift

PII-B-a was located within Lancaster Sound and adjacent channels from 13 October 2011 to 7 October 2012. After this point, PII-B-a ceased looping within Lancaster Sound and began drifting south in Baffin Bay. It was grounded for a period (71°19'N, 71°05'W) between 4 November 2012 and 19 March 2013. PII-B-a displaced a distance of 800 km, from Lancaster Sound to Baffin Bay over 720 days (Fig. 3.8) (Table 3.3).

PII-B was grounded at 69°38'N 65°55'W (150 km SE of Clyde River, NU) from 22 October 2011 to 12 August 2012 and then traveled 140 km SSE between 13 August 2012 and 2 July 2013. After un-grounding, PII-B drifted at an average speed of 2.5 km d^{-1}, following a south/southeast trajectory in Baffin Bay along the coast of Baffin Island (Fig. 3.8). PII-B had an average drift speed of 5.6 km d^{-1} when in open waters and 0.14 km d^{-1} when surrounded by pack ice.

Thickness

On average, PII-B was thicker than PII-B-a (Table 3.2). However, on both ice islands, there was considerable spatial variability in ice thickness. There was a 35 m difference between the two measurement sites on PII-B with 73 ±0.6 m at Site 1 and 102 ±0.6 m at Site 2. PII-B-a was markedly thinner at one end compared to the other: 50 ±0.6 m (Site 1), 90 ±0.6 m (Site 2) and 96 m ±0.6 m (Site 3), a difference of 46 ±1.2 m over a distance of 3.2 km (Fig. 3.4).

Surface area & mass loss rates, deterioration modes and environmental conditions

Exact deterioration amounts, rates and sea ice conditions are detailed for all ice islands in Appendix B. PII-B-a lost 5.9 ± 0.04 km^2 and $4.1 \cdot 10^8$ tonnes of mass (40%) over the study period from its initial size and mass of 14.2 ± 0.02 km^2 and $1.0 \cdot 10^9$ tonnes (9 September 2011). This ice island only experienced deterioration through fracturing and decay (Fig. 3.9). A single fracturing event in September 2012 accounted for a loss of 10% of the surface area and mass (1.47 km^2 ± 0.04 km^2 and $1.0 \cdot 10^8$ tonnes) and occurred in ice free waters (< 1/10 sea ice concentration). Decay occurred in open water (< 1/10) as well as in very close pack (9/10) and compact ice conditions (10/10) (Fig. 3.9, Appendix B). The surface area and mass of PII-B-a decreased by 4.4 ± 0.2 km^2 and $3.1 \cdot 10^8$ tonnes, respectively, from decay.

At the start of the series of FQ RADARSAT-2 image acquisitions (7 September 2011), PII-B had a surface area of 69.8 ± 0.04 km^2 with an estimated volume of 5.5 km^3 and a mass of $4.8 \cdot 10^9$ tonnes. Over the next 22 months, PII-B lost 58.5 ± 0.06 km^2 of its surface area, amounting to 4.0 billion tonnes of ice drifting independently of the parent ice island. PII-B experienced periods dominated by each of the three deterioration modes. Fragmentation occurred only in open water conditions (< 1/10) (Fig. 3.9) and was only recorded towards the end of the summer melt seasons (September/October 2011 and September 2012) (Appendix B). The seven

fracturing events observed for PII-B occurred during all states of sea ice concentration: open water (< 1/10) in September 2011 and September/October 2012, close pack (8/10) in November 2011 and compact ice conditions (10/10) in January 2012 (Fig. 3.9, 3.5). The largest fracturing event occurred between 16 November and 20 November 2011 when 17.6 km^2 (30% of PII-B's surface area) of ice broke free. This event occurred as new sea ice was forming in the region (very close pack, 9/10) and while PII-B was grounded. The September and October 2012 events occurred during open water conditions after PII-B became ungrounded. In all, fracture events caused a surface area loss of 48.8 ±5.8 km^2 and $2.7 \cdot 10^9$ tonnes of independent fragments. Decay periods were also observed during all sea-ice concentration states and resulted in a loss of 3.96 km^2 (Fig. 3.9, Appendix B).
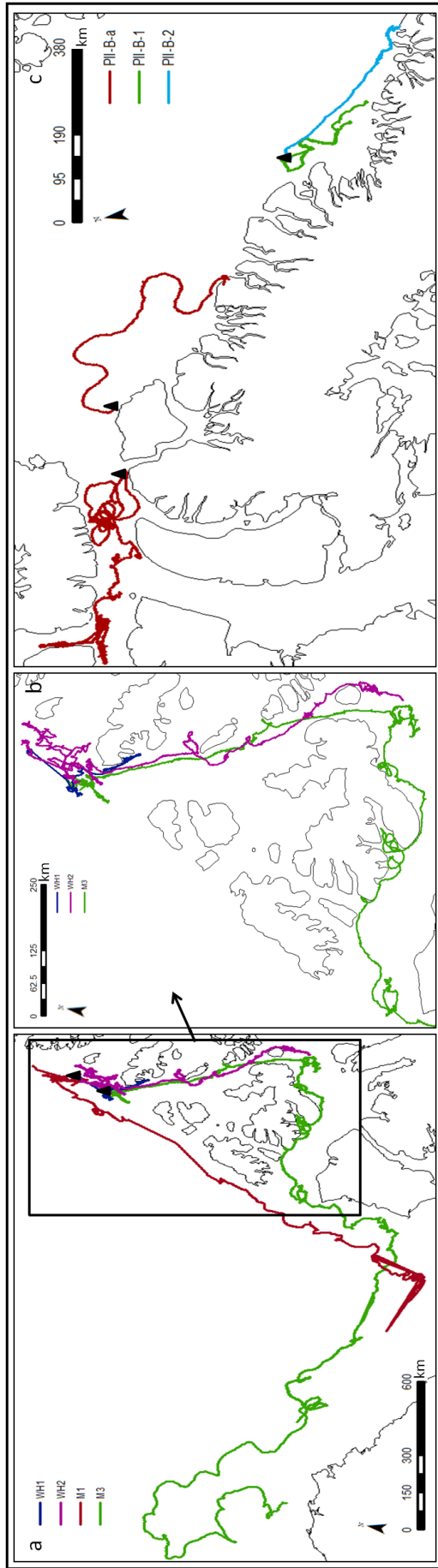
Figure 3.8: Drift tracks of ice islands within the (a, b) Western and (c) Eastern Canadian Arctic. Refer to Figure 3.5 for placement within Canadian Arctic waters and Table 3.3 for beacon specifics. Triangles denote beacon deployment location.
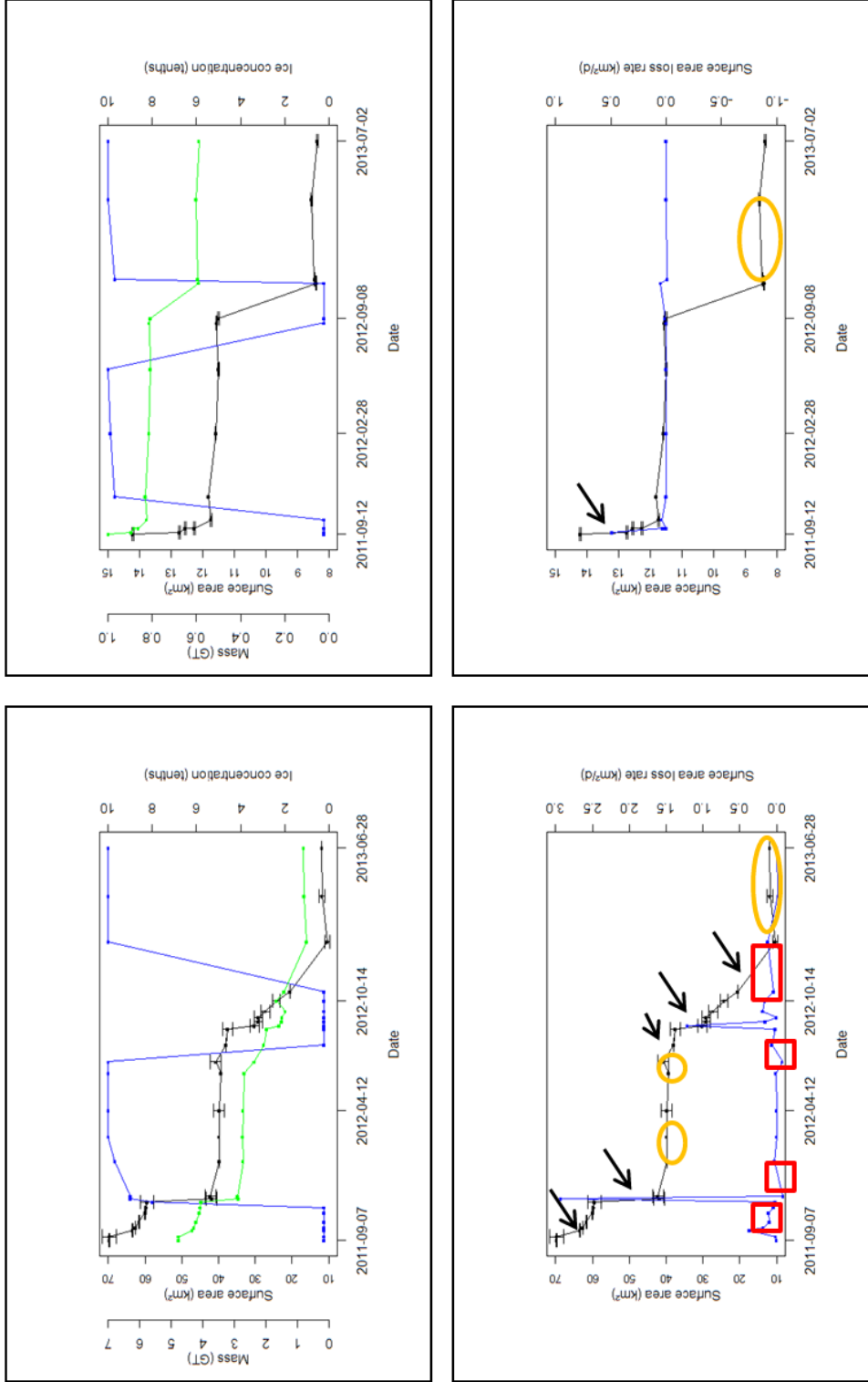
Figure 3.9: Surface area, mass and areal rate loss with sea ice concentration in the ECA. Surface area (black) and mass (green) change and sea ice concentration (blue) for a) PII-B and b) PII-B-a. Surface area loss rate (black) and surface area (blue) for a) PII-B and b) PII-B-a. Surface area loss rate (black) and surface area (blue) for c) PII-B and d) PII-B-a. Fragmentation periods are outlined with red boxes. Arrows point to fracturing events. All other periods with deterioration are classified as decay. Periods of addition are circled in orange.

3.4.2 Western Canadian Arctic

Drift

Table 3.3 reports the displaced distances and duration of tracking for the five WCA ice islands, while Figure 3.8 illustrates their respective tracks. Of the five ice islands located in the WCA, only M3 was being tracked when it fully deteriorated on 10 November 2012. The ice island had been adrift for over 4 years and 4 months and had displaced a distance of 2100 km over the 936 days it was tracked (2 km d^{-1}). WH1 and WH2 drifted south through the western channels of the CAA at a speed of 0.6 and 0.9 km d^{-1}, respectively. M1 and M2 (observed in imagery with M1) drifted along the western edge of the CAA and circulated westward in a trajectory consistent with drift in the Beaufort Gyre. M1 drifted 2200 km (an average of 2 km d^{-1}).

Surface area decrease, deterioration modes and sea ice concentrations

WH1 had a surface area of 11 ± 0.03 km^2 (6.2 x 2.7 km) when first imaged by ScanSAR Wide in May 2009 as well as when FQ RADARSAT-2 image acquisition began in September 2009. Between 7 May 2009 to 1 December 200 and between 8 January 2010 to 29 March 2010 the ice island experienced deterioration by decay only and lost a total area of 2.45 ± 0.43 km^2. The only recorded fracturing event was in December 2010 and resulted in the loss of 35% of the ice island's areal extent. This occurred during very close pack (9/10 to <10/10) sea ice concentrations that were typical for this ice island throughout the duration of the study period (11 months) (Fig. 3.10, Appendix B).

WH2 was within very close pack from 7 May 2009 to 26 March 2011 except for one 45 day period of open drift conditions (4/10 to 6/10). The ice island appeared to gain area (0.45 ± 0.53 km^2) over that time (Fig. 3.10) due to accumulated sea ice made apparent in image

digitization (Appendix B). WH2 deteriorated through be decay for most of the monitoring period except for two observed fracture events.

When FQ image acquisition began in September 2009, M1 had a surface area of 18 km^2 (5.8 x 4.0 km) and was composed of both meteoric and marine ice. M2 was only composed of marine ice and was 2 km^2 (2.6 x 1.0 km) (De Abreu et al., 2011). M1 and M2 were surrounded by high sea ice concentrations (very close pack, 9/10 to <10/10) for the duration of the study period (7 May 2009 to 19 February 2010 and 7 May 2009 to 2 March 2010, respectively). M1 deteriorated through decay (5%) and one fracturing event where its areal extent decreased by 22% (Fig. 3.10, Appendix B). M2 deteriorated through decay for the majority of the study period. It decreased by 0.74 ±0.03 km^2 (35% of the starting 2.13 km^2 ±0.01 km^2 surface area), with 17% of the original surface area lost due to decay (Fig. 3.10, Appendix B).

M3 had a surface area of 4.6 ±0.11 km^2 when first imaged with RADARSAT FQ in October 2009. FQ image acquisition continued sporadically through May 2011 (12 images). The ice island only lost area in the decay mode totally 0.7 ±0.02 km^2 in area (Fig. 3.10, Appendix B).
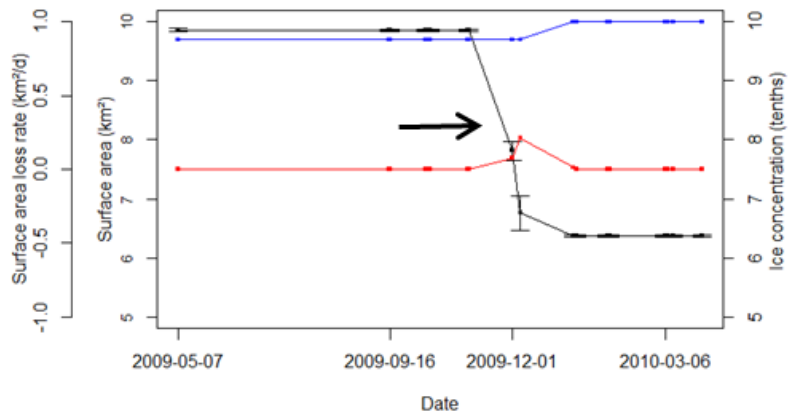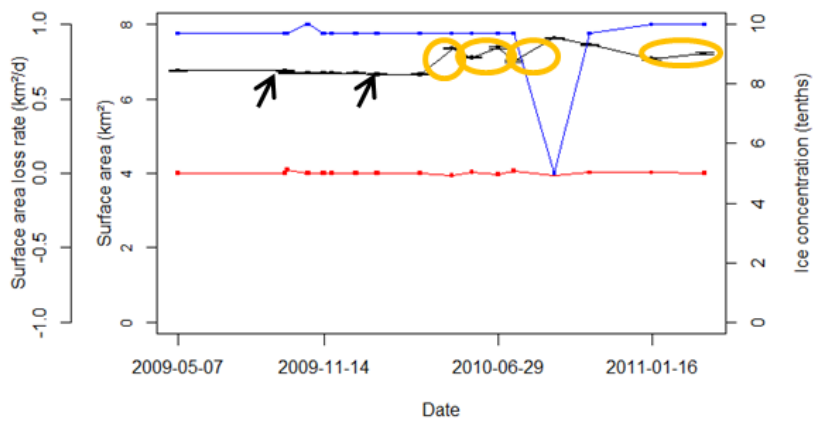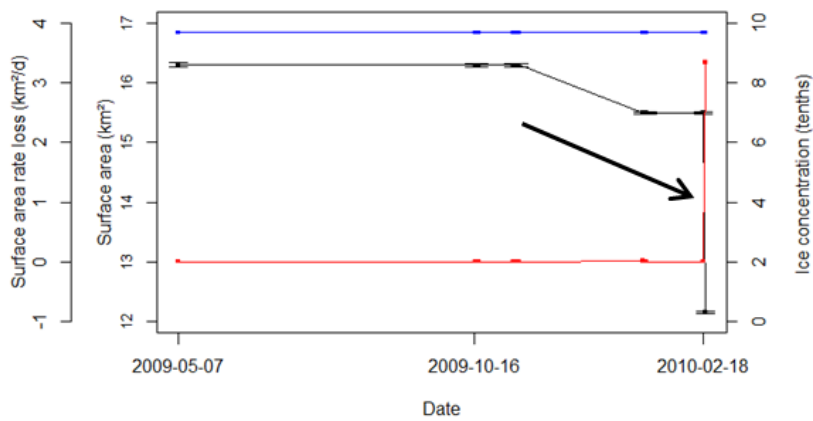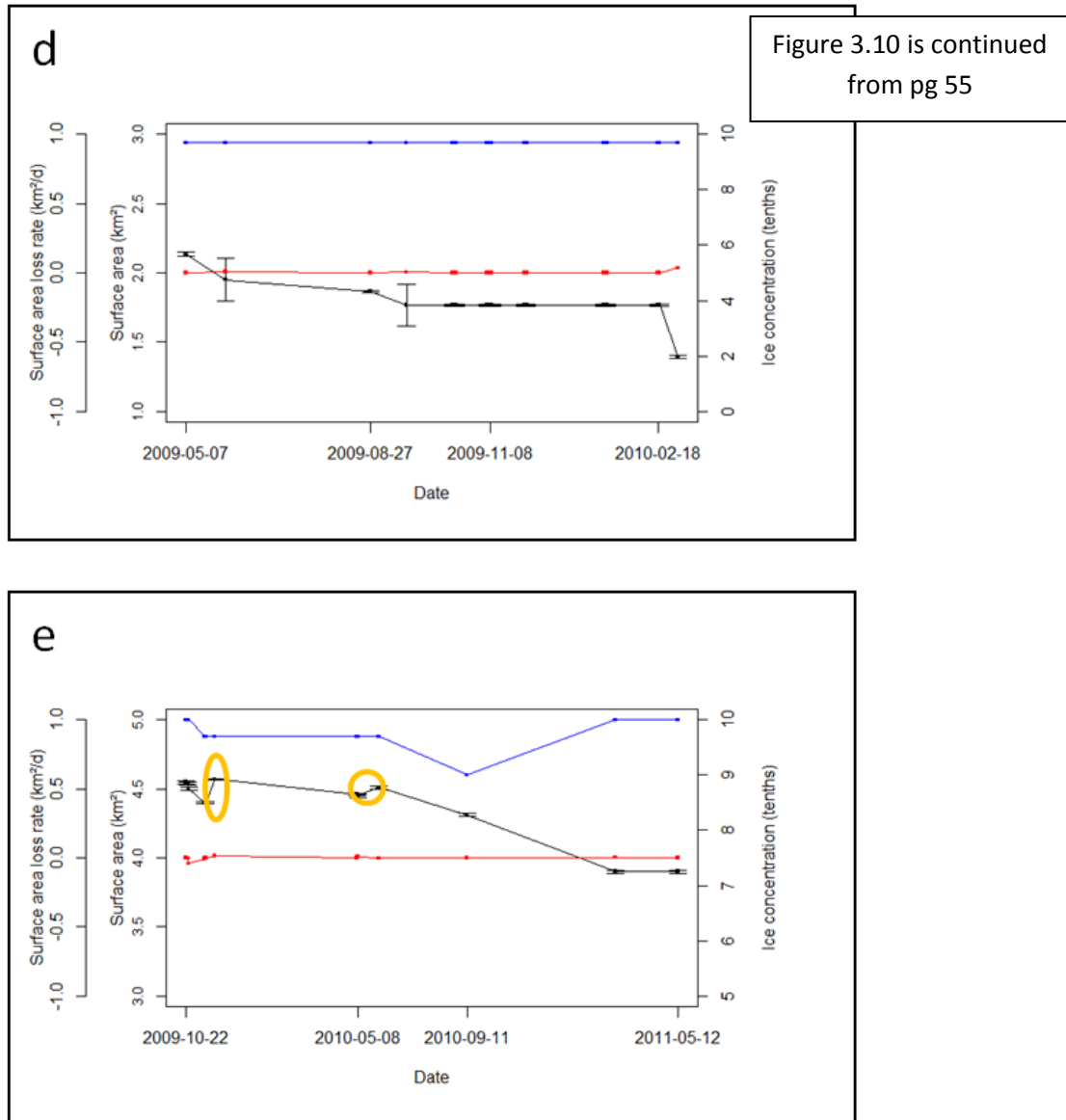
Figure 3.10: Surface area loss (black), sea ice concentration (blue) and rate of areal loss (red) of a) WH-1, b) WH-2, c) M-1, d) M-2 and e) M-3. Arrows point to fracture events. Periods of addition are circled in orange.

3.4.3 Eastern and Western Canadian Arctic

Environmental conditions and deterioration rate

Spearman's rank correlation analysis after variable data was averaged for each ice island showed that no environmental variables were significantly correlated with deterioration rate ($km^2\,d^{-1}$). This is possibly due to the low sample size created by averaging the information of each ice island. Without data averaging, T_a, SST and sea ice concentration are all significantly correlated ($p<0.05$) with deterioration rate ($km^2\,d^{-1}$). MDD (for the period in between observations), cumulative MDD and DAZ were not significantly correlated with deterioration rate (Table 3.4).

The LME model developed to predict deterioration rate with no fixed effects (environmental variables) but which did include the random effects of ice island and origin showed that there was a marginally significant ($p<0.10$) difference between the deterioration rate ($km^2\,d^{-1}$) of ice islands with differing regions of origin (ECA vs. WCA). The deterioration rate of each ice island is grouped individually and by origin and illustrated in Figure 3.11. The LME regression model which included T_a and sea ice concentration (as individual, fixed-effect terms) was the best fit (AIC=136, BIC=150) for modeling ice island deterioration rate. The fixed effect of T_a was marginally significant ($p<0.10$); however, sea ice concentration was not ($p=0.11$). It was decided to retain the sea ice concentration term as T_a was not significant after its removal. The interaction term between T_a and sea ice concentration was also significantly correlated ($p<0.05$) with deterioration rate in correlation analysis.
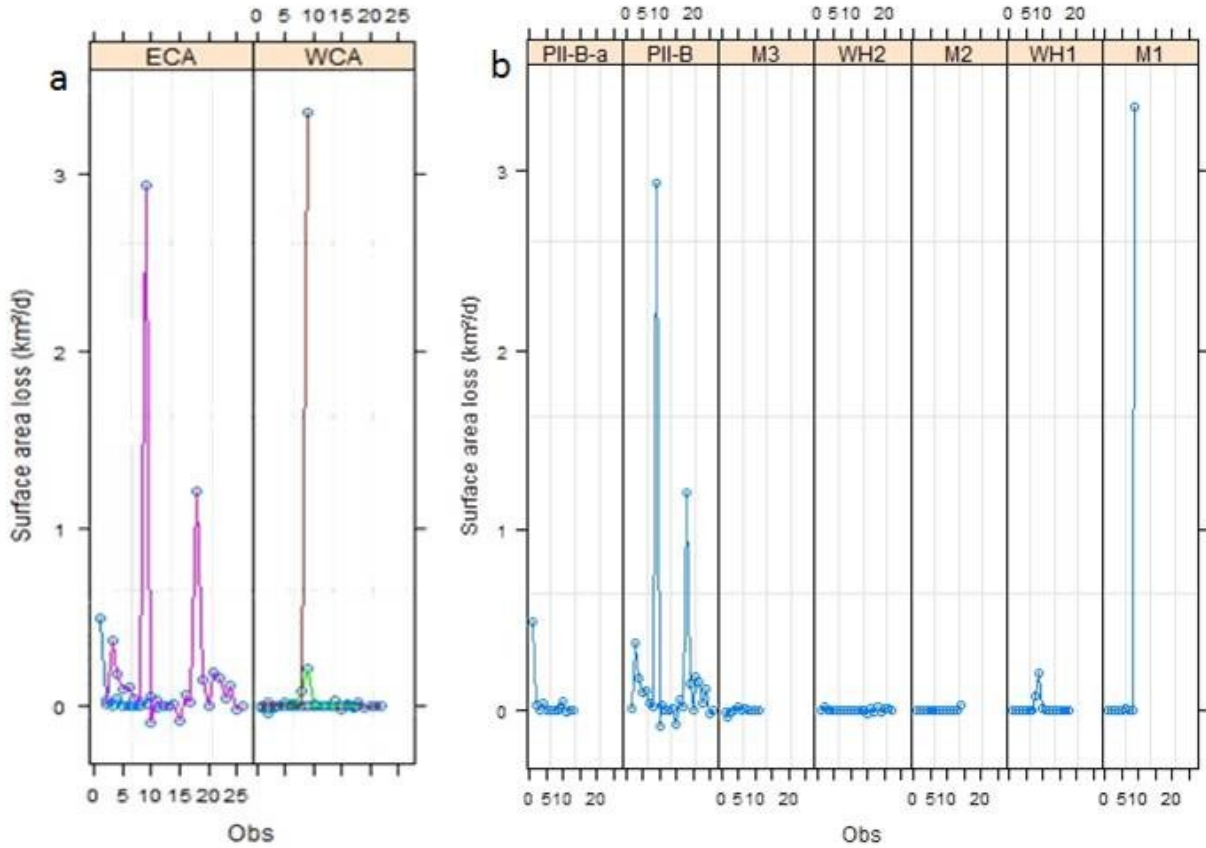
Figure 3.11: Surface areal rate loss (km^2 d^{-1}) between a) regions and b) individual ice islands. Obs (x-axis) represents consecutive RADARSAT-2 acquisitions. Different colours in a) represent ice islands located within that region: ECA: PII-B (pink), PII-B-a (blue) and WCA: M3 (blue), WH2 (pink), M2 (orange), WH1 (green), M1 (red).

Sea ice concentration and T_a were significantly different between the ECA and WCA when tested in the same manner as deterioration rate with LME modeling (T_a or sea ice concentration modeled with the random ice island effect). Given that T_a is included in the parsimonious and robust LME model and the significant difference of T_a between the ECA and WCA, it is suggested that it is the most important factor in controlling ice island deterioration rate. T_a is followed by the sea ice concentration effect in terms of importance, which is also included in the LME model and is significantly different between the two regions of origin. Both

are also significantly correlated with deterioration rate, as is their interaction term ($p<0.05$), albeit without the removal of possible pseudoreplication error through data averaging.

3.5 Discussion

3.5.1 *Influence of sea ice concentration on ice island deterioration mode*

Four mechanisms have been identified which contribute to the side wall deterioration of ice islands: buoyant vertical convection, forced convection from wind and water currents, wave erosion and calving of overhanging slab resulting from wave erosion (Fig. 2.5) (Ballicater, 2012; Kubat et al., 2007; Savage, 2001). The latter two are deemed to cause the greatest relative loss during iceberg deterioration, accounting for a combined volume loss of 68 to 87% (Savage, 2001).

There is an exponential decrease in wave period and amplitude with the distance a wave travels under a continuous ice sheet, therefore high sea ice concentration results in the attenuation of wave energy (Squire et al., 1995). Consequently, the amount of erosion caused by waves should decrease when sea ice surrounds the perimeter of an ice island due to this attenuation of wave energy and the physical barrier that the sea ice provides to an ice island's side walls. This effectively stops sidewall deterioration through the wave erosion process and therefore the calving of overhanging slabs formed from wave erosion stops as well.

In this study, sea ice concentration correlated with deterioration rates and was included in the final LME model. Fragmentation did not occur when the ice islands of this study were within heavy sea ice conditions. In particular, the WCA ice islands in this study were never in open water conditions, as classified by CIS ice concentration charts and were never observed to be subject to the fragmentation deterioration mode. The ice islands of the ECA were within open water conditions for up to 27% of the time monitored and each (PII-B and PII-B-a) spent periods

deteriorating by the fragmentation process. This is in agreement with the observation by Scambos et al. (2005) that the edge-wasting deterioration process (equivalent to this Arctic ice island's fragmentation) became more influential after tabular icebergs drifted free of sea ice.

In contrast, large fracturing events were recorded in both the ECA and WCA. These events occurred during periods of <1/10 sea ice concentration (PII-B, October 2012 and PII-B-a, September 2011), while ice was just beginning to form (9/10, PII-B, November 2011) and when full sea ice cover was present (10/10, WH1, November/December 2009). However, out of the five WCA ice islands, only WH1 and WH2 experienced deterioration by fracturing. The observation of fracturing events in various ice conditions was also observed by Scambos et al. (2005) for Antarctic tabular icebergs.

The presence of sea ice does not imply mean that large fracturing events cannot occur to ice islands. However, its presence does inhibit the ability for the multiple pieces to drift independently of each other. It may therefore be impossible to detect that a fracture has occurred until pressure from surrounding sea ice lessens and the two remaining pieces are able to drift far enough to be detected by RADARSAT-2 imagery (8 m resolution for FQ, 160 m for ScanSAR).

Scambos et al. (2005) and Ballicater (2012) note that large fracturing events often or may occur along pre-existing flaws. Ballicater (2012), Scambos et al. (2005), MacAyeal et al. (2006) and Wadhams (1986) state that stress exerted by ocean-swell and wave amplitude contribute to ice island fracturing. Surface troughs that are found on some ice islands are potential fracture locations since melt water collects there and re-freezes, releasing latent heat (Jeffries, 1987). However, the location and timing of fracturing events are very difficult to predict since it is impossible to quantify all internal and surface flaws (e.g., cracks, crevasses, troughs) (Ballicater, 2012; Goodman et al., 1980).

When sea ice was present ice islands were predominately subject to the decay deterioration mode. PII-B-a and PII-B each experienced decay while surrounded by sea ice and in open water, with a combined decrease of 8.3 km^2 or $1.1 \cdot 10^9$ tonnes of ice. The WCA ice islands all experienced loss due to decay as well with a combined decrease of 4.0 km^2. Scambos et al. (2005) found that this mode (classified as disintegration in the Antarctic iceberg study) occurred when a tabular iceberg was flooded with surface melt ponds. Both PII-B-a and PII-B did experience these conditions during the summer season and large melt ponds were observed on PII-B-1 during August 2012 field work (Fig. 3.12).

The coarse temporal resolution of RADARSAT-2 FQ and spatial resolution of ScanSAR image acquisition does not always allow periods of fragmentation and decay to be distinguished. It is probable that both are occurring in tandem for the ECA ice islands during the summer melt season. By using the 8 m resolution of FQ imagery, which is better than ScanSAR wide beam (160 m) used by CIS operations and MODIS imagery (250 m) used for previous work on Antarctic tabular iceberg deterioration (Scambos et al., 2005), three deterioration modes (fracture, fragmentation and decay) could be identified in this study. Error in surface area digitization increased with the decreased resolution of FQ, ScanSAR wide and MODIS imagery (±0.14%, 3.6%, 5.6%, respectively), using Ghilani's (2000) method for calculating remote-sensing areal uncertainty). Given a hypothetical ice island area of 10 km^2 and a thickness of 100 m, this error relates to ±122 tonnes (FQ), ±300,000 tonnes (ScanSAR wide) and ±500,000 tonnes (MODIS).

3.5.2 *Mass loss and hazard potential*

The fragments created throughout the deterioration of an ice island become independent ice hazards. According to the results of this study, $4.8 \cdot 10^9$ tonnes of independent ice hazards were potentially created from two ice islands over 20 months in the ECA. Fragments created by fragmentation or large fracturing events are more likely to be identifiable in satellite imagery than growlers or bergy-bits which are discharged through small-scale decay. The CIS defines a growler as a piece of ice with < 1 m freeboard, < 5 m length, a surface area of 20 m^2 and mass of 1,000 tons, approximately (MANICE, 2005). A bergy bit is larger with a freeboard between 1 and 5 m, length between 5 m and 15 m, a surface area between 100 and 300 m^2 and an estimated mass of 10,000 tons (MANICE, 2005). Daughter ice islands created during fracturing events were responsible for the most substantial surface area and mass losses. The ability to identify these large fragments/smaller ice islands on satellite imagery allows offshore management to be alerted of their locations. The small fragments (bergy bits and growlers) discharged during decay are still of impressive mass (> $3.0 \cdot 10^7$ tonnes, ECA) and the inability to locate or track these pieces remotely increases the risk associated with these ice hazards.

Figure 3.12: Ponding of melt water on the surface of PII-B-1, August 2012.

In order to examine the importance of ice islands as a source of smaller ice hazards, a series of first order calculations was undertaken using the result of the deterioration analysis. These calculations approximated the number of either bergy bits or growlers generated by an ice island while in the decay mode. These analysis used the decay rates of PII-B-a and PII-B during this study, the generic mass and surface area of bergy bits and growlers (MANICE, 2005) and the assumption that only one of the two size classes (bergy bits or growlers) would be produced at one time. This is a large approximation of the number of small ice hazards produced, as only two ice islands are used in the calculation and under normal circumstances both bergy bits and growlers will be produced simultaneously. As well, decay sized deterioration occurs throughout

the year but is overshadowed by the larger deterioration modes during the sea ice-free season. However, it is a useful exercise to illustrate the large quantity of small ice hazards produced throughout the deterioration of an ice island. The results estimated that an ice island adrift in the ECA could discharge 430 bergy bits per km of ice island perimeter per month in open water conditions. If all the discharged pieces during the decay period were of growler size, the number of ice hazards would increase by an order of magnitude (approximately 4300 per km of perimeter per month during sea-ice free season in the ECA).

During conditions when sea ice was present, the number of bergy bits or growlers produced, depending on size of discharged pieces, would have decreased to 250 or 2500 per kilometer per month, respectively, in the ECA. This study could not estimate mass loss of the WCA ice islands but it is believed that the discharge rate of bergy bits or growlers would be less than PII-B or PII-B-a, as the WCA ice islands are assumed to be between 30 and 50 m thick and therefore have less volume and mass associated with the length of their perimeter (MANICE, 2005).

It is possible that the mass loss during decay is over-estimated when this process occurs by calving from wave action and notch creation at and above the waterline. This process creates a ram under the waterline (projection of an ice island's submerged wall due to greater melting and/or calving of the un-submerged portion (Fig. 2.5, MANICE, 2005)). The digitization procedure used here has the ability to detect a decrease in surface area above waterline, which has been assumed to be equal above and below the waterline. In reality less ice mass has eroded below the waterline during decay (surface area of the keel is greater than that of the sail). This translates to greater mass loss during fracture or fragmentation when the ram would finally be separated from the parent ice island.

3.5.3 *Drift tracks, environmental conditions and deterioration*

The typical drift trajectories of ECA vs. WCA ice islands cause them to be exposed to contrasting environmental conditions. Ice islands in the ECA tend to drift south more rapidly than their WCA counterparts (Peterson, 2011). At more southern latitudes, ice islands are more likely to encounter ice-free conditions which make it possible for larger deterioration processes, such as fragmentation or fracturing, to occur (Scambos et al., 2008). A sensitivity study completed by Kubat et al. (2007) also found these deterioration rates increase with a corresponding increase in water temperature. This study supports these previous findings by determining that T_a was a factor, along with sea ice concentration, in controlling the rate of ice island deterioration and that it was significantly different between the two regions of ice island origin and drift.

An ice island's drift is impeded when surrounded by sea ice (Scambos et al., 2008). The decreased drift rates of the WCA ice islands when located along the northwest coast of the CAA demonstrates the effect of the presence of sea ice on ice island drift speed. Ice islands in the WCA normally circulate within the Beaufort Gyre (a small number originating from northern Ellesmere Island travel east and south through Nares Strait or through the CAA) (Peterson, 2011; VanWychen and Copland, forthcoming). Ice islands within the Beaufort Gyre have been observed to survive multiple cycles (3-4) around the gyre, each taking 5-10 years (Jeffries, 1992), before deteriorating fully or being picked up by the Transpolar Drift Stream (Jeffries, 1992) and being directed into the North Atlantic. This was not the case for ice islands included in this study but makes it possible for WCA ice islands to survive as ice hazards for a longer duration (up to 40 years; Jeffries, 1992) than those in the ECA. This is possible due to the differences in drift routes, even though WCA ice islands usually start with smaller surface area and lesser thickness. Hobson's Choice Ice Island was reported to have a thickness of 43 m

(Jeffries, 1988), while those of the ECA in this study had thicknesses between 50 and 102 m and have been reported to be as thick as 131 m (Forrest et al., 2012). In the ECA, the time it takes for an ice island to reach these southern latitudes can be slowed by large oscillations, grounding episodes, and local currents (Scambos et al., 2008; Peterson, 2009).

Scambos et al. (2008) point out that the presence of sea ice is not the only condition which causes less fragmentation (termed edge-wasting in the Antarctic iceberg study). The cooler ocean temperatures during the winter season (approximately -2°C along the Canadian Arctic coast, NCEP/NCAR reanalysis) may inhibit this mode as well, while the 0°C summer SST augment deterioration rates. This study did not conclude that SST was important in the LME model, but SST was correlated with deterioration rate when pseudoreplication was not considered.

3.5.4 *Deterioration mode and environmental condition difference between regions*

The deterioration rate ($km^2\ d^{-1}$) and predominate modes were different between the two study regions, as were T_a and sea ice concentration. T_a, sea ice concentration and SST were all significantly correlated with deterioration rate, with T_a and sea ice concentration used as explanatory environmental variables in the final LME model for deterioration rate. The ice islands of the WCA were never subject to open water conditions during the image acquisition period. This likely accounts for the difference in average deterioration rates of WCA ice islands (0.05 $km^2\ d^{-1}$) being less than that of the ECA (0.16 $km^2\ d^{-1}$) as there was a large difference in annual exposure to open water conditions (2.4% vs 27%, respectively).

 The ability to model ice island deterioration rates by T_a and ice concentration is an asset since data for both are readily available from sea ice charts, GPS beacons and/or weather

forecasting. The analysis of the deterioration rate versus environmental variables can be applied to deterioration modes since mode classification was based on deterioration rate.

A limitation to this study was the low number of images acquired during ice-free conditions. More frequent imaging during the summer (open drift conditions) season would augment this dataset and allow for stronger conclusions to be drawn between environmental conditions (air and ocean temperatures) and ice island deterioration rates. *In-situ* SST data would also contribute to a more accurate analysis of this variable's effect on deterioration (versus the utilized regional reanalysis data).

3.5.5 *Ice island life spans*

As of writing, the PII-B-1 (68°28'N, 65°15'W) and PII-B-a-1 (71°19'N, 71°04'W) were both drifting off the coast of Baffin Island, over 3 years after the original 2010 PII calving from the Petermann Glacier. However, another fragment of the original ice island (PII-A) transited the approximately 3000 km from Nares Strait to coast of Southern Labrador in only 321 days. This ice island broke up completely off the Grand Banks, NL in the same 2011 season. Exact dates of the complete break-up are not available for WH1, WH2, M1 or M2. However, M3 was assumed to have fully deteriorated on 10 November 2012, over four years from when the ice island originally calved from the Markham Ice Shelf. This is attributed to decay dominating the deterioration mode (i.e. slow deterioration rates) while trapped in sea ice, which ice islands originating from the Ellesmere Islands are subject to for longer durations annually. This also impedes their drift rates south along the coast or within the CAA. This situation contributes to the slow deterioration of these ice islands as they are not drifting to areas of warmer air and SST conditions or where open drift conditions are realized.

3.6 Conclusion and future work

This analysis demonstrated that there is a difference in ice island deterioration rates and modes between the ECA and WCA, which have been associated here with significantly different T_a and ice conditions between the two regions. T_a and sea ice concentration were the variables used in the LME model to predict deterioration rate and show the differences between WCA and ECA. High sea ice concentrations inhibit large fracturing events (or separation of parent and daughter ice islands) and fragmentation periods. Ice islands of the WCA spend more time in conditions of highly consolidated sea ice and low T_a, which caused WCA ice islands to have low deterioration rates for the majority of this study. The common drift pattern of WCA ice islands may also cause these ice islands to circulate in the Beaufort Gyre and not experience environmental conditions more conducive to increased deterioration rates. This allows for the WCA ice islands to have longer life spans even if they calve with smaller surface area and thinner thickness than their counterparts in the ECA. Future industrial activity in the Beaufort and Chukchi seas must therefore account for the longevity of ice islands produced from the Ellesmere Island ice shelves that may drift into the vicinity of operations.

Ice islands of the ECA experience more fracturing and fragmentation than their WCA counterparts, ostensibly due to less interaction with sea ice and a drift track that transports them to warmer environments. A consequence of this is the production of many independent, large hazards that then need to be tracked along Canada's East Coast. These ice islands have the potential to reach areas of existing activity (Grand Banks, NL) and are also potential risks to vessels and operations looking to increase activity further north along the same coast.

Ice island drift and deterioration data is still needed to augment the sparse ice island observational database, especially during periods of open drift conditions (sea-ice free). This will allow for improved understanding of the influence of environmental conditions (ice

concentration, SST and T_a) on rates and modes of deterioration and the observations needed for risk assessment and management programs of the offshore industry.

Table 3.1: Origin and calving events of ice islands in the Eastern and Western Canadian Arctic under study (adapted from Table 1.1, White (2011)).

Ice island	Region	Origin	Break-off event	Area calved (km^2)	Reference
PII-B	ECA	Petermann Glacier	August 2010	270	Johannessen et al., 2011
PII-B-a	ECA	Petermann Glacier	August 2010	270	Johannessen et al., 2011
M1	WCA	Markham Ice Shelf	August 2008	50	Mueller et al., 2008
M2	WCA	Markham Ice Shelf	August 2008	50	Mueller et al., 2008
M3	WCA	Markham Ice Shelf	August 2008	50	Mueller et al., 2008
WH1	WCA	Ward Hunt Ice Shelf	2010	42	De Abreu et al., 2011
WH2	WCA	Ward Hunt Ice Shelf	2010	42	De Abreu et al., 2011

Table 3.2: Ice island dimensions measured from the first fine-quad RADARSAT-2 images acquired closest to the time of beacon deployment.

Ice island	Date	Length (km)	Width (km)	Surface area (km^2)	Average thickness (m)	Mass (Gt)
PII-B[1]	Oct 2011	12	7.6	66	83 ± 0.4	4.97
PII-B-a[2]	Oct 2011	6.7	3.0	14	78 ± 0.4	1.0
M1 *	Jul 2009	5.8	4.0	18	--	--
M2 *	Jul 2009	2.6	1.0	2.0	--	--
M3	Apr 2012	3.6	1.7	4.6	--	--
WH1*	May 2009	6.2	2.7	11	--	--
WH2*	May 2009	4.4	2.3	7	--	--

[1]2011-09-07, [2]2011-09-12, *De Abreu et al. 2011

Table 3.3: GPS tracking beacons details.

Ice island	Date deployed	Location of deployment	Time interval	Days tracked	Displaced distance (km)	Company & Model
PII-B-1	23-Oct-2011	69.6N 65.9W	hourly	639	140	MetOcean Polar iSVP
PII-B-2	23-Oct-2011	69.6N 65.9W	hourly	342	340	MetOcean Polar iSVP
PII-B-a	02-Aug-2011	74.1N 85.1W	dozens d^{-1}			Oceanetic Drifter/MetOcean
*PII-B-a	10-Nov-2012	74.3N 87.9W	dozens d^{-1}	720**	800**	CALIB ARGOS
M1 & M2	11-Jul-2009	81.4N 98.1W	hourly	658***	1500***	MetOcean Iridium GPS
M3	19-Apr-2010	79.7N 106.9W	dozens d^{-1}			MetOcean CALIB ARGOS
M3	6-Apr-2012	71.9N 125.2W	10 min	936**	2200****	MetOcean Iridium GPS
WH1	19-May-2009	80.4N 102.8W	hourly	320	180	MetOcean CALIB ARGOS
WH2	19-May-2009	80.5N 101.8W	hourly	840	720	MetOcean CALIB ARGOS

*Using longest lasting beacon, ** combination of beacon segments, ***Beacon on M1, ****Used 3 points (mid-point at location of second beacon deployment).

Table 3.4: Correlation matix of environmental variables and deterioration rate using all available data. T_a_Ice = Interaction term of T_a and Ice. Above and below the diagonal line are the r_s values and p-values, respectively.

	Ta	SST	Ice	Ta_Ice	DAZ	MDD	Rate
Ta	*****	0.782	-0.365	0.988	0.652	0.689	0.186
SST	<0.001	*****	-0.446	0.788	0.551	0.581	0.278
Ice	<0.001	<0.001	*****	-0.377	-0.228	-0.228	-0.430
Ta_Ice	<0.001	<0.001	<0.001	*****	0.640	0.674	0.210
DAZ	<0.001	<0.001	0.016	<0.001	*****	0.922	0.046
MDD	<0.001	<0.001	0.016	<0.001	<0.001	*****	0.063
Rate	0.050	0.003	<0.001	0.026	0.634	0.513	*****

4.0 Surface ablation model evaluation on a drifting ice island in the Canadian Arctic

4.1 Introduction

One consequence of Arctic climate change is an increased frequency in break-up events of ice shelves and floating glacial tongues, which create drifting ice islands (large tabular icebergs) that are hazards to navigation and offshore infrastructure (Mueller et al., 2008; Peterson, 2005). Ice islands have been increasing in occurrence off the east coast of Canada (Peterson, 2005) and in the Arctic Ocean (Copland et al., 2007). These ice masses present serious risks to shipping and resource extraction infrastructure (McGonigal et al., 2011; Peterson, 2011) due to their extreme mass and dimensions, particularly the low drafts (depth below waterline) which allow for drift into industrially active, shallow waters (Ballicater, 2012). The deterioration mechanisms and drift patterns of ice islands are poorly understood since they have been relatively uncommon in Canadian Arctic waters until recently. There is a urgent need to improve our ability to monitor and model ice island deterioration and drift as they are increasingly observed in waters rich in natural resources which are poised for future exploration and development (Peterson, 2011) and increased ship traffic (Prowse et al., 2009).

Dimensional output from the operational ice island deterioration model is used as input to the subsequent ice island drift model, therefore the former must have high model skill for accurate drift forecasting. Savage (2001) and Kubat et al. (2007) detail the processes by which an iceberg deteriorates. Five of these are explicitly included in the CIS operational deterioration model designed for icebergs: 1) solar radiation causing surface ablation, 2) buoyant vertical convection, 3) forced convection from wind and water currents, 4) wave erosion, and 5) calving of overhanging slabs resulting from wave erosion (Fig. 2.5, Table 2.1). Surface ablation, in this chapter, refers to surface melt calculated as the lowering of the horizontal, above-water surface of an ice island as stated in Section 1.2. Surface ablation was found to average a relatively low

(2.8%) of the total observed deterioration in previous studies on traditional icebergs (non-tabular or tabular with smaller surface dimensions) (Savage, 2001). Crocker et al. (2013) state that surface ablation will have a larger effect on the overall deterioration of ice islands compared to traditional, non-tabular icebergs due to an ice island's extensive horizontal surface. The proportion of total deterioration contributed by surface ablation will increase as the waterline length, the surrogate for size and mass in deterioration modeling (Kubat et al., 2007), of an ice island increases. It is predicted that an ice island with a 2 km waterline will experience approximately 10% of mass loss via surface ablation. This increases to approximately 30% for an ice island with a 10 km waterline (Ballicater, 2012). An example of the mass loss by surface ablation for an ice island is provided by Halliday et al. (2012) who document the surface ablation observed for PII-A, a product of the 2010 Petermann Glacier calving event. This 62 km^2 ice island was visited twice between June and July 2011 when adrift off the coast of Labrador. The average surface ablation (n = 4) was 1.72 m over 35 days (Halliday et al., 2012). Based on an estimated extent of 62 km^2 (Halliday et al., 2012), this equates to a mass loss of 9.6 x 10^4 tonnes.

An ice island research project was initiated by the CIS and ArcticNet in 2011 to gather data for the purpose of recalibrating the existing iceberg deterioration model for ice islands. A comprehensive 4-week microclimate dataset was recorded for a small ice island unofficially named Berghaus (Fig. 4.1) as it drifted off the north and east coast of Bylot Island (Fig. 4.2).
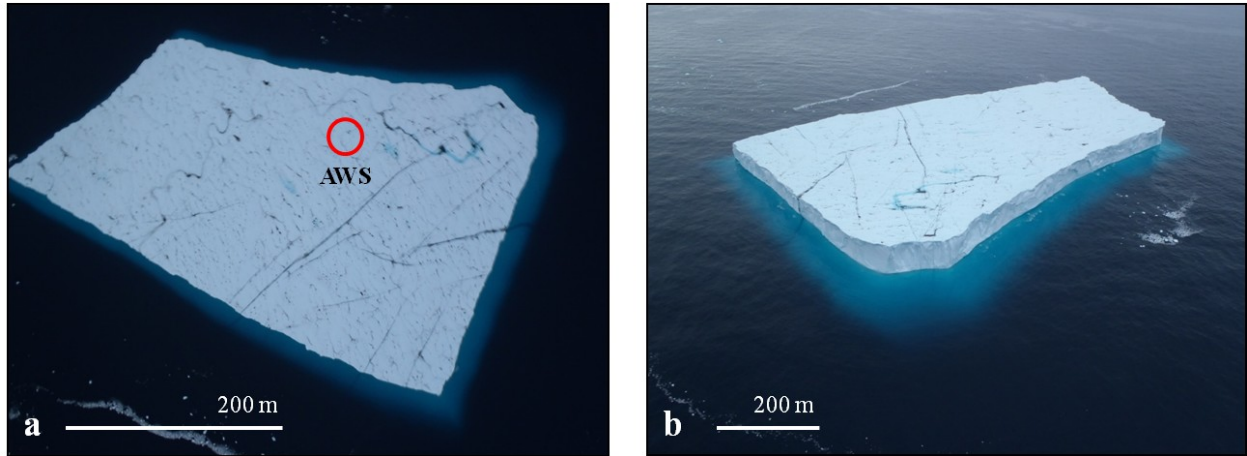
Figure 4.1: Near vertical (a) and oblique profile (b) aerial photography of Berghaus. The location where the automated weather station (AWS) was situated is circled (a).
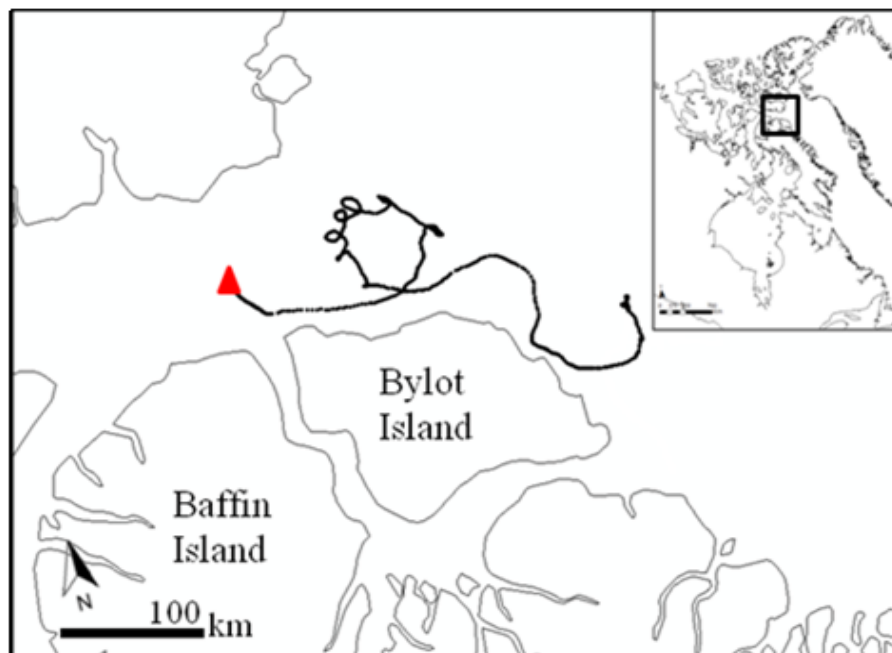
Figure 4.2: Drift of Berghaus: 30 July 2011 (red triangle) - 29 September 2011.

This is a unique dataset for an Eastern Canadian Arctic ice island, which included hourly surface ablation measurements from the automated weather station's (AWS) sonic ranger (Fig. 4.3). AWS environmental variables included relative humidity (RH), air temperature (T_a), atmospheric pressure (APress), net radiation (Q_N), incoming and reflected shortwave radiation ($K\downarrow$ and $K\uparrow$), wind speed (U_s) and wind direction, among others. Correlations between climate variables and surface ablation, and surface ablation model performance, were evaluated with this dataset. The ice island's surface energy balance was calculated as well with the environmental data and provides insight into which energy fluxes are driving Berghaus surface ablation.

Figure 4.3: Automated weather station installed on Berghaus.

Calibrating and/or modifying existing surface ablation models, specifically for use in operational ice island deterioration modeling, is a first step in improving the knowledge of the ice island deterioration processes. The objective of this study is to compare existing model outputs to observed surface ablation on a drifting ice island and provide recommendations for

future surface ablation modeling. Three existing surface ablation models were forced using the AWS data: 1) the CIS iceberg deterioration model (Kubat et al., 2007), 2) a newly-developed ice island energy balance (EB) model which quantifies surface fluxes to determine residual heat energy available for surface ablation (Ballicater, 2012), and 3) a temperature-index model (TIM) which empirically relates air temperature (T_a) and surface ablation (Hock, 2003; Hock, 1999, Hock, 2012).

A fourth surface ablation model was empirically-derived from the AWS dataset using binary recursive partitioning (regression tree modeling) to determine which environmental variables (and/or variable interactions) explain the most variation in surface ablation. Recommendations include model type and complexity, plus which environmental variables to input versus those to keep constant at an estimated value in operational models. It is hypothesized that a relatively sophisticated EB surface ablation model will show the greatest skill for ice island surface ablation modeling, while TIMs prove attractive due to limited climate input data, acceptable forecast accuracy and computational ease. This study will evaluate ice island surface ablation modeling methods for possible use in a full operational deterioration model, as well as improve the understanding of individual microclimate forces on the surface ablation process.

4.2 Study Site

The 270 km^2 Petermann Ice Island (PII) calved on 5 August 2010 from the Petermann Glacier of northwest Greenland (81°N, 61°W) (Johannessen et al., 2011). Berghaus, a 0.13 km^2 fragment, most likely from the original 2010 PII (Fig. 4.1), was accessed on 30 July 2011 from the CCGS *Amundsen* (Forrest et al., 2012). Berghaus was located off the northwest coast of Bylot Island in Lancaster Sound (74°06'N, 81°12'W) at the time of survey (Fig. 4.2). Thickness

varied from 124.5 to 131.2 m (GPR measurement - see Section 3.4.2) and freeboard was estimated between 18-25 m. Length and width ranged from 190-260 m and 260-460 m, respectively, and mass was estimated at 114,300 kg (Forrest et al., 2012).

Rapid deterioration of Berghaus caused discontinuation of AWS data transmission within four weeks of initial survey. The station last reported at 73°29'N and 75°07'W, 200 km (0.5 deg south) from where it was installed at the start of the experiment. Based on hourly position reports, the ice island drifted 560 km over the four weeks and its looping drift track is illustrated in Figure 4.2.

4.3 Methods

4.3.1 Data collection

The AWS was installed on Berghaus on 30 July 2011 and was supported by a tripod atop of vertical wooden posts drilled into the ice (Figs. 4.1 & 4.3). Data was collected every 60 seconds and averaged hourly for the 4-week observation period. A CR3000-XT datalogger (Campbell Scientific Inc., Lincoln, NE) and Iridium L-Band modem transmitted data for remote data collection. The AWS was equipped with a Kipp and Zonen (Delft, Holland) NRLite2 net radiometer, two Kipp and Zonen CMP-3-L pyranometers (down-welling and up-welling solar radiation), a Vaisala (Helsinki, Finland) HC2-S3-L hygrometer/thermistor (RH and T_a − 1.8 m above surface), an RM Young (Traverse City, Michigan) Marine 05106-10-L anemometer (U_s and direction − 2.4 m above the surface), an RM Young 61302V barometer (air pressure), a Hemisphere V101 GPS (position), five Campbell Scientific 109B thermistors (ice temperature) at initial depths of 10, 60, 110, 160 and 210 cm below the ice surface and an SR50A sonic ranger (surface ablation) (Campbell Scientific).

4.3.2 Energy flux calculations

The AWS data collected from Berghaus allowed for the determination of the full surface EB on the ice island either through direct measurement (Q_N, $K{\uparrow}$ and $K{\downarrow}$) or through calculation. $L{\uparrow}$ was calculated using the Stephan-Boltzman relationship and the surface temperature, taken from the ice thermistor closest to the surface (not melted out). Emissivity of ice was set to 0.97 in accordance with Ballicater (2012). This is the upper limit of the emissivity range of sea ice as reported by Oke (1987) but is lower than the 0.985 emissivity value reported for glacial surfaces by Lougeay (1974). This study did not assess the impact of changing the emissivity value from 0.97 but acknowledges the need to do so in the future. $L{\downarrow}$ was calculated by completing Equation 2.2 after substituting Q_N, $L{\uparrow}$, $K{\downarrow}$ and $K{\uparrow}$. The sign convention for energy and radiation fluxes is negative when directed away from the ice and positive when directed towards the ice (Knox, 2011; Oke, 1987)

Sensible (Q_S) and latent heat flux densities (Q_E) and their contributions to available melt energy (Q_M) were calculated through the BAA, using the same equations and parameter values as Ballicater (2012) (Eq. 2.3 and 2.4). Surface temperature was held constant at 273.15 K, the assumed temperature of melting ice (Ballicater, 2012). The ice temperature profile provided by the Berghaus AWS (Fig. 4.4) allowed for the calculation of the ground heat flux (Q_G) and assessment of this energy flux's magnitude. The Q_G is calculated with the gradient method previously employed by Pellicciotti et al. (2009) on several glaciers. Male and Gray (1981) provide the equation (4.1):

$$Q_G = - k \, (\Delta T / \Delta z) \tag{4.1}$$

where $\Delta T / \Delta z$ is the change in temperature over depth. In this case, the difference was taken between the closest-to-surface thermistor (not melted out and recording air temperature) and the

thermistor 1 m below. Thermal conductivity (k) was set to 2.07 W m^{-1} K^{-1} (Male and Gray, 1981).

4.3.3 Statistical Analysis

All statistical analysis was carried out in R (Version 2.14). The most important parameters for modeling hourly surface ablation were determined and visualized through correlation analysis and regression tree modeling (Crawley, 2007). Due to non-normal distributed variables ($K\uparrow$, $K\downarrow$, T_a), a correlation table using Spearman`s r (r_s) was created to determine the association between environmental variables and hourly surface ablation, as well as cross-correlation between variables.

A non-parametric regression tree was used to predict hourly surface ablation and illustrated the data structure, variable interactions and hierarchy between environmental variables for varying magnitudes of surface ablation (Merkle and Shaffer, 2010). This method partitions the variance in the response variable into groups that can be explained by a given combination of explanatory variables at set threshold values. The tree reads like a series of decisions, where at each node a decision is made based on a variable, and its corresponding threshold, that maximally divides the remaining data. This continues for each sub-group until no improvements to the explanation of the response variable can be made. At the bottom of the tree, or the end of the explanatory variable splitting, there are a set number of values of the response variable for each combination of explanatory variables (Therneau et al., 1997).

Specifically for this study, splitting in the tree occurs at thresholds of environmental variables which explain hourly surface ablation. These thresholds divide the dependent variable (hourly surface ablation) into two groups (or branches) which have maximally different means and minimal deviance (sum of squared errors). This is repeated for each branch of the tree until

further deviation can no longer be explained by partitioning or there are too few data points to do so (Crawley, 2007). Tree models differ from multiple linear regression (MLR) by being fit through forward stepwise-selection of variables (MLR uses backward stepwise-selection) and the binary recursive partitioning procedure detailed above (Crawley, 2007). Tree models are often utilized when there are many causative variables that make it impossible to assess interactions between all variables in regular regression modeling. Regression tree models were used for hourly surface ablation analysis over MLR modeling due to the multiple interaction terms between environmental variables that are not illustrated with MLR (Merkle and Shaffer, 2010). The 'rpart' package (Therneau et al., 2013) was utilized for tree modeling. In order to ensure that the tree model was fit in a robust manner, a permutation was performed whereby one tenth of the data was removed and the model was fit on the remaining data. This was repeated ten times, with a different subset of data removed from the original dataset for each permutation. The results were then averaged for the creation of the tree model that maximized R^2 and minimized deviance (mean squared error). Ten-fold cross-validation was also completed when predicting hourly surface ablation from the tree model.

The tree developed and used in this study to illustrate parameter structure when explaining hourly surface ablation was developed from the entire dataset (r-part tree model above). Random forest was used to determine and visualize variable importance on hourly surface ablation. Random forest analysis is another recursive partitioning method used for sub-sampling and cross-validating non-linear data during multiple regressions (Strobl et al., 2009). Benefits of the random forest method include its ability to deal with multiple explanatory variables and their interactions, and then subsequently give an accurate illustration of variable importance (Strobl et al., 2009; Breiman and Cutler, 2013). Single tree models (as in 'rpart' above) developed on a single subset of data, are extremely sensitive to the sub-sampled data and

can change structure easily between subsample runs. This instability is thus removed by averaging the results of many sub-sampled trees (ensemble) with the random forests computation. Since numerous trees are created with random forests, it is impossible to visualize a final, single tree (Strobl et al., 2009).

Random forest analysis gives a more robust assessment of variable importance since the ensemble method gives explanatory variables multiple chances to reorder their interaction structure based on the respective subset of data used for each tree. These 'order effects' are averaged out with the ensemble of trees and allows the true variable importance to be assessed (Strobl et al., 2009). Here, half of the data matrix was used as a subsample for cross-validation and 100,000 trees were created. Instead of using forward selection (as tree modeling above), variables are removed and re-added to determine the out-of-bag error (percent increase in mean square error) (Strobl et al., 2009).

4.3.4 Surface ablation modeling

4.3.4.1 Operational surface ablation models

Both the operational iceberg and ice island models developed by Kubat et al. (2007) and Ballicater (2012) are EB models, yet they vary greatly in the number of parameters and variables included and which environmental variables are held constant or use external input data (Table 4.1). External input data may be supplied by other models or direct measurement. The models were run with the variables set to those recommended by the respective authors. Both were also run with the substitution of environmental variables that were collected by the AWS in 2011. Models were evaluated on their ability to accurately predict the observed, cumulative surface ablation of Berghaus. This was calculated as the percent difference between modeled and

observed surface ablation. Models were also evaluated on their hourly surface ablation predictions with their respective root mean squared error (RMSE) values.

The CIS iceberg surface ablation model (Eq. 4.2) was run twice, both times with observed $K\downarrow$ (sole environmental input). The first run was conducted with the assigned α value of 0.7 (Savage 2001), while the second run used the AWS median albedo ($\alpha = K\uparrow/K\downarrow$) as input.

$$R = [K\downarrow/(\rho_i\Gamma)](1-\alpha) \tag{4.2}$$

The EB surface ablation model included in the Ballicater (2012) ice island deterioration model requires T_a and ΔU, the difference between 10 m wind (U_2) and ice island drift speed, (U_1) input. The AWS U_s was corrected to a standard 10 m height using the power law relationship (Eq. 4.3), with an exponential parameter (a) set to 0.143. This is akin to a surface roughness of 3-4 cm and is a reasonable input value for neutral stability conditions (Tuoma, 1977; Robeson and Shein, 1997), which are prevalent over the ocean (Hsu et al., 1994). Differential speed between Berghaus and wind was not calculated but this should have minimal effect on model prediction (G. Crocker, pers. comm., 2013).

$$U_2=U_1(Z_2/Z_1)^a \tag{4.3}$$

where U_1 and U_2 are wind speeds (m s^{-1}) at heights (m) Z_1 and Z_2.

The Ballicater (2012) ice island surface ablation model is based on a full EB; however many of the variables were parameterized (Table 4.2 and Section 2.5). Two model runs were completed: 1) forced with the normal environmental input data used for operational modeling (T_a and 10 m U_s), and 2) with AWS data wherever possible (median α, RH, $K\downarrow$, U_s and T_a).

Another EB model, developed by Brock and Arnold (2000), was run to compare output to Ballicater (2012). The two models are based on the same theory and general equations, with the Brock and Arnold (2000) model developed for glacial surface ablation modeling and use of data collected from small weather stations. The Brock and Arnold (2000) model was forced with the

required AWS ($K{\downarrow}$, T_a, U_s and APress) data for comparison with the Ballicater (2012) EB model. Surface roughness values can be modified by the user for the glacial surface ablation model (Brock and Arnold, 2000). A value of 2 cm was used for initial comparison. The results of both models were similar (1.5% difference) and it was decided to focus on the operational ice island surface ablation model in use by the CIS (Ballicater, 2012) for this study.

4.3.4.2 Temperature index model

A TIM (Eq. 2.6; Hock, 2003) was run with PDD input calculated from AWS T_a data. An initial DDF, which relates PDD to surface ablation through the close relationship of T_a and surface ablation, was selected from a review of various studies which reported DDF values for snow and ice (Hock, 2003). The most comparable DDF to the location and environmental conditions of Berghaus was reported for the John Evans Glacier (Canada) during sampling in July 1996 (Arendt and Sharp, 1999). This DDF (7.6 mm d^{-1} $°C^{-1}$) was chosen for the Berghaus analysis due to the study's summer sampling season and low altitude (260 m) and was used for the initial model run (Hock, 2003; Braithwaite, 1995). The value was initially chosen by Arendt and Sharp (1993) by averaging 13 DDFs for ice from values reported by Braithwaite (1995).

To address DDF fit and validation, as well as the idea put forward by Arendt and Sharp (1999), that DDFs need to be modified throughout the melt season, the data was divided in half (first 14 day vs. second 14 day period). A regression equation was fit using the initial 7.6 mm d^{-1} $°C^{-1}$ DDF and TIM-predicted surface ablation with this DDF. The equation was solved to find the best DDF fit for the first period after substitution of the observed surface ablation value. The fitted DDF was used subsequently in the second data period's model run, as well as the entire dataset, to validate the TIM and calculated DDF value.

This model was tested by hindcasting surface ablation using climate reanalysis data (regional monthly T_a data (NCEP/NCAR, 2013)) to determine the model's forecasting accuracy with input data similar to what is available to operational modelers. Data from NCEP/NCAR reanalysis was used as a substitute for GEM (Global Environmental Multiscale model) input normally used by CIS operations. The TIM and optimal DDF calculated for the entire Berghaus dataset were validated using T_a reanalysis data and surface ablation records from PII-A (Halliday et al., 2012).

4.4 Results

4.4.1 AWS data

The surface T_a observed on Berghaus, initially recording 1.8 m above the surface, ranged from 1.7°C to 12°C (mean = 5.1°C) (Fig. 4.4). Median RH was 97%, with minimum and maximum values of 57% and 100%, respectively. The mean RH was 93%, with 95% of the data being within the range of 84-100% (1 standard deviation) and average U_s was 2.7 m s^{-1}. Between the first and second periods of data collection mean α rose from 0.6 to 0.9.
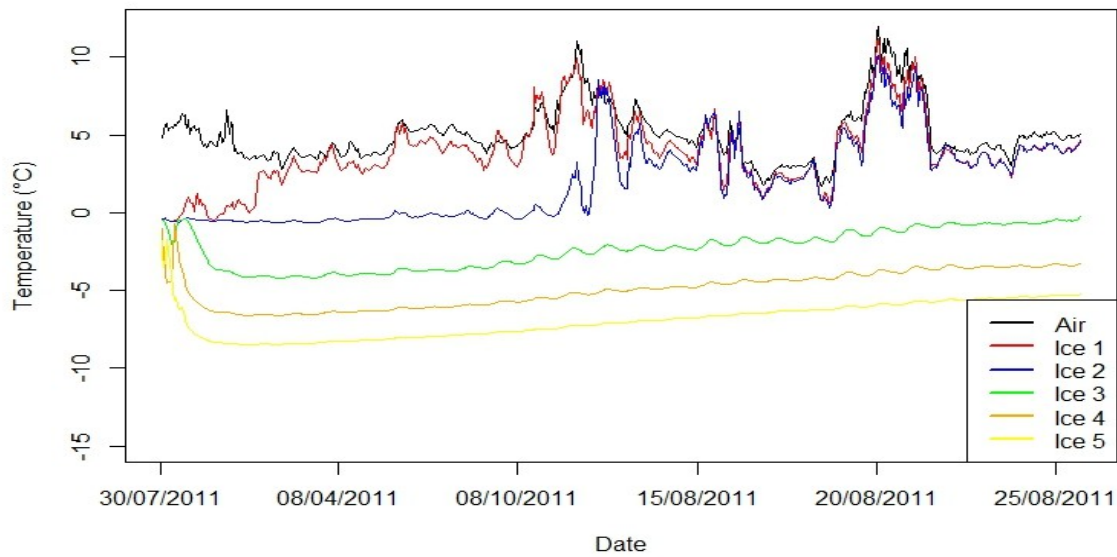
Figure 4.4: Air and ice temperature profiles on Berghaus. Ice thermistors 1, 2, 3, 4 and 5 were originally inserted 10, 60, 110, 160 and 210 cm beneath the ice surface. Ice 1 begins recording air temperature on day 2 and Ice 2 on day 16.

Figure 4.5 illustrates the radiation fluxes recorded and calculated on Berghaus. $K\downarrow$ showed typical diurnal variability but cloud cover is assumed to have increased due to a low pressure period towards the end of measurement period. $L\downarrow$ supplied the greatest amount of radiation energy to the surface (average 277 W m^{-2}) while $K\downarrow$ supplied 125 W m^{-2} on average. Since the ice surface temperature remained near zero, $L\uparrow$ was only slightly less than $L\downarrow$ and the net receipt of longwave radiation available for melt averaged 26 W m^{-2}. Due to a high α (mean = 0.75)*, K$\uparrow$ averaged 72 W m^{-2}, resulting in an average net receipt of only 53 W m^{-2} in shortwave radiation.
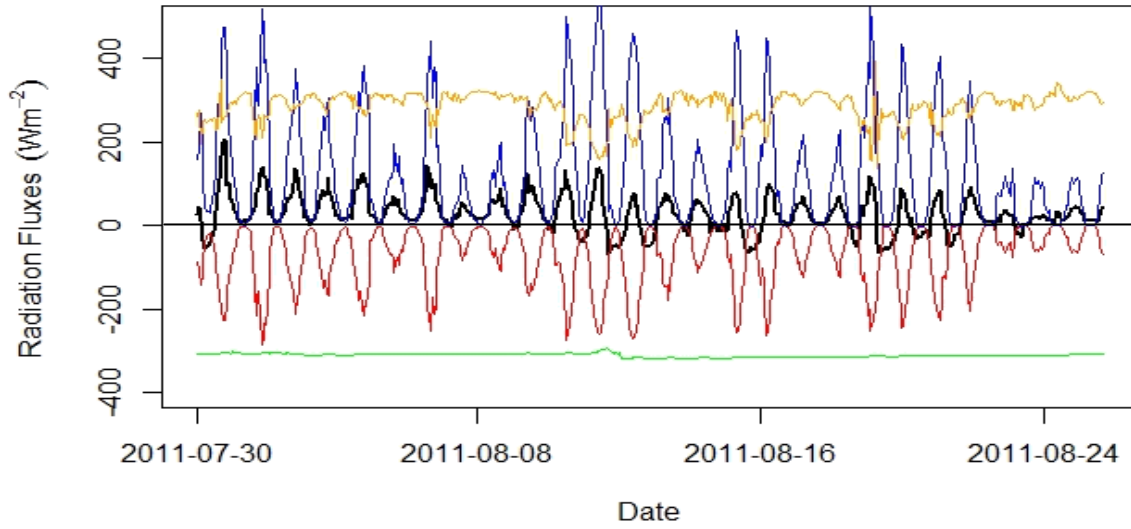
Figure 4.5: Radiative fluxes recorded or calculated for Berghaus energy balance: Q_N (black), $K\downarrow$ (blue), $K\uparrow$ (red), $L\downarrow$ (yellow), $L\uparrow$(green). The dip in $L\uparrow$ on August 12 is due to switching the ice thermistor used for ice temperature input in $L\uparrow$ calculation, since Ice 2 (Fig. 4.4) melted out and began recording T_a on day 18 of data collection.

Berghaus experienced 89.3 cm of cumulative surface ablation over a 4-week period (30 July - 26 August 2011) (Fig. 4.6). It is assumed that this value is representative of the entirety of the constant, gently undulating ice island surface due. With ice density equal to 900 kg m^{-3}, this represents a loss of 116 x 10^3 m^3 of ice, or 104 x 10^3 kg of melt water equivalent (MWE). The two most shallow ice thermistors melted out of the ice surface 4 (2 August 2011) and 18 (16 August 2011) days after AWS installation, representing 10 and 60 cm of surface ablation, respectively (Fig. 4.4).
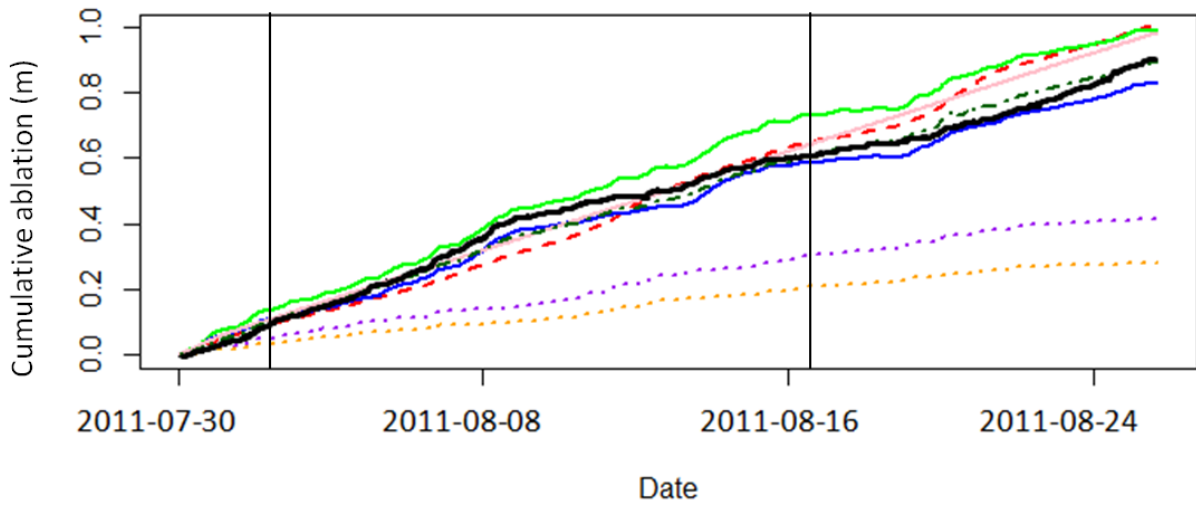
Figure 4.6: Berghaus observed and modeled cumulative surface ablation: observed (solid, black), CIS ice island standard (solid, blue), CIS ice island extra input (solid, green), CIS iceberg standard (••••, orange), CIS iceberg extra input (••••, purple), TIM standard (----, red), TIM with reanalysis data (----, pink), regression tree (·-·-·-·, dark green). See Table 4.2 for model run details. Black lines represent thermistors Ice 1 and Ice 2 melting out of the ice surface (Fig. 4.4).

4.4.2 Energy flux contributions to available melt energy

Daily total energy flux densities and their relative contribution are shown in Figure 4.7. The potential contribution towards surface ablation and correlations between T_a and energy fluxes were investigated. T_a was highly correlated (p<0.001) with $L\downarrow$, $K\downarrow$ and I. The radiation variable with the strongest, significant correlation to T_a was $L\downarrow$ (r=0.55). Both Q_S and Q_E were significantly correlated (p<0.05) with T_a and had an r_s of 0.41 and -0.22, respectively. All energy fluxes were significantly correlated with Q_M.
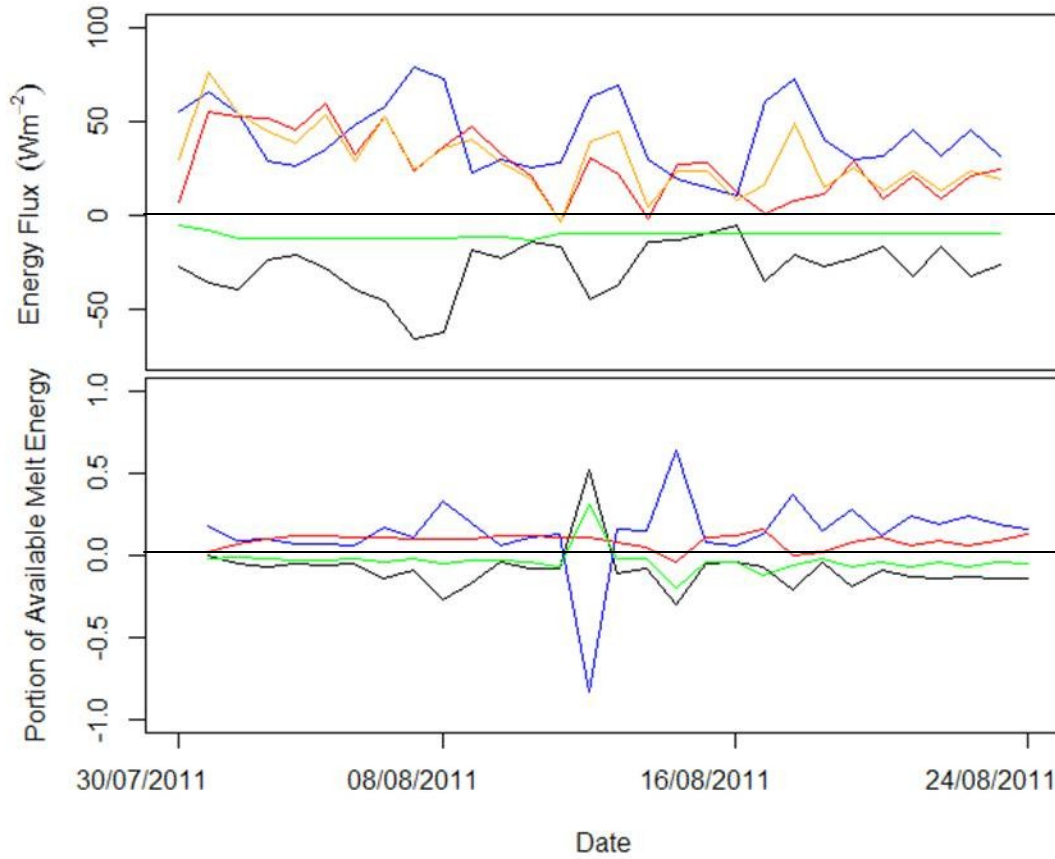
Figure 4.7: Top: Daily average energy flux densities. Bottom: Relative portion of energy fluxes to available melt energy (Q_M) over past 24 hours. Colour representation is: Q_E (black), Q_S (blue), Q_N (red), Q_G (green) and Q_M (orange).

Of the four energy fluxes calculated or measured in this study (Q_N, Q_G, Q_E, Q_S), Q_G had the least magnitude with hourly observations ranging between -0.38 to -17 W m^{-2}. The maximum hourly value of Q_S was 164 W m^{-2} and minimum value of Q_E was -114 W m^{-2}. The relative contribution of each energy flux to Q_M is plotted in Figure 4.7. Average Q_M was negative for only one daily period. Q_S, Q_E and Q_G switched their respective normal flux contributions on this day (Fig. 4.7). Q_M followed Q_N and was associated with a large positive r-value of 0.93 (p<0.05). Q_G and Q_E always removed energy from the surface and never contributed energy to Q_M. The Q_M

time series is plotted with observed surface ablation and showed good general agreement (r=0.47, p<0.001) (Fig. 4.8).
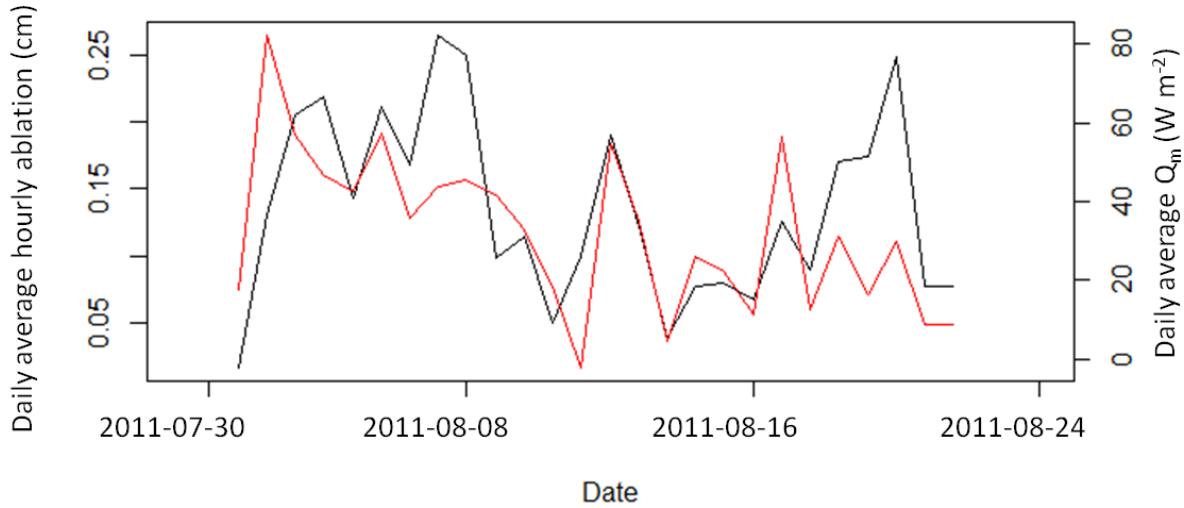
Figure 4.8: Hourly surface ablation averaged daily (black) and Q_M (red).

4.4.3 Statistical analysis of AWS data

Variables with significant associations (p<0.05) to hourly surface ablation were U_S, T_a, $K{\downarrow}$, and Q_N (Table 4.3). The strongest correlation was between hourly surface ablation and U_s (r=0.19) (Table 4.3). As expected, high multicollinearity was apparent between the radiation variables (Q_N, $K{\downarrow}$, $K{\uparrow}$) and α. The two radiation variables retained for regression tree modeling were $K{\downarrow}$ and α as they were not correlated with each other.

The tree model (Fig. 4.9) created with a 10-fold cross-validation included U_s, $K{\downarrow}$, RH, T_a and APress. The first and most influential branching occurred at a threshold of RH (62.5%). There are only 11 observations (1.7%) of RH below this threshold. When RH is above 62.5%

(98.3% of data collection period), a split at U_s (1.5 m s^{-1}) is then able to explain the most variability in hourly surface ablation. $K\downarrow$ explains hourly surface ablation at $U_s < 1.5$ m s^{-1} when following the left branch, as well as for U_s between 1.5 m s^{-1} and 4.7 m s^{-1} after a second partition based on U_s.

Continuing along the left branch, hourly surface ablation is maximally partitioned by T_a at low $K\downarrow$ (< 344.7 W m^2), followed by atmospheric pressure for $T_a \geq 8.3°C$. A cross-validated model prediction of cumulative surface ablation was 89.3 cm and root mean square error (RMSE) was 0.29 (Fig. 4.6). Residuals had a mean of zero and with non-significant skew but did exhibit significant kurtosis.

The random forest analysis was run with the same variables as the regression tree above to determine variable importance with ensemble modeling (Fig. 4.10). The removal of RH causes the mean square error to increase the most (114%). This is followed by T_a, U_s, α and $K\uparrow$ (101%, 97% and 49% and 27%, respectively).
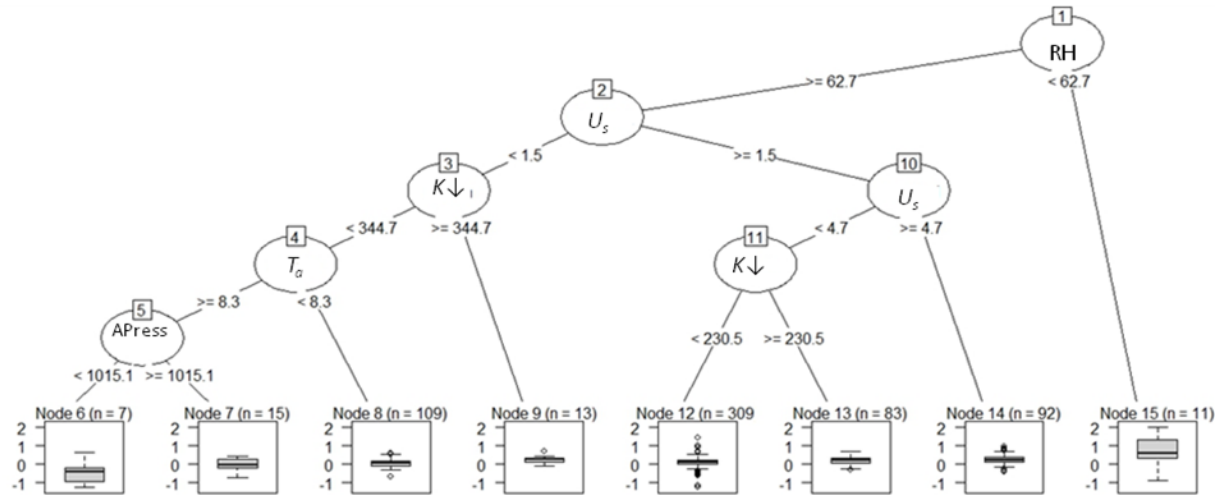
Figure 4.9: Regression tree analysis results depicting which AWS variables (and their threshold values) explain the greatest variation in hourly surface ablation. Boxplots depict z-scores of hourly surface ablation records recorded under conditions of the respective branch.
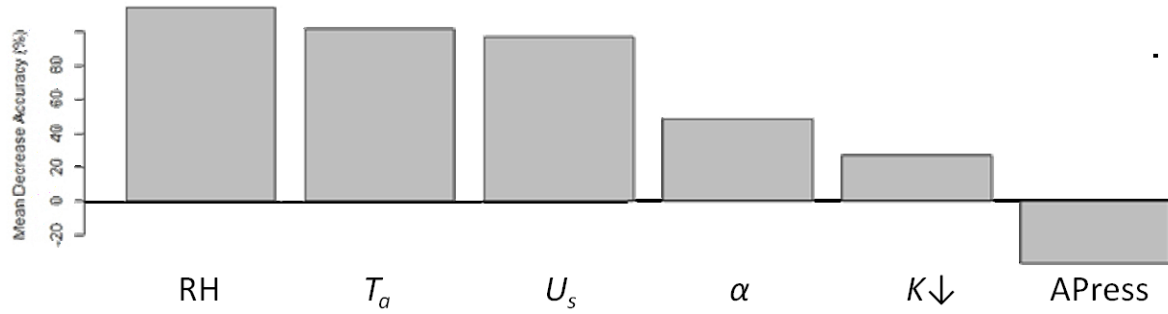
Figure 4.10: Variable importance as distinguished by random forest analysis.

4.4.4 Modeling results

Cumulative surface ablation output of all models is illustrated in Figure 4.6. Table 4.2 gives input variables, results and errors for the different models used in this study. The CIS iceberg surface ablation model under-predicted cumulative Berghaus surface ablation by 68% (28 cm predicted surface ablation) and had a RMSE of 35.9 cm when run with the suggested α of 0.7 and observed $K\downarrow$ (AWS data). When run with the observed median α of 0.56, the model still under-predicted by 53% (41 cm predicted total surface ablation) and RMSE was 27.9 cm.

When running the CIS ice island surface ablation model, runs conducted with 10 m U_s input extrapolated with a power-law input value of 0.143 and without extra AWS inputs (RH, $K\downarrow$, median α) modeled observed, cumulative surface ablation most accurately (7.5% under-prediction, RMSE = 50 cm). When more data collected from the AWS was used to force the model, the RMSE decreased to 0.09 cm and cumulative surface ablation was over-predicted by 10%.

The initial TIM run (DDF = 7.6 mm d^{-1} °C^{-1}) predicted 50.4 cm cumulative surface ablation for the calibration period (14 days). When a regression equation was solved the fitted

calibration period DDF was 7.3 mm d^{-1} °C^{-1} (RMSE = 0.06 cm). When applied to the validation period (14 days), RMSE was 0.09 cm and the model over-predicted by 28%. When applied to the entire melt period, observed surface ablation was 101 cm (12% over-prediction) and RMSE = 0.09. The best fit DDF for the full 4 weeks of melt was 6.8 mm d^{-1} °C^{-1} (predicted surface ablation of 91.0 cm) (Table 4.2). A DDF of 5.2 mm d^{-1} °C^{-1} was the best fit for the last 2 weeks (RMSE = 0.02). The calibration and validation periods both had mean T_a values of 5.1 °C, mean α values of 0.6 and 0.9 and cumulative surface ablation amounts of 50.4 and 39.3 cm, respectively. The TIM (7.3 mm d^{-1} °C^{-1} DDF) was run with NCEP/NCAR reanalysis data and over-predicted total surface ablation by 9.6% (98.2 cm predicted), with RMSE = 0.05 cm (Fig. 4.6).

The TIM was also run with NCEP/NCAR reanalysis data for the region surrounding PII-A between June 18 and July 22, 2011 (35 days). The TIM predicted 2.0 m of surface ablation over this time period when run with a DDF of 7.3 mm d^{-1} °C^{-1}. This is a 17% over-prediction of average, observed cumulative surface ablation (1.73 m) and 12% over prediction of the maximum cumulative surface ablation recorded (1.80 cm). Minimum surface ablation on PII-A was 1.66 m (Halliday et al., 2012). Predicted, cumulative surface ablation was 1.9 m (10% over-prediction) when run with a DDF of 6.8 mm d^{-1} °C^{-1}. A DDF of 6.1 mm d^{-1} °C^{-1} predicts 1.70 m of surface ablation (0.2% under prediction). Albedo measurements from PII-A were not recorded so it is impossible to see if this site characteristic had a large effect on the variation in the DDF fit as in the Berghaus dataset.

4.5 Discussion

4.5.1 Energy flux and environmental conditions affecting Q_M and surface ablation

Observed surface ablation is a combination of Q_M and Q_E. It was impossible to differentiate the exact contribution of each to surface ablation from the Berghaus AWS records as both contribute to surface ablation through the melting (Q_M), evaporation or sublimation (Q_E) of ice and melt water. Confidence in calculation of the energy fluxes by the BAA is created after plotting Q_M (sum of energy fluxes) to observed surface ablation as they are in general agreement (Fig. 4.8).

Q_S and Q_N were the main suppliers of incoming energy on Berghaus. Figure 4.7 shows that Q_S is the dominate contributor to Q_M for most of the observation period. This is possibly attributed to a high average T_a of 5.1°C, which caused a large vertical gradient between the atmosphere and ice surface (Fig. 4.4). The highly significant correlation (p<0.001) between observed surface ablation and U_s is also in agreement with previous findings that the turbulent fluxes play an important role in surface ablation (Oerlemans and Grisogono, 2002). U_s is an integral component of turbulent heat flux calculations (Ballicater, 2012). In the case of Berghaus, the turbulent fluxes move warm air down to the cold surface, driving both the evaporation and sublimation processes resulting from Q_E transfer and melt from Q_M. Figure 4.9 illustrates the control of U_s over surface ablation as it is the first environmental variable used to explain hourly surface ablation under normal RH conditions. U_s is the only variable necessary to explain hourly surface ablation at high wind speeds (Fig. 4.9) as the contributions of Q_E and Q_S are relatively high (Ballicater, 2012). The random forest analysis (Fig. 4.10) recognizes the importance of U_s, as well as T_a, in hourly surface ablation magnitudes. Since both of these environmental variables contribute to the magnitude of the turbulent fluxes, these analyses confirm the influence of the turbulent fluxes on surface ablation. This is in agreement with Knox et al. (2012) who found Q_S

to be the dominant contributor to surface ablation (53%) during a snow-pack study in Eastern Ontario.

Relative to all the energy fluxes, Q_N correlated best with Q_M. Q_N was better correlated than T_a with observed surface ablation, suggesting that radiative energy, and not turbulent fluxes, drove Berghaus surface ablation. During periods of relatively low U_s (< 0.15 m s^{-1}), which inhibits turbulent atmospheric exchange and results in relatively low Q_E and Q_S contributions (Oke, 1987), the relative contribution of the radiative flux (Q_N represented by $K\uparrow$) to surface ablation increases. Oerlemans et al. (1999) state the importance of radiation input for the magnitude of surface ablation after analysis of AWS data collected from a maritime Icelandic glacier named Vatnajökull, with radiation contributing approximately twice the energy for melt compared to turbulent fluxes. Interestingly, this was not the case on Berghaus, as $K\downarrow$ did not show high importance in random forest analysis (Fig. 4.10) and only was a factor in explaining 22% of Berghaus observations in the regression tree analysis (Fig. 4.9).

Q_E always represented a loss of energy from the ice surface as sublimated or evaporated water vapour was transported into the atmosphere from the surface. Q_E correlated well with Q_S as expected given the common variable, T_a, in their calculation. Since Q_E is calculated using a gradient method, temporal variations in RH and e_a may have contributed to variations in the magnitude of Q_E, which is expected to become more (i.e. greater rates of evaporation and sublimation) during periods of low RH. This is suggested by the highly significant correlation between RH and Q_E (p<0.001) but the Berghaus data is not conclusive in the relationship with a weak r value of -0.23.

The statement by Ballicater (2012) that RH is an important variable in surface ablation modeling is supported by the variation in hourly surface ablation being best explained by a split based on a RH threshold of 62.5% (Fig. 4.9). As well, RH was the most important environmental

variable in random forest analysis (Fig. 4.10). Low values of RH increase the potential evaporation with the greater humidity gradient between the surface and atmosphere (Oke, 1987). However, the AWS only recorded RH values below this identified partitioning threshold for 1.7% of the collection period. These 11 observations can be considered 'extreme cases' and could be considered outliers that a general model may not need to take into account (Crawley, 2007). These were recorded during one 11 hour span when high T_a (10-11°C) was observed and U_s and air pressure were close to normal (4 m s^{-1} and 1014 Pa). RH did not have a significant relationship with hourly surface ablation (Table 3.1), further highlighting that a few extreme values of RH had a large influence on the aforementioned regression trees. Ice islands are located in a maritime environment with high humidity during the melt season. It is suggested that RH continue to be an approximated value in operational models and extra effort in obtaining more accurate data for model runs be focused on other environmental variables.

Q_G also removes energy that could otherwise contribute to Q_M and averages 10% of the EB. The greatest relative Q_G fluxes are observed during periods of minimal Q_N (Fig. 4.7), when the loss of energy from Q_G was not countered by Q_N contributions. Inclusion of Q_G in future EB model development may improve surface ablation accuracy. It is expected that the EB models in this study would over-predict surface ablation by 10% by omitting Q_G in EB calculations. It is interesting that this was not the case, as the Ballicater (2012) model under-predicted surface ablation. Q_G is often omitted in glacial surface ablation modeling (Pellicciotti et al., 2009) since modeling often takes place when surface ablation is occurring and this flux is assumed to be small. Q_G becomes more important when snow is present or in dry environments (Pellicciotti et al., 2009). Further refinement in the operational surface melt model may consider the inclusion of Q_G in EB calculations due to its relatively large diversion of energy away from Q_M.

Albedo has been identified as an important factor in surface ablation magnitude in the past (Oerlemans et al., 1999). Oerlemans et al. (1999) show that α varies temporally, ranging from 0.1 to 0.5 for the study's sites, and is related to surface ablation. Albedo did not surface as a parameter that split an informative amount of the surface ablation data at any stage (Fig. 4.9). In the importance plot (Fig. 4.12), α did surface as the variable that explained the fourth greatest amount of hourly surface ablation. Even though it was not included in the regression tree (Fig. 4.9) further study into accurate α input, either as an estimated parameter or input variable, in EB or TIM models is recommended as the α of Berghaus varied greatly (50%) between the two data subsets.

The correlation matrix (Table 4.3) corroborates other study's findings that U_s and T_a, as well as $K\downarrow$, are important forcing variables in surface ablation modeling (Oerlemans and Grisogono, 2002). As stated above, these variables were seen to explain the variation in surface ablation during normal conditions of RH and are linked to the turbulent and radiative fluxes. U_s and T_a. were also important in random forest analysis. It is thus necessary to input accurate U_s and T_a, and secondarily $K\downarrow$, data into ice island EB surface ablation models and should be a priority for future *in-situ* data collection and model development if EB model use continues.

4.5.2 CIS operational surface ablation models

Ballicater (2012) explains that the surface ablation process plays a larger relative role in overall deterioration for ice islands when compared to traditional icebergs. It is therefore important that this process is accurately represented (not underestimated) in the full ice island deterioration model. Berghaus was a relatively small ice island (0.13 km^2) and it is expected that error in surface ablation prediction will increase as the model is applied to larger ice islands. Both model runs of the CIS iceberg surface ablation model display the diurnal change expected

to occur for the rate of surface ablation, but under-predict observed surface ablation. It is obvious from Figure 4.6 and the high RMSE values (Table 4.2) of model runs that the CIS iceberg deterioration model does not accurately represent the surface ablation occurring on Berghaus during the melt season. This justifies the development of a more adequate surface ablation model for ice islands.

The CIS model developed specifically for ice islands provided a more accurate surface ablation forecast than the original CIS iceberg model (decreased under-prediction from 69% to 7.5%). It was surprising that the addition of extra AWS input data (RH, $K\downarrow$ and median α) resulted in decreased model accuracy (10% over-prediction). A small bias built up over time for the added data run, but was cancelled out in the normal run (Table 4.2), which made its final cumulative output accurate. This is interesting, as the added input of *in-situ* RH, $K\downarrow$ and median α should have increased model skill. The fact that the model decreased in accuracy upon substitution of the median observed α is a warning that the model needs additional tuning. By lowering the α value to 0.6, the predicted surface ablation increased by decreasing $K\uparrow$ input and increasing Q_M. It would be beneficial to test the model in a variety of environments with varying RH and $K\downarrow$ conditions and periods of melt magnitude and consider the use of an evolving α value.

The largest contributors to Q_M and surface ablation on Berghaus were most often Q_E and Q_S (Fig. 4.7). Previous studies (Oerlemans and Grisogono, 2002; Oerlemans, 2001) have stated that surface ablation sensitivity is dependent on $L\downarrow$, $L\uparrow$, Q_E and Q_S, as well. This study finds that the inclusion of the turbulent fluxes (Q_E and Q_S) is a large asset to the ice island surface ablation model (Ballicater, 2012).

It was noted that a change in the value of surface roughness did affect the magnitude of forecasted surface ablation by 9-10% when α was held constant when forcing the Brock and

Arnold (2000) glacial surface ablation model. This is expected as greater roughness has the potential to increase turbulence and enhance the turbulent flux exchanges between the atmosphere and ice surface (Oke, 1987). Care should be taken to input the most accurate value for surface roughness when it is a parameter (individual or embedded within the turbulent coefficient) of a surface ablation model. Attention should also be given to the value assigned to the emissivity of ice used in operational models due to the variation in values presently used in models and those reported by past studies.

4.5.3 Temperature index model

TIMs have been successful in predicting surface ablation of glaciers due to the good correlation between T_a and the main sources of Q_M: $L\downarrow$, $K\downarrow$ and Q_S (in order of importance) (Ohmura, 2001). The benefit of the TIM for operational use is the simplicity of input, with PDD being calculated directly from T_a data. A TIM would have a maximum of two variables (PDD and DDF).

When the calibrated DDF (7.3 mm d^{-1} °C^{-1}) was applied to the validation period, surface ablation was largely over-predicted. Arendt and Sharp (1999) advocated a non-constant DDF to allow the changing surface conditions (mostly α) during a melt season to be taken into account when modeling surface ablation. If conditions do not change considerably it is not necessary to modify the DDF (Hock, 2003). However, it is recommended that a non-constant DDF be used if a TIM is adapted for ice island modeling, as a constant α was not observed on Berghaus and it is likely that the observed change in α on Berghaus caused the TIM inaccuracy over the validation period.

The best fit TIM for the entire dataset used a 6.8 mm d^{-1} °C^{-1} DDF. This is very close to the constant value (6.84 mm d^{-1} °C^{-1}) used by Arendt and Sharp (1993) for iced surfaces and falls

within the values determined by Braithwaite (1995) for ice surfaces. When applied to the entire dataset, error was low (RMSE = 0.06 cm, 1.9% over-prediction). The accuracy when regional reanalysis T_a data is used as input is another asset to the TIM method for operational modelers.

The TIM over-predicted surface ablation by 17% on PII-A when using a DDF of 7.3 mm d^{-1} $°C^{-1}$ and regionally estimated T_a data. A DDF of 6.1 mm d^{-1} $°C^{-1}$, fit for PII-A, predicted 1.72 m of surface ablation (0.2% under-prediction of average PII-A surface ablation). The two ice islands were separated by 20° latitude and mean reconstructed T_a differed over the respective study periods by 1.8°C. Modifying the DDF by location or mean T_a could be a way forward if implementing this approach in ice island surface ablation modeling during drift. The applicability of this model for operational use would be determined by whether or not a modeler would use a non-constant DDF.

4.5.4 Overall model comparison

Results from the original CIS iceberg deterioration model demonstrate the necessity for improved surface ablation modeling for ice islands, and possibly typical icebergs as well. The new CIS ice island deterioration model improved accuracy of predicted surface ablation. Further investigation is warranted towards the study of why the CIS ice island surface ablation model became more inaccurate with the addition of extra AWS input. However, with and without the extra input, this model predicts within 10% of observed surface ablation. This is not as accurate as the best-fit TIM (1.9% over-prediction) but is more accurate than the cross-validated TIM (12% over-prediction). The TIM's operational ease, ability to incorporate regional environmental data and minimal necessary input from other environmental models may be overshadowed by the confidence inspired by the EB model developed by Ballicater (2012). The EB model is more likely to work acceptably in a variety of situations by incorporating various environmental

conditions and including the turbulent energy flux energy calculations. However, T_a and U_s data will come from the GEM model in use at the CIS for their operational EB model. This can compound model error (error from the GEM being carried through the surface ablation model, plus additional error inherent in the EB model). The ice island EB model's complexity is much greater than the TIM as well, with 17 included parameters (Table 4.1). These are all items for operational modelers to consider when deciding on the best method for ice island surface ablation modeling.

4.6 Conclusions

Inaccuracy in cumulative surface ablation output relates to under-prediction of 18 tons of MWE for the normal CIS ice island model run (3.3 tons over-prediction with the additional AWS input), 79 tons for the traditional CIS iceberg model and only 0.77 tons for the best fit TIM. When scaled-up to represent a 10 km^2 ice island, these errors relate to 1300, 26000, 6100 and 59 tons, respectively. This depicts how inaccuracy in surface ablation prediction can result in large surface ablation errors during operational ice island deterioration modeling and why effort towards model refinement is necessary.

The TIM method of ice island surface ablation forecasting is a viable method for accurate results. The minimal variable input, in comparison to sophisticated EB models, makes it an attractive method for surface ablation modeling within a complete ice island deterioration model. However, operational modelers may continue with the EB surface ablation model for the confidence in model output under a variety of environmental conditions, especially while a method to modify DDFs during TIM forcing is established. Recursive partitioning and random forests were helpful in the interpretation of AWS data interactions on observed surface ablation,

with the validation of U_s, T_a and $K\downarrow$ being the environmental parameters to focus data collection efforts towards for accurate input to any operational model.

Table 4.1: Parameters and variables tested in surface ablation models.

Model	Variables (#)	Variables	Parameters (#)	Parameters
Regression Tree	6 (AWS data)	$Us, T_a, K\uparrow, K\downarrow,$ RH, α	N/A	N/A
CIS Iceberg	1	$K\downarrow$	3	A, Γ, ρ_i
CIS Ice island	2	T_a, U_S	17	RH, $K\downarrow$, α, T_s, ε_a ε_s, e_s, e_a, p, C_E, c_{pa}, C_S, L_v, Γ, ρ_a, ρ_i, σ
TIM	1	PDD (T_a input)	1	DDF

Table 4.2: Model hindcasts for cumulative surface ablation against observed Berghaus surface ablation. * Denotes extra AWS input, **Plus climate constants (See Table 4.1 and List of Symbols).

Model	AWS input	Environmental variables held constant	Cumulative surface ablation (cm)	Cumulative error (%)	RMSE (cm)	Source
Regression Tree	Us, Ta, $K\uparrow, K\downarrow$, RH, α		89.3	0.3	0.29	This study
CIS Iceberg	$K\downarrow$	α (0.7)	28	68	36	Kubat et al., 2007
CIS Iceberg*	$K\downarrow$	median α	41	56	28	Kubat et al., 2007
CIS Ice island	Ta, Us	RH (75%), $K\downarrow$(203.5 W m^{-2}), α (0.8) **	82.9	7.5	0.16	Ballicater, 2012
CIS Ice island*	Ta, Us, RH, $K\downarrow$,	median α	99.1	10	0.003	Ballicater, 2012
TIM	Ta (PDD)	DDF (7.3 mm)	101	12.0	0.09	Hock, 2003
TIM	Ta (PDD)	DDF (6.8)	91.0	1.9	0.06	Hock, 2003
TIM		DDF (7.3 mm), NCEP Ta (Monthly Average)	98.2	9.6	0.06	Hock, 2003

Table 4.3: Correlation coefficients (Spearman's rank) and p-values (above and below *****, respectively) of environmental variables and hourly ablation rate. Modified variable names: Kup (K↑), Kdown (K↓).

	HourlyAblation	WindSpd	Q_N	Ta	RH	Kup	Kdown	APress	Albedo
HourlyAblation	*****	0.194	0.191	0.096	0.032	-0.075	0.092	0.048	0.070
WindSpd	<0.001	*****	0.207	0.009	0.141	-0.032	0.060	-0.142	0.045
Q	<0.001	<0.001	*****	-0.036	0.139	-0.729	0.781	0.104	0.205
Ta	0.015	0.813	0.359	*****	-0.616	-0.292	0.252	-0.240	-0.140
RH	0.418	<0.001	<0.001	<0.001	*****	0.267	-0.229	0.214	0.102
Kup	0.059	0.415	<0.001	<0.001	<0.001	*****	-0.992	-0.066	0.143
Kdown	0.020	0.129	<0.001	<0.001	<0.001	<0.001	*****	0.073	-0.076
APress	0.230	<0.001	0.009	<0.001	<0.001	0.094	0.066	*****	-0.055
Albedo	0.079	0.261	<0.001	<0.001	0.010	<0.001	0.056	0.168	*****

5.0 Conclusions

Analyses of ice island deterioration within the Arctic are limited, but with the expansion of offshore industry into the region, are imperative for safe activity. Four of the five processes included in operational ice island deterioration models were considered through this thesis' research. The three processes affecting the horizontal (areal) deterioration of ice islands were addressed in Chapter 3 while Chapter 4 specifically analyzed one process contributing to change in the vertical dimension (surface ablation). Energy-balance and temperature index surface ablation models were forced with *in-situ* microclimate data from an ECA ice island in this analysis. The performance of operational models was assessed and an alternative to current surface ablation modeling is discussed.

Results presented in Chapter 3 confirmed the hypothesis that the rates and observed modes of deterioration in the Eastern and Western Canadian Arctic regions are different based on an ice island's location of origin. This is likely due to the resulting drift trajectory of ice islands sourced from these two regions and environmental conditions to which it is exposed. Air temperature and sea ice concentration were determined to be associated with ice island deterioration rate $(km^2 d^{-1})$ and LME modeling showed these variables to be significantly different between the two Canadian Arctic regions. Ice islands adrift in the ECA have a common drift trajectory south through Nares Strait, Baffin Bay and the Labrador Sea. These ice islands will come into contact with warmer air temperatures and will be exposed to a greater duration of open water conditions in comparison to ice islands located in the WCA (27% vs 2% of time over respective observation periods). Ice islands sourced from Ellesmere Island ice shelves, the common origin of ice islands adrift in this region, normally transit south and west, possibly through the CAA and ultimately into the Beaufort Sea. The possibility of re-circulation in the Beaufort Gyre causes these ice islands to stay at more northern latitudes with colder air temperatures and greater duration of

closed-pack sea ice conditions than the southern latitudes more quickly reached by ice islands adrift in the ECA. Offshore activity (natural resource exploration/extraction and ship traffic) is projected to increase in both of these areas. The re-circulation and long life-spans of ice islands in the WCA cause these ice islands to retain their hazardous potential to local offshore industry in the Beaufort and Chukchi Seas. The more numerous, larger fragments in the ECA created by fracturing and fragmentation contribute to even more individual ice hazards for operations to account for.

Use of *in-situ* microclimate data allowed for the first validation of EB and TIMs for ice islands in the Canadian Arctic (Chapter 4). The original iceberg model was not parameterized adequately to represent the magnitude of surface ablation occurring on an ice island and under-represented observed surface ablation by 68%. The more complex EB model was more adequate for representing ice island surface ablation and improved the cumulative surface ablation prediction to a 7.5% under-prediction. The inclusion of the turbulent fluxes (Q_E and Q_S) is a large benefit of the EB model since these fluxes are often the greatest contributor to Q_M. However, this is a heavily parameterized model which will be forced with environmental data estimated from the GEM model during operational CIS use. A TIM was within 10% of observed surface ablation and worked well with modeled temperature data. It is not, however, anticipated to work as well with changing albedo or other environmental or surface conditions. Further study should be completed to determine a way to modify the DDF for evolving albedo conditions throughout a melt season before this approach is adapted. Operational modelers must decide between the parsimonious TIM, which instills less confidence due to changing performance accuracy throughout a melt season, or a reliable, yet heavily parameterized, EB model.

A strength of these studies was satellite-telemetered beacon locations which aided in the acquisition of numerous satellite images for areal deterioration modeling and *in-situ* surface

ablation and microclimate data. The manuscript chapters considered both the horizontal deterioration mechanisms (wave erosion, buoyant vertical convection and fracturing) in Chapter 3 and one of the two vertical deterioration mechanisms (surface ablation) in Chapter 4. With future work, the mass balance of an ice island will be documented, filling in the gap of subsurface melt allowing for mass balance analysis.

Gaining further knowledge of ice island processes will allow for the continued improvement of operational drift and deterioration models. This will lessen the chance of an accident between an ice island and offshore activity in Canadian waters. *In-situ* data is imperative for model development and validation. Ice island fragments from 2010 and 2012 calving events of Petermann Glacier are possible sites for this research while they transit south through Baffin Bay and the Labrador Sea before reaching the Grand Banks, NL. Natural resource extraction is already underway in Newfoundland waters and it is speculated that this activity will move north along with increased ship traffic in the coming years. This thesis and future ice island research and model development will contribute to the mitigation of risk associated with a collision between an ice island and vessels or offshore equipment. This will benefit operations economically and protect the fragile and unique Arctic ecosystem.

6.0 References

Aguado, E., and Burt, J.E. 2007. Understanding Weather and Climate. Prentice Hall, New Jersey, USA.

Arcone, S.A. 2009. Glaciers and Ice Sheets. In: Jol, H.M., ed. Ground Penetrating Radar: Theory and Applications. 1st Ed. Elsvier Science, U.K.. 524 pp.

Arendt, A., and Sharp, M. 1999. Energy balance measurements on a Canadian high arctic glacier and their implications for mass balance modeling. In: Tranter, M. et al., eds. Interactions Between the Cryosphere, Climate and Greenhouse Gases. Proceedings of the IUGG Symposium, Birmingham 1999. IAHS Publ, no. 256:165-172. 86 pp.

Arnold, N.S., Willis, I.C., Sharp, M.J., Richards, K.S., and Lawson, W.J. 1996. A distributed surface energy-balance model for a small valley glacier. I. Development and testing for Haut Glacier d'Arolla, Valais, Switzerland. Journal of Glaciology 42(141):77-89.

Ballicater Consulting Ltd. 2012. Ice Island and Iceberg Studies 2012. Report prepared for the Canadian Ice Service, Environment Canada. Report 12-01. 51 pp.

Bamler, R., and Hartl, P. 1998. Synthetic aperture radar interferometry. Inverse Problems 14: R1-R54.

Barrette, P. 2011. Offshore pipeline protection against seabed gouging by ice: An overview. Cold Regions Science and Technology 69:3-20.

Belkin, I.M., and Sergey, A.K. Forthcoming. Russian drifting stations on Arctic ice islands. In: Copland, L., and Mueller, D., eds. Arctic Ice Shelves and Ice Islands. Springer: in preparation.

Bogorodsky, V.V., Bentley, C.R., and Gudmandsen, P.E. 1985. *Radioglaciology*. Boston: D. Reidel Publishing Co. 272 pp.

Bradford, J.H., Nichols, J., Mikesell, T.D., and Harper, J.T. 2009. Continuous profiles of electromagnetic wave velocity and water content in glaciers: an example from Bench Glacier, Alaska, USA. Annals of Glaciology 50:1-9.

Braithwaite, R.J. 1995. Positive degree-day factores for ablation on the Greenland Ice Sheet studied by energy-balance modeling. Journal of Glaciology 41(137):153-160.

Braithwaite, R.J., and Olesen, O.B. 1993. Seasonal variation of ice ablation at the margin of the Greenland ice sheet and its sensitivity to climate change, Qamanârssûp sermia, West Greenland. Journal of Glaciology 39(132):267-274.

Breiman, L., and Cutler, A. 2008. Random forests – Regression description. Accessed June 2013. <http://www.stat.berkeley.edu/~breiman/RandomForests/reg_papers.htm>

Brock, B. 2006. EB_INFO: Instructions for using the EB_AUTO spreadsheet energy balance model. University of Dundee. Accessed August 2012. <http://www.dundee.ac.uk/geography/research/resources/ebautoinstructions/ >

Brock, B.W., and Arnold, N.S. 2000. A spreadsheet-based (Microsoft Excel) point surface energy balance model for glacier and snow melt studies. Earth Surface Processes and Landforms 25:649-658.

Campbell Scientific. 2010. SR50A Sonic ranging sensor - Instruction manual. Campbell Scientific Canada Corp., Edmonton, AB. 59 pp.

Comiso, J.C. 2012. Large decadal decline of the Arctic multiyear ice cover. Journal of Climate 25:1176-1193, doi:10.1175/JCLI-D-11-00113.1.

Copland, L., Mueller, D.R., and Weir, L. 2007. Rapid loss of the Ayles Ice Shelf, Ellesmere Island, Canada. Geophysical Research Letters. doi:10.1029/2007GL031809.

Crawford, A.J. 2012. Personal field work. Clyde River, NU.

Crawley, M.J. 2007. The R Book. 1st ed. Sussex, UK: John Wiley & Sons, Inc. 254 pp.

Crocker, G., Carrieres, T., and Tran, H. 2013. Ice island drift and deterioration forecasting in eastern Canada. Proceedings of the 22nd International Conference on Port and Ocean Engineering under Arctic Conditions held 9-13 June in Espoo, Finland. POAC13-166.

Derksen, C., Smith, S.L., Sharp, M., Brown, L., Howell, S., Copland, L., Mueller, D.R. et al. 2012. Variability and change in the Canadian cryosphere. Climatic Change. doi :10.1007/s10584-012-0470-0.

De Abreu, R., Arkett, M., Cheng, A., Zagon, T., Mueller, D., Vachon, P.W., and Wolfe, J. 2011. RADARSAT-2 Mode Selection for Maritime Surveillance. External client report DRDC Ottawa ECR 2011 - prepared by the Canadian Ice Service for Environment Canada and Defence Research and Development Canada. 50 pp.

Environment Canada (2012a) Archive Search v1.0. Accessed on 12 March 2013. <http://dynaweb.cis.ec.gc.ca/Archive10/?lang=en>

Environment Canada (2012b) Petermann Glacier Ice Island 2012. Government of Canada. Accessed on 15 June 2013. <http://www.ec.gc.ca/default.asp?lang=En&n=592AB94B-1&news=63B51150-B0B0-438F-94CA-A1CDDFA86A25>

ESA. 2013. Radar Course III. (c) 2001-2013. Accessed on 16 July 2013. <http://earth.esa.int/applications/data_util/SARDOCS/spaceborne/Radar_Courses/>

Esbensen, S.K., and Reynolds, R.W. 1981. Estimating monthly averaged air-sea transfers of heat and momentum using the bulk aerodynamic method. Journal of Physical Oceaonography 11(4):457-465.

Falkner, K.K., Melling, H., Münchow, A.M., Box, J., Wohlleben, T., Johnson, H.L., and Gudmandsen P. 2011. Context for the recent massive Petermann Glacier Calving Event. Eos 92(14):117-124.

Fletcher, J.O. 1968. Origin and early utilization of aircraft-supported drifting stations. In: Arctic Drifting Stations, Coordinated by J.E. Slater. Proceedings of the Arctic Institute of North America Symposium held 12-15 April 1966 in Virginia. 475 pp.

Forrest, A.L., Hamilton, A.K., Schmidt, V., Laval, B.E., Mueller, D., Crawford, A., Brucker, S., and Hamilton, T. 2012. Digital terrain mapping of Petermann Ice Island fragments Canadian High Arctic. Proceedings of the 21st International Symposium on Ice held 11-15 June in Dalin, China.

Ghilani, C.D. 2000. Demystifying area uncertainty: more or less. Surveying and Land Information Systems 60:177-182.

Halliday, E.J., King, T., Bobby, P., Copland, L., and Mueller, D. 2012. Petermann Ice Island 'A' survey results, offshore Labrador. Arctic Technology Conference held 3-5 Dec 2012 in Houston, Texas. OTC 23714.

Harsem, O., Eide, A., and Heen, K. 2011. Factors influencing future oil and gas prospects in the Arctic. Energy Policy 39:8037-804.

Hay, J.E., Fitzharris, B.B. 1988. A comparison of the energy-balance and bulk-aerodynamic approaches for estimating glacial melt. Journal of Glaciology 34(117):145-153.

Higgins, A.K. 1991. North Greenland glacier velocities and calf ice production. Polarforschung 60:1-23.

Hock, R. 1999. A distributed temperature-index ice and snowmelt model including potential direct solar radiation. Journal of Glaciology 45(149):101-111.

Hock, R. 2003. Temperature index melt modeling in mountain areas. Journal of Hydrology 282:104-115

Hock, R. and Tijm-Reijmer, C. 2012. A mass-balance, glacier runoff and mutli-layer snow model. Program documentation and users manual. University of Alaska Fairbanks and Utrecht University, The Netherlands. Vers. 27, 88 pp.

Hoffman, M.J., Fountain, A.G., and Achuff, J.M. 2007. 20th-century variations in area of cirque glaciers and glacierets, Rocky Mountain National Park, Rocky Mountains, Colorado, USA. Annals of Glaciology 47:349-354.

Hsu, S.A., Meindl, E.A., and Gilhousen, D.B. 1994. Determining the power-law wind-profile exponent under near-neutral stability conditions at sea. Journal of Applied Meteorology 33:757-765.

Huybrechts, P., Letréguilly, A., Reeh, N. 1991. The Greenland ice sheet and greenhouse warming. Palaeogeography, Palaeoclimatololgy, and Palaeoecology 89(4): 399-412.

IPCC (Intergovenmental Panel on Climate Change). 2001. Climate Change 2000 - Third Assessment Report. Cambridge University Press, Cambridge.

Irvine-Fynn, T.D.L., Moorman, B.J., Williams, J.L.M., and Walter, F.S.A. 2006. Seasonal changes in ground-penetrating radar signature observed at a polythermal glacier, Bylot Island, Canada. Earth Surfaces Processes and Landforms 31: 892-909.

Jeffries, M.O. 1986. Ice island calvings and ice shelf changes, Milne Ice Shelf and Ayles Ice Shelf, Ellesmere Island, N.W.T. Arctic 39:15-19.

Jeffries, M.O. 1992a. Arctic ice shelves and ice islands: origin, growth and disintegration, physical characteristcs, structural-stratigraphic variability, and dynamics. Reviews of Geophysics 30:245-267.

Jeffries, M.O. 1992b. The source and calving of ice island ARLIS-II. Polar Record 28(165):137-144.

Jeffries, M.O. 2002. Glaciers of the Arctic Islands – Ellesmere Island ice shelves and ice islands. In: Williams, E.S., and Ferrigno, J.G., eds. Satellite image atlas of glaciers of the world - U.S. Geological Survey professional paper. 1386-J-1.

Jeffries, M.O., and Sackinger, W.M. 1987. Remote sensing of sea-ice growth and melt-pool evolution, Milne Ice Shelf, Ellesmere Island, Canada. Annals of Glaciology 9:145-150.

Jeffries, M.O., Sackinger, W.M., and Shoemaker, H.D. 1987. Geometry and physical properties of ice islands. Proceedings of the 9th International Conference on Port and Ocean Engineering Under Arctic Conditions held 17-21 August in Fairbanks, Alaska. 1:69-83.

Jeffries, M.O., and Sackinger, W.M. 1990. Ice island detection and characterization with airborne synthetic aperture radar. Journal of Geophysical Research 95:5371-5377.

Jeffries, M.O., and Shaw, A.M. 1993. The drift of ice islands from the Arctic Ocean into the Channels of the Canadian Arctic Archipelago: the history of Hobson's Choice Ice Island. Polar Record 29(171):305-312.

Johannessen, O.M., Babiker, M., and Miles, M.W. 2011. Petermann Glacier, North Greenland: massive calving in 2010 and the past half century. The Cryosphere Discussions 5:169-181, doi:10.5194/tcd-5-169-2011.

Kalnay, E. et al, 1996. The NCEP/NCAR 40-year Reanalysis Project. Bulletin of the American Meteorological Society 77(3): 437-471.

Knox, S. 2011. Snow surface energy exchanges and snowmelt in a shrub-covered bog in Eastern Ontario, Canada. MSc Thesis, Department of Geography and Environmental Studies, Carleton University, Ottawa, Ontario. 134 pp.

Knox, S., Carey, S.K., and Humphreys, E.R. 2012. Snow surface energy exchanges and snowmelt in a shrub-covered bog in eastern Ontario, Canada. Hydrological Processes 26:1877-1891, doi: 10.1002/hyp.9289.

Koenig, L.S., Greenaway, K.R., Dunbar, M., and Hattersley-Smith, G. 1952. Arctic ice islands. Arctic 5:67-103.

Krajick, K. 2001. Tracking icebergs for clues to climate change. Science 292:2244-2245.

Kubat, I., Sayed, M., Savage, S.B., and Carrieres, T. 2005. An operational model of iceberg drift. Proceedings of the 15th International Offshore and Polar Engineering Conference held 19-24 June in Seoul, Korea. 1:125-131.

Kubat, I., Sayed, M., Savage, S.B., Carrieres, T., and Crocker, G. 2007. An Operational Iceberg Deterioration Model. Proceedings of the 17th International Offshore and Polar Engineering Conference held 1-6 July in Lisbon, Portugal. 1:652 – 657.

Labey, K., St. Pierre, H., Sundsten, J., and Seaman, O. 2009. Combining GPR and historical aerial photographs to investigate river channel morphodynamics, Oldman River, southern Alberta. Lethbridge Undergraduate Research Journal 3(2).

Lindsay, R.W. 1998. Temporal variability of the energy balance of thick Arctic pack ice. Journal of Climate 11:313-333.

Lougeay, R. 1974. Detection of buried glacial and ground ice with thermal infrared remote sensing. In: Advanced concepts and techniques in the study of snow and ice resources: an interdisciplinary symposium. The National Academy of Sciences. Symposium held 2-6 December in Monterey, CA, USA. 487-493 pp.

Lindsay, R.W. 1998. Temporal variability of the energy balance of thick Arctic pack ice. Journal of Climate 11:313-333.

MacAyeal, D.R., Okal, E.A., Aster, R.C., Bassis, J.N., Brunt, K.M., Cathles, L.M., Drucker, R., et al. 2006. Transoceanic wave propogation links iceberg calving margins of Antarctica with storms in tropics and Northern Hemisphere. Geophysical Research Letters 33, L17502, doi:10.1029/2006GL027235.

Male, D.H., and Gray, D.M. 1981. Snowcover ablation and runoff. In: Gray, D.M., and Male, D.H., eds. Handbook of snow: principles, processes, management and use. Pergamon Press, Toronto: pp 360-436.

MANICE. 2005. Manual of Standard Procedures for Observing and Reporting Ice Conditions. Revised 9th ed. Meteorological Service of Canada – Canadian Ice Service, Ottawa, ON.

Marcus, M.G., Moore, R.D., and Owens, I.F. 1985. Short-term estimates of surface energy transfers and ablation on the lower Franz Josef Glacier, South Westland, New Zealand. New Zealand Journal of Geology and Geophysics 28(3): 559-567.

McGonigal, D., Hagen, D., and Guzman, L. 2011. Extreme ice features distribution in the Canadian Arctic. Proceedings of the 20th International Conference on Port and Ocean Engineering under Arctic Conditions held 11-14 July in Montéal, Quebec. POAC 11-045.

McKenna, R.F. 2005. Refinement of iceberg shape input to the CIS forecast model. Richard McKenna report 04-09-01 to Canadian Ice Service, Environment Canada. Ottawa, Ontario. 10 pp.

MDA (MacDonald, Dettwiler and Associates Ltd.). 2009. RADARSAT-2 - Product Details. Document RN-SP-52-1238 RS2. 12 pp.

Merkle, E.C., and Shaffer, V.A. 2011. Binary recursive partitioning : Background, methods, and application to psychology. British Journal of Mathmatical and Statistical Psychology 62 :161-181.

Mortimer, C.A., Copland, L., and Mueller, D.R. 2012. Volume and area changes of the Milne Ice Shelf, Ellesmere Island, Nunavut, Canada, since 1950. Journal of Geophysical Research 117, F04011, doi:10.1029/2011F002074.

Mott, H. 2007. Remote Sensing with Polarimetric Radar. John Wiley & Sons, Inc. Hoboken, New Jersey, USA. 309 pp.

Mueller, D.R. Forthcoming. Ice shelf chapter. In: Copland, L., and Mueller, D., eds. *Arctic Ice Shelves and Ice Islands*. Springer: in preparation.

Mueller, D.R. Copland, L., Hamilton, A., and Stern, D. 2008. Examining Arctic ice shelves prior to the 2008 breakup. Eos 89(49):502-503.

Mueller, D., Crawford, A., Copland, L., and VanWychen, W. 2013. Ice island and iceberg fluxes from Canadian High Arctic sources. Report prepared for the Northern Transportation Assessment Initiative, Innovation Policy Branch, Transport Canada. Ottawa, Ontario. 22 pp.

Mueller, D.R., Vincent, W.F., and Jeffries, M.O. 2006. Environmental gradients, fragmented habitats, and microbiota of a northern ice shelf cryoecosystem, Ellesmere Island, Canada. Arctic, Antarctic and Alpine Research 38(4): 593-607.

Mueller, D.R., and Wohlleben, T. 2010. Beacon Deployment Report. Canadian Ice Service, Environment Canada. Ottawa, Ontario.

Munro, D.S. 1989. Surface roughness and bulk heat transfer on a glacier: comparison with eddy correlation. Journal of Glaciology 35(121):343-348.

Murphy, D.L., and Carrieres, T. 2010. CIS-IIP iceberg model inter-comparison. Report prepared for the North American Ice Service. 27 pp.

NASA. 2012. Earth Observatory - More ice breaks off the Petermann Glacier: Natural hazards. Accessed on 14 February 2013. <http://earthobservatory.nasa.gov/NaturalHazards/view.php?id=78556>

NCEP/NCAR. 2013a. NCEP/NCAR air temperature (surface) reanalysis. NOAA Earth Systems Research Laboratory - Physical Sciences Division. Accessed on 3 May 2013. <http://www.esrl.noaa.gov/ >

NCEP/NCAR. 2013b. NCEP/NCAR sea surface temperature reanalyis. NOAA Earth Systems Research Laboratory - Physical Sciences Division. Accessed on 3 May 2013. <http://www.esrl.noaa.gov/ >

Newell, J.P. 1993. Exceptionally large icebergs and ice islands in Eastern Canadian Waters: A review of sightings from 1900 to present. Arctic 46:205-211.

NSIDC. 2012. Arctic sea ice shatters previous low records; Antarctic sea ice edges to record high. National Snow and Ice Data Center press release: 2 Oct 2012. Accessed on 12 Oct 2012. <http://nsidc.org/news/press/20121002_MinimumPR.html.>

Oerlemans, J. 2001. Glaciers and Climate Change. Taylor and Francis, NY, USA.

Oerlemans, J., Björnsson, H., Kuhn, M., Obleitner, F., Palsson, F., Smeets, C.J.P.P., Vugts, H.F., and De Wolde, J. 1999. Glacio-meteorological investigationson Vatnajökull, Iceland, Summer 1996: an overview. Boundary-Layer Meteorology 92:3-26.

Oerlemans, J., and Grisogono, B. 2002. Glacier winds and parameterization of the related surface heat fluxes. Tellus 54(A):440-452.

Ohmura, A. 2001. Physical basis for the temperature-based melt-index method. Journal of Applied Meteorology 40:753-761.

Oke, T.R. 1987. Boundary Layer Climates. 2nd ed. Routledge, New York. 435 pp.

Park, J.W., Gourmelen, N., Shepherd, A., Kim, S.W., Vaughan, D.G., and Wingham, D.J. 2013. Sustained retreat of the Pine Island Glacier. Geophysical Research Letters 40:2137-2142, doi:10.1002/grl.50379.

Pellicciotti, F., Carenzo, M., Helbing, J., Rimkus, S., and Burlando, P. 2009. On the role of subsurface heat conduction in glacier energy-balance modelling. Annals of Glaciology 50:16-24.

Peterson, I.K. 2005. Large tabular icebergs and ice islands off Eastern Canada in 2001-2003 and their probable source. Proceedings of the 18th International Conference on Port and Ocean Engineering under Arctic Conditions held 26-30 July in Potsdam, New York. 1:143-152.

Peterson, I.K. 2011. Ice island occurrence on the Canadian East Coast. Proceedings of the International Conference on Port and Ocean Engineering under Arctic Conditions. Held 10-14 July in Montréal, Canada. POAC11-044.

Peterson, I.K., Prinsenberg S.J., Pittman, M., and Desjardins, L. 2009. The drift of an exceptionally large ice island from the Petermann Glacier in 2008. Proceedings of the 20th International Conference on Port and Ocean Engineering under Arctic Conditions held 9-12 June in Luleå, Sweden. POAC09-130.

Pinheiro, J.C., and Bates, D.M. 2000. Mixed-Effects Models in S and S-PLUS. 1st ed. NY, USA: Springer Verlag. 528 pp.

Pope, S.G. 2010. Changes in Multiyear Landfast Sea Ice in the Northern Canadian Arctic Archipelago. MSc Thesis, Department of Geography, University of Ottawa, Ottawa, Ontario. 84 pp.

Prowse, T.D., Furgal, C., Choulnard, R., Mulling, H., Milburn, D., and Smith, S.L. 2009. Implications of climate change for economic development in Northern Canada: Energy, Resource, and Transportation Sectors. Ambio 38:272-28.

Rignot, E., and Steffen, K. 2008. Channelized bottom melting and stability of floating ice shelves. Geophysical Research Letters doi:10.1029/2007GL031765.

Robe, R., Maier, D., and Kollmeyer, R. 1977. Iceberg deterioration. Nature 267:505-506.

Robeson, S.M., and Shein, K.A. 1997. Spatial coherence and decay of wind speeds and power in the north-central United States. Physical Geography 18(6): 479-495, doi:10.1080/02723646.1997.10642631.

Rudkin, P., King, T., Ralph, F., and Stoermer, S.A. 2005. Investigations into the increased sightings of ice islands in the North Atlantic. Proceedings of the 18th International Conference on Port and Ocean Engineering Under Arctic Conditions held 26-30 June in Potsdam, NY. 2:605-614.

Sackinger, W.M., Jeffries, M.O., Li, F., and Lu, M. 1991. Ice island creation, drift, recurrences, mechanical properties, and interactions with Arctic offshore oil production structures. Final report prepared for the US Dept of Energy. Contract No: DE-FG21-88MC25027.

Sackinger, W.M., Shoemaker, H.D., Serson, H., Jeffries, M.O., Yan, M. 1985. Ice islands as hazards to Arctic offshore production strucutres. Proceedings of 17th Annual Offshore Technology Conference. Houston, TX. OTC 4943.

Savage, S.B. 2001. Aspects of iceberg drift and deterioration. In: Balmforth, N.J., and Provenzale, A., eds. Geomophological Fluid Mechanics, Springer Verlag Press, Berlin. 279-318 pp.

Scambos, T., Hulbe, C., and Fahnestock, M. 2003. Climate-induced ice shelf disintegration in the Antarctic Peninsula. Antarctic Research Series 76:335-347.

Scambos, T., Sergienko, O., Sargent, A., MacAyeal, D., Fastook, J. 2005. ICESat profiles of tabular iceberg margins and iceberg breakup at low latitudes. Geophysical Research Letters doi:10.1029/2005GL023802.

Scambos, T., Fricker, H.A., Liu, C.C., Bohlander, J., Fastook, J., Sargent, A., Massom, R., and Wu, A.M. 2009. Ice shelf disintegration by plate bending and hydro-fracture: Satellite observations and model results of the 2008 Wilkins ice shelf break-ups. Earth and Planetary Science Letters 280:51-60.

Scambos, T., Ross, R., Bauer, R., Yermolin, Y., Skvarca, P., Long, D., Bohlander, J., and Haran, T. 2008. Calving and ice-shelf break-up processes investigated by proxy: Antarctic tabular iceberg evolution during northward drift. Journal of Glaciology 54:579 – 591.

Stephenson, S.R., Smith, L.C., Brigham, L.W., and Agnew, J.W. 2013. Projected 21st-century changes to Arctic marine access. Climatic Change. DOI:10.1007/s10584-D12-0685-D.

Strobl, C., Malley, J., and Tutz, G. 2009. An introduction to recursive partitioning: rationale, application and characteristics of classification and regression trees, bagging and random forests. Psychologyical Methods 14(4):323-348.

Stroeve, J., Serreze, M., Drobot, S., Gearheard, S., Holland, M., Maslanik, J., Meier, W., and Scambos, T. 2008. Arctic sea ice extent plummets in 2007. Eos 89(2):13-20.

Squire, V.A, and Dugan, J.P. 1995. Of ocean waves and sea ice. Annual Review of Fluid Mechanics 27:115-168.

Tang, C.C.L., Ross, C.K., Yao, T., Petrie, B., DeTracey, B.M., and Dunlap, E. 2004. The circulation, water masses and sea-ice of Baffin Bay. Report of the Bedford Institute of Oceanography prepared for Fisheries and Oceans Canada, Dartmouth, Nova Scotia. 16 pp.

Taylor, J.R. 1982. An Introduction to Error Analysis. 2nd ed. University Science Books2[nd] ed. Sausalito, CA., USA. 327 pp.

Therneau, T., Atkinson, B., and Ripley, B. 2013. Recursive Partitioning - Package: Rpart. Accessed on 2 June 2013. <http://cran.r-project.org/web/packages/rpart/rpart.pdf>

Trenberth, K.E., Soden, B., Rusticucci, M., Renwick, J.A., Rahimzadeh, F., Parker, D., Klein Tank, A., Easterling, D., Zhai, P., Jones, P.D., Ambenje, P. et al. 2007. Observations: surface and atmospheric climate change. In: Solomon, S. Qin, D., Manning, M, Chen, Z., Marquis, M., Averyt, K.B., Tignor A., and Change, H.L., eds. Climate change 2007: The Physical Science Basis. Contribution of Working Group I to the Fourth Assessment Report of the Intergovernmental Panel on Climate Change. Cambridge University Press, New York, NY.

Tuoma, J.S. 1977. Dependence of the wind profile power law on the stability of various locations. Journal of Air Pollution Control Association 27(9): 863-866.

UNOOSA (2013) Radarsat-2, Technology Guide. Accessed on 8 August 2013. <http://www.un-spider.org/technology-guides/radarsat-2>

Valsson, T., and Ulfarsson, G.F. 2011. Future changes in activity structures of the globe under a receding Arctic ice scenario. Futures 42:450-459.

van der Sanden, J.J., and Drouin, H. 2011. Polarimetric RADARSAT-2 for river freeze-up monitoring; preliminary results. Proceedings of the 5th International Workshop on Science and Application of SAR Polarimetry and Polarimetric Interferometry held 24-28 Jan 2011 in Frascati, Italy. SP-695.

VanWychen, W., and Copland, L. Forthcoming. Ice island drift mechanisms in the Canadian High Arctic. In: Copland, L., and Mueller, D., eds. Arctic Ice Shelves and Ice Islands. Springer: in preparation.

Veitch, B., Williams, M., Gardner, A., and Liang, B. 2001. Field Observations of Iceberg Deterioration. Report 20-64 prepared for the CHC/National Research Council by Ocean Engineering Research Centre, Memorial University, St. John's, Newfoundland. 108 pp.

Vincent, W.F., Whyte, L.G., Lovejoy, C., Greer, C.W., Laurion, I., Suttle, C.A., Corbeil, J., and Mueller, D.R. 2009. Arctic microbial ecosystems and impacts of extreme warming during the International Polar Year. Polar Science 3:171-180.

White, A. 2012. Dynamics and historical changes of the Petersen Ice Shelf and Epishelf Lake, Nunavut, Canada, since 1959. MSc Thesis, Department of Geography, University of Ottawa, Ottawa, Ontario. 103 pp.

White, F.M., Spaulding, M.L., and Gominho, L. 1980. Theoretical estimates of the various mechanisms involved in iceberg deterioration in the open ocean environment. Report prepared for the U.S. Coast Guard, No. CG-D-62-80, 126 pp.

Woodward, J., and Burke, M.J. 2007. Applications of ground-penetrating radar to glacial and frozen materials. Journal of Environmental and Engineering Geophysics. 12(1), 69–85.

Appendix A: RADARSAT-2 imagery used to quantify ice island surface area deterioration.

Ice island	Beam mode	Date	Time (UTC) (hhmmss)	Resolution (m)
PII-B	Fine-quad	7-Sep-11	213824	8
	ScanSAR Wide	13-Sep-11	220200	320
	Fine-quad	24-Sep-11	214236	8
	Fine-quad	28-Sep-11	212557	8
	Fine-quad	8-Oct-11	213417	8
	Fine-quad	23-Oct-11	110315	8
	Fine-quad	1-Nov-11	213417	8
	ScanSAR Wide	10-Nov-11	103700	320
	ScanSAR Wide	16-Nov-11	110200	320
	ScanSAR Wide	20-Nov-11	104500	320
	Fine-quad	18-Jan-12	215918	8
	Fine-quad	28-Feb-12	220328	8
	ScanSAR Wide	12-Apr-12	104500	320
	Fine-quad	14-Jun-12	214237	8
	ScanSAR Wide	3-Jul-12	105400	320
	Fine-quad	1-Aug-12	214237	8
	ScanSAR Wide	27-Aug-12	105000	320
	ScanSAR Wide	2-Sep-12	111400	320
	ScanSAR Wide	9-Sep-12	111000	320
	ScanSAR Wide	16-Sep-12	110600	320
	ScanSAR Wide	26-Sep-12	110200	320
	ScanSAR Wide	14-Oct-12	105000	320
	Fine-quad	29-Oct-12	214643	8
	ScanSAR Wide	21-Jan-13	110200	320
	Fine-quad	8-Apr-13	215038	8
	Fine-quad	29-Jun-13	215859	8
PII-B-a	Fine-quad	12-Sep-11	223421	8
	Fine-quad	22-Sep-11	224233	8
	Fine-quad	22-Sep-11	224229	8
	Fine-quad	6-Oct-11	123834	8
	ScanSAR Wide	14-Nov-11	134000	320
	Fine-quad	28-Feb-12	234535	8
	Fine-quad	14-Jun-12	132838	8
	ScanSAR Wide	31-Aug-12	121300	320
	ScanSAR Wide	8-Sep-12	113900	320
	ScanSAR Wide	6-Nov-12	111900	320
	ScanSAR Wide	12-Nov-12	114400	320
	Fine-quad	26-Mar-13	113600	8
	Fine-quad	2-Jul-13	22120	8

WH-1	Wide	7-May-09	230053	14
	Fine-quad	15-Sep-09	142128	8
	Fine-quad	16-Sep-09	153224	8
	Fine-quad	8-Oct-09	230910	8
	Fine-quad	9-Oct-09	142144	8
	Fine-quad	11-Oct-09	232140	8
	Fine-quad	3-Nov-09	235052	8
	Fine-quad	4-Nov-09	232139	8
	ScanSAR Narrow	1-Dec-09	000308	80
	ScanSAR Wide	6-Dec-09	142900	160
	Fine-quad	8-Jan-10	150735	8
	Fine-quad	10-Jan-10	140909	8
	Fine-quad	29-Jan-10	231321	8
	Fine-quad	30-Jan-10	224410	8
	Fine-quad	31-Jan-10	002422	8
	Fine-quad	6-Mar-10	003247	8
	Fine-quad	8-Mar-10	230501	8
	Fine-quad	11-Mar-10	231732	8
	Fine-quad	29-Mar-10	225233	8
WH-2	Wide	7-May-09	230053	14
	Fine-quad	24-Sep-09	231739	8
	Fine-quad	27-Sep-09	233011	8
	Fine-quad	22-Oct-09	230056	8
	Fine-quad	24-Oct-09	234240	8
	Fine-quad	25-Oct-09	145455	8
	Fine-quad	12-Nov-09	224825	8
	Fine-quad	14-Nov-09	233009	8
	Ultra-fine	24-Nov-09	151952	3
	Fine-quad	25-Dec-09	151534	8
	Fine-quad	26-Dec-09	144623	8
	Fine-quad	21-Jan-10	220649	8
	Fine-quad	22-Jan-10	231744	8
	Fine-quad	23-Jan-10	224830	8
	Fine-quad	19-Mar-10	224425	8
	Fine-quad	30-Apr-10	235937	8
	Fine-quad	26-May-10	144227	8
	Fine-quad	29-Jun-10	230925	8
	Fine-quad	20-Jul-10	225656	8
	Fine-quad	11-Sep-10	235048	8
	Fine-quad	27-Oct-10	145142	8
	Fine-quad	16-Jan-11	134918	8
	Fine-quad	16-Mar-11	232513	8

M-1&2	Wide	7-May-09	230053	14
	Scan-SAR Wide	31-May-09	144101	160
	Fine	27-Aug-09	233430	8
	Scan-SAR Wide	18-Sep-09	225153	160
	Fine-quad	16-Oct-09	223606	8
	Fine-quad	18-Oct-09	231750	8
	Fine-quad	6-Nov-09	222334	8
	Fine-quad	8-Nov-09	230517	8
	Fine-quad	9-Nov-09	141711	8
	Fine-quad	29-Nov-09	225252	8
	Fine-quad	30-Nov-09	222340	8
	Fine-quad	16-Jan-10	143338	8
	Fine-quad	18-Jan-10	151522	8
	Fine-quad	18-Feb-10	215022	8
	Fine-quad	19-Feb-10	144154	8
	Wide	2-Mar-10	224018	14
M3	Fine-quad	22-Oct-09	320056	8
	Fine-quad	24-Oct-09	234240	8
	Fine-quad	25-Oct -09	145455	8
	Fine-quad	12-Nov-09	224825	8
	Fine-quad	14-Nov-09	233009	8
	Fine-quad	24-Nov-09	151952	8
	Fine-quad	7-May-10	235524	8
	Fine-quad	8-May-10	232610	8
	Fine-quad	1-Jun-10	232609	8
	Fine-quad	11-Sept-10	235036	8
	Fine-quad	1-Mar-11	003140	8
	Fine-quad	12-May-11	003142	8

Appendix B: Details of area and mass decreases, corresponding deterioration mode and recorded sea ice concentration at time of RADARSAT-2 image acquisition.

Ice island	Date	Days between images	Surface area (km^2)	Areal rate decrease (km^2 d^{-1})	Mass (Gt)	Sea ice concentration (tenths)	Deterioration Mode
PII-B-a	12-Sep-11		14.214		1.0	0.2	
PII-B-a	15-Sep-11	3	12.745	0.49	0.90	0.2	Fracture
PII-B-a	22-Sep-11	7	12.555	0.03	0.88	0.2	Decay
PII-B-a	22-Sep-11	0	12.269	0.00	0.86	0.2	Decay
PII-B-a	06-Oct-11	14	11.734	0.04	0.83	0.2	Decay
PII-B-a	14-Nov-11	39	11.81	0.00	0.83	9.7	Decay
PII-B-a	28-Feb-12	145	11.586	0.00	0.82	9.9	Decay
PII-B-a	14-Jun-12	107	11.503	0.00	0.75	10	Decay
PII-B-a	31-Aug-12	78	11.57	0.00	0.69	0.2	Decay
PII-B-a	08-Sep-12	8	11.5	0.01	0.65	0.2	Decay
PII-B-a	06-Nov-12	59	8.39	0.05	0.47	0.2	Decay
PII-B-a	12-Nov-12	6	8.45	-0.01	0.48	9.7	Addition
PII-B-a	26-Mar-13	134	8.54	0.00	0.48	10	Decay
PII-B-a	02-Jul-13	98	8.36	0.00	0.47	10	Decay

Ice island	Date	Days between images	Surface area (km^2)	Areal rate decrease (km^2 d^{-1})	Mass (Gt)	Sea ice concentration (tenths)	Deterioration Mode
PII-B	07-Sep-11		69.81		4.77	0.2	
PII-B	13-Sep-11	6	69.77	0.01	4.77	0.2	Decay
PII-B	24-Sep-11	17	63.40	0.37	4.33	0.2	Fracture
PII-B	28-Sep-11	4	62.67	0.18	4.28	0.2	Fragmentation
PII-B	08-Oct-11	10	61.64	0.10	4.21	0.2	Fragmentation
PII-B	23-Oct-11	15	60.04	0.11	4.10	0.2	Fragmentation
PII-B	01-Nov-11	9	59.65	0.04	4.08	0.2	Decay
PII-B	10-Nov-11	9	59.44	0.02	4.06	8	Decay
PII-B	16-Nov-11	6	41.84	2.93	2.86	9	Fracture
PII-B	20-Nov-11	4	42.22	-0.09	2.89	9	Addition
PII-B	18-Jan-12	78	39.78	0.03	2.72	9.7	Fracture
PII-B	28-Feb-12	41	39.87	0.00	2.73	10	Addition
PII-B	12-Apr-12	44	39.84	0.00	2.72	10	Decay
PII-B	14-Jun-12	107	39.26	0.01	2.68	10	Decay
PII-B	03-Jul-12	19	40.73	-0.08	2.36	10	Addition
PII-B	01-Aug-12	48	37.94	0.06	2.06	0.2	Decay
PII-B	27-Aug-12	26	37.49	0.02	1.97	0.2	Decay
PII-B	02-Sep-12	6	30.21	1.21	1.57	0.2	Fracture
PII-B	09-Sep-12	7	29.13	0.15	1.50	0.2	Fragmentation
PII-B	16-Sep-12	7	29.12	0.00	1.48	0.2	Decay
PII-B	26-Sep-12	10	27.22	0.19	1.37	0.2	Fracture
PII-B	14-Oct-12	18	24.26	0.16	1.66	0.2	Fracture
PII-B	29-Oct-12	89	20.56	0.04	1.41	0.2	Decay
PII-B	21-Jan-13	84	10.29	0.12	0.70	10	Fracture
PII-B	08-Apr-13	77	11.8	-0.02	0.78	10	Addition
PII-B	28-Jun-13	82	11.84	-0.00	0.80	10	Addition

Ice island	Date	Days between images	Surface area (km^2)	Areal rate decrease (km^2 d^{-1})	Sea ice concentration (tenths)	Deterioration Mode
WH1	07-May-09		9.86	0	9.7	Decay
WH1	15-Sep-09	131	9.86	0.00	9.7	Decay
WH1	16-Sep-09	1	9.86	0.00	9.7	Decay
WH1	08-Oct-09	22	9.86	0.00	9.7	Decay
WH1	09-Oct-09	1	9.86	0.00	9.7	Decay
WH1	11-Oct-09	2	9.86	0.00	9.7	Decay
WH1	03-Nov-09	23	9.86	0.00	9.7	Decay
WH1	04-Nov-09	1	9.86	0.00	9.7	Decay
WH1	01-Dec-09	27	7.82	0.08	9.7	Decay
WH1	06-Dec-09	5	6.76	0.21	9.7	Fracture
WH1	08-Jan-10	33	6.36	0.01	10	Decay
WH1	10-Jan-10	2	6.36	0.00	10	Decay
WH1	29-Jan-10	19	6.36	0.00	10	Decay
WH1	30-Jan-10	1	6.36	0.00	10	Decay
WH1	31-Jan-10	1	6.36	0.00	10	Decay
WH1	06-Mar-10	34	6.36	0.00	10	Decay
WH1	08-Mar-10	2	6.36	0.00	10	Decay
WH1	11-Mar-10	3	6.36	0.00	10	Decay
WH1	29-Mar-10	18	6.36	0.00	10	Decay

Ice island	Date	Days between images	Surface area (km^2)	Areal rate decrease (km^2 d^{-1})	Sea ice concentration (tenths)	Deterioration Mode
WH2	07-May-09		6.77		9.7	
WH2	24-Sep-09	140	6.77	0.00	9.7	Decay
WH2	27-Sep-09	3	6.70	0.97	9.7	Fracture
WH2	22-Oct-09	25	6.70	0.00	10	Decay
WH2	24-Oct-09	2	6.70	0.00	10	Decay
WH2	25-Oct-09	1	6.70	0.00	10	Decay
WH2	12-Nov-09	18	6.70	0.00	9.7	Decay
WH2	14-Nov-09	2	6.70	0.00	9.7	Decay
WH2	24-Nov-09	10	6.70	0.00	9.7	Decay
WH2	25-Dec-09	31	6.70	0.00	9.7	Decay
WH2	26-Dec-09	1	6.70	0.00	9.7	Decay
WH2	21-Jan-10	26	6.66	0.62	9.7	Fracture
WH2	22-Jan-10	1	6.66	0.00	9.7	Decay
WH2	23-Jan-10	1	6.66	0.00	9.7	Decay
WH2	19-Mar-10	55	6.66	0.00	9.7	Decay
WH2	30-Apr-10	42	7.30	-0.02	9.7	Addition
WH2	26-May-10	26	7.11	0.01	9.7	Decay
WH2	29-Jun-10	34	7.30	-0.01	9.7	Addition
WH2	20-Jul-10	21	7.02	0.02	9.7	Decay
WH2	11-Sept-10	53	7.64	-0.01	5.0	Addition
WH2	27-Oct-10	46	7.46	0.00	9.7	Decay
WH2	16-Jan-11	81	7.08	0.00	10	Decay
WH2	26-Mar-11	69	7.22	0.00	10	Addition

Ice island	Date	Days between images	Surface area (km^2)	Areal rate decrease (km^2 d^{-1})	Sea ice concentration (tenths)	Deterioration Mode
M1	07-May-09		16.30		9.7	
M1	16-Oct-09	162	16.30	0.00	9.7	Decay
M1	18-Oct-09	2	16.30	0.00	9.7	Decay
M1	06-Nov-09	19	16.30	0.00	9.7	Decay
M1	08-Nov-09	2	16.30	0.00	9.7	Decay
M1	09-Nov-09	1	16.30	0.00	9.7	Decay
M1	16-Jan-10	68	15.50	0.01	9.7	Decay
M1	18-Jan-10	2	15.50	0.00	9.7	Decay
M1	18-Feb-10	31	15.50	0.00	9.7	Decay
M1	19-Feb-10	1	12.15	3.35	9.7	Fracture

Ice island	Date	Days between images	Surface area (km^2)	Areal rate decrease (km^2 d^{-1})	Sea ice concentration (tenths)	Deterioration Mode
M2	07-May-09		2.13		9.7	
M2	31-May-09	24	1.95	0.01	9.7	Decay
M2	27-Aug-09	88	1.86	0.00	9.7	Decay
M2	18-Sept-09	22	1.77	0.00	9.7	Decay
M2	16-Oct-09	28	1.77	0.00	9.7	Decay
M2	18-Oct-09	2	1.77	0.00	9.7	Decay
M2	06-Nov-09	19	1.77	0.00	9.7	Decay
M2	08-Nov-09	2	1.77	0.00	9.7	Decay
M2	09-Nov-09	1	1.77	0.00	9.7	Decay
M2	29-Nov-09	20	1.77	0.00	9.7	Decay
M2	30-Nov-09	1	1.77	0.00	9.7	Decay
M2	16-Jan-10	47	1.77	0.00	9.7	Decay
M2	18-Jan-10	2	1.77	0.00	9.7	Decay
M2	18-Feb-10	31	1.77	0.00	9.7	Decay
M2	19-Feb-10	1	1.77	0.00	9.7	Decay
M2	02-Mar-10	11	1.39	0.03	9.7	Decay

Ice island	Date	Days between images	Surface area (km^2)	Areal rate decrease (km^2 d^{-1})	Sea ice concentration (tenths)	Deterioration Mode
M3	22-Oct-09		4.55	0.00	10	
M3	24-Oct-09	2	4.54	0.00	10	Decay
M3	25-Oct-09	1	4.50	0.04	10	Decay
M3	12-Nov-09	18	4.40	0.01	9.7	Decay
M3	14-Nov-09	2	4.40	0.00	9.7	Decay
M3	24-Nov-09	10	4.57	-0.02	9.7	Addition
M3	07-May-10	164	4.46	0.00	9.7	Decay
M3	08-May-10	1	4.45	0.01	9.7	Decay
M3	01-Jun-10	24	4.51	0.00	9.7	Addition
M3	11-Sep-10	102	4.31	0.00	9	Decay
M3	01-Mar-11	171	3.90	0.00	10	Decay
M3	12-May-11	72	3.90	0.00	10	Decay